WEIGHT-OPTIMIZED DESIGN OF A CARBON FIBER AXIAL FLUX ROTOR FOR AVIATION-GRADE ELECTRIC MOTORS

A Thesis

by

CHASE BRANTLEY WILEY

Submitted to the Graduate and Professional School of
Texas A&M University
in partial fulfillment of the requirements for the degree of

MASTER OF SCIENCE

Chair of Committee,	Moble Benedict
Committee Members,	Darren Hartl
	Terry Creasy
Head of Department,	Ivett Leyva

December 2022

Major Subject: Aerospace Engineering

ABSTRACT

This thesis presents a complete structural design process of a rotor for a 250-kW dual rotor axial flux motor suited for single-aisle 150-200 passenger aircraft like the Boeing 737. The initial design space with geometric and material considerations is explored, accompanied by detailed sensitivity studies and comparisons with several different structural configurations in search of a mass optimal structure. The optimal rotor structure found utilized IM7/8552 carbon fiber composites for stiffness in 4 particular sections: the retaining ring, the magnet mounting disk, the spokes, and the root structures. For a nominal axial force of 5750 N at a 1.25 mm air gap distance, the optimal rotor structure which permits only 0.3 mm of deflection weighs only 406 g. Additionally, mass trade-off comparisons are presented using different Aerospace grade materials such as Aluminum 2024-T3 and Titanium 6Al-4V. It was found that the optimal masses of these structures are 831 g and 819 g respectively. A hybrid structure is also analyzed, with an aluminum primary structure and a carbon fiber retaining ring. This yielded an optimal mass of 600 g. Depending on a project manager's goals, this study presents options for a trade study as far as mass-cost trade-offs in the development of a real axial flux motor meant for aircraft.

DEDICATION

To my wife and two cats. They're great!

ACKNOWLEDGMENTS

I would like to thank my advisor and mentor Dr. Benedict for so many years of rewarding work. I approached him in my Junior year of undergrad because he seemed like a very down-to-Earth and helpful professor in class. I was seeking opportunities to be able to practice the engineering skills taught in class, and he immediately welcomed me and gave me a research project to work on. Four years later I now have a broad range of experience with the mechanical and structural design of projects involving water, air, space, and now electric drives. Many challenges arose but he was able to successfully push me through each of them and help me be the best engineering student and researcher I can be. It has been a pleasure, and I seek to continue to apply and refine the skills I have gained during my time here for the rest of my career.

I would like to thank my colleagues at the Advanced Vertical Flight Lab for many years of support with my projects. From the time when I started as an undergrad, all the way up to the time I finish my masters, y'all were there to guide, assist, and help me see the most efficient ways to do things. You are all great and I wish the best future for each of you and to perhaps see you around in the Industry.

I would also like to thank the Aerospace Engineering department, especially the business office, for their unwavering support. They have never denied orders for parts used in our tests, no matter how ridiculous the request. I would also like to thank Ms. Rowe for being a great staff advisor and guiding me through the requirements of the program. I also want to thank Rodney Inmon for his constant support of everything experimental done at our lab. From providing us with lab spaces to allowing us to use his equipment, we wouldn't be where we were without him.

I also wish to thank the professors of Texas A&M for providing quality education to me. They have done an exceptional job of instilling the fundamental physical knowledge and engineering sense needed to succeed. In particular, I wish to thank Dr. Hartl of the Aerospace Engineering department, Dr. Creasy of the Materials Science and Engineering department, and Dr. San Andres of the Mechanical Engineering department. Each of you contributed greatly to my fundamental

skills in structural design, composite design, and vibration analysis. I am happy to have been a student of yours.

I would also like to thank my former professors at Tarrant County Community College: Dr. Magtoto and Mr. Griffin. The guidance given to me in my early academic life was invaluable and helped prepare me for the challenges I faced ahead at Texas A&M and in Graduate School.

Finally, I would like to thank my wife for sticking it out with me throughout my Master's degree. From enduring the Texas Winter Freeze of '21 to allowing me your desk space for all my crazy projects, your support was essential for me to see it until the end. I hope to let this degree enrich our lives and pay us back in multitudes in the future.

CONTRIBUTORS AND FUNDING SOURCES

Contributors

This work was supported by a thesis committee consisting of Professor Moble Benedict (advisor), Professor Darren Hartl of the Department of Aerospace Engineering and Professor Terry Creasy of the Department of Materials Science and Engineering. Dr. Hartl's AERO 405 course introduced me to many of the foundational skills utilized in this thesis, such as structural analysis with Abaqus, optimization techniques, and the application of both in a Python script. Dr. Creasy's MSEN 617 course gave me the fundamental knowledge required in composite structural design. Both courses were a cornerstone in this research and I am honored to have both professors on my committee.

Professor Matthew C. Gardner of the University of Texas at Dallas (UTD) and doctoral researchers Sri Vignesh Sankarraman of UTD and Dorsa Talebi of Texas A&M (TAMU) gave valuable information regarding the electromagnetic side of the axial flux motor in this study. They provided great insight and direction throughout the course of the project, especially with the electromagnetic configuration, electromagnetic forces, rotational speeds, and other important non-structural design considerations.

All other work conducted for the thesis was completed by the student independently.

Funding Sources

Graduate study was supported under a Phase 1 contract from the Advanced Research Project Agency - Energy (ARPA-E) program Aviation-class Synergistically Cooled Electric-motors with iNtegrated Drives (ASCEND). Dr. Peter DeBock serves as the Program Manager.

TABLE OF CONTENTS

Page

LIST OF FIGURES

FIGURE Page

LIST OF TABLES

1. INTRODUCTION*

To slow or halt the progression of climate change, there is a global interest to reduce carbon emissions from industries worldwide. A modern example involves the electrification of automobiles, citing the rise of companies such as Tesla, Lucid, and many other electric vehicle manufacturers. Similarly, many well-established automotive companies are seeking to hybridize their vehicles or outright electrify them, such as Ford's F-150 lightning given in Fig. 1.1.

Figure 1.1: Ford F-150 Lightning [1]

Likewise, there is growing interest in electrifying aviation. The Advanced Research Project Agency-Energy (ARPA-E) has created the Aviation-class Synergistically Cooled Electric-motors with iNtegrated Drives (ASCEND) program in an effort to push the state of the art in this direction. ARPA-E has defined these critical program benchmarks that need to be achieved to enable electrified aviation:

1. Power density at or greater than 12 kW of power per kg of mass

2. Overall motor efficiency at or greater than 93

*Part of this chapter is reprinted with permission from "Design of a Carbon Fiber Rotor in a Dual Rotor Axial Flux Motor for Electric Aircraft" by Chase Wiley, 2022. 2022 IEEE Energy Conversion Congress and Exposition (ECCE), Copyright 2022 by The Institute of Electrical and Electronics Engineers, Incorporated.

The current state-of-the-art motors significantly fall short of these metrics. For example, the YASA 750 R, which is considered a high-performing Axial Flux motor currently available on the market, has 200 kW of peak power with an advertised power density exceeding 5 kW/kg [2]. However, to have motors powerful enough for single-aisle commercial aircraft like the Boeing 737, these motors need to push the bounds of power density by over twofold.

Texas A&M and the University of Texas at Dallas have engaged in Phase 1 of the ASCEND contract, and have sought out high power density electromagnetic, structural, and thermal configurations through the use of many simulations and trade-off studies. Together, we have achieved a motor design that exceeds a power density of 13 kW/kg, and efficiencies above 93%. This thesis focuses on the development of a lightweight rotor structure including material selections, three different configurations, and a comprehensive optimization study.

1.1 Motor Electromagnetic Configuration

There are two overarching configurations of electric motors: radial flux and axial flux. Radial flux configuration typically consists of the stator wrapping around the magnetic rotor array in the radial direction. These are typically long cylindrical motors and are most common in the industry. On the other hand, axial flux motors position either two sets of magnetic rotors on both sides of one stator or one set of magnets between two stators. These are axially short and large in diameter, much like a pancake shape. Fig. 1.2 introduces a diagram highlighting these key differences.

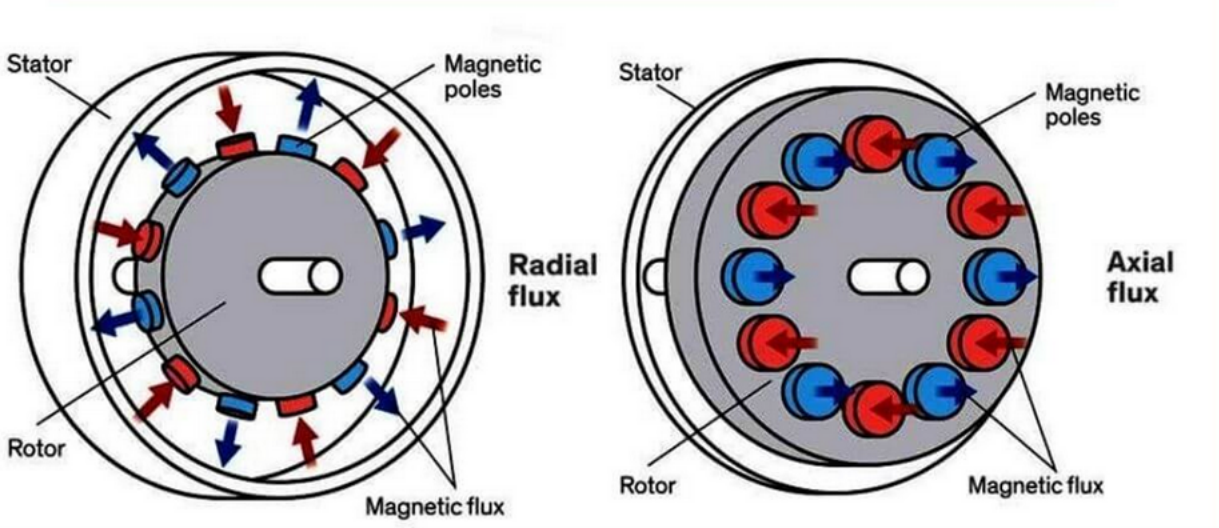

Figure 1.2: Comparison between a radial flux and axial flux motor [3]

The motor that Texas A&M University and the University of Texas at Dallas have designed follows a dual-rotor axial flux configuration. Figure 1.3 outlines the rotor magnets and stator used in the electromagnetically active portion of the design. In this design, grain-oriented electrical steel (GOES) is used for higher design power density [4] and efficiency [5]. The rotor houses permanent magnets which are segmented in a Halbach array.

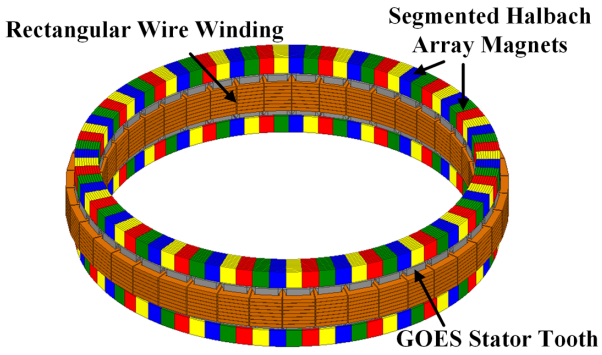

Figure 1.3: Electromagnetically active portion of the proposed motor [4]

The electromagnetic design of the active motor components (magnets, windings, stator tooth, etc.) given here has been thoroughly optimized and designed by our collaborators in [4]. This provided an excellent starting point for us to perform the structural design of the 250 kW motor. This paper provides the initial design sweep for electromagnetic performance, factoring in inter-

faces with other motor systems such as the structure, inverter, and thermal systems. 1.4 shows a few points of the design sweep and tabulates the electromagnetic mass, rotor axial force, and efficiency during take-off. The red arrow identifies the initial design configuration much of this thesis is based on. Some key parameters are given in Table 1.1, and the mass, efficiency, and rotor axial force are taken to be 7.4 kg, 95.6%, and 5.75 kN respectively.

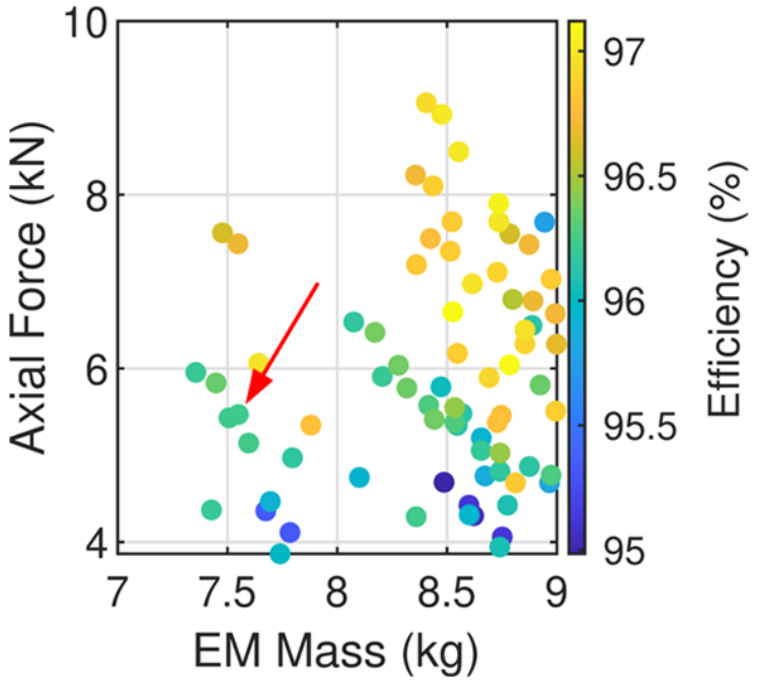

Figure 1.4: Axial rotor force, electromagnetically active mass, and takeoff electromagnetic efficiency of the best points in the electromagnetic design sweep [4]

Table 1.1: Motor's key electromagnetic parameters.

Parameter	Values
Peak takeoff power (kW)	250
Cruise power (kW)	83
Takeoff speed (RPM)	5000
Cruise speed (RPM)	4000
Pole pairs	20
Number of stator teeth	42
Rotor magnet outer diameter (mm)	270
Rotor magnet inner diameter (mm)	220
Magnet thickness (mm)	10

1.2 Motor Structural Materials Literature Review

Aluminum, titanium, and carbon fiber composites commonly find use in electric motors. Due to aluminum's low density and high conductivity, aluminum conductors have been chosen as an alternative to copper conductors in electric motor applications [6]. Additionally, carbon fiber and titanium have low conductivity and are popular design choices for retaining sleeves in rotors, owing to their high strengths [7]. However, due to Aluminum's high conductivity, applications as a structural material in electromagnetically active sections of the motor can cause significant eddy current losses, which reduce overall efficiency. Nonetheless, aluminum can be used as a structural material where variations in the magnetic field are small, such as in the rotor [8] or the motor housing [9]. On the other hand, carbon fiber reinforced polymers (CFRPs) have low conductivity and can be used in place of aluminum structures [10]. CFRPs have also been used as support material in magnetic gears [11]. Titanium has more conductivity than CFRP and will be penalized by increased eddy current losses. Regardless, some applications still use titanium alloy as a support material for electric motors [10], [12].

In aerospace applications, it is often the goal to create functional structures with minimal mass.

Figures 1.5 & 1.6 present an Ashby chart, comparing many material classes with their properties against each other. Figure 1.5 specifically compares the young's modulus and the density, while Fig. 1.6 compares the strength of materials against their density. Aerospace structures tend to favor materials that are stiff, strong, and lightweight. A great way to determine which material class outperforms the other is to refer to the simplified Ashby chart given in Fig. 1.7. Note the line for constant Young's modulus over density (E/ρ) on the chart. The material classes below that line perform worse than the ones above (less stiffness or strength for the same unit of density). Following this logic, it is easy to see that the materials near the upper left-hand corner of the chart have the best mass-specific performance, due to having a higher modulus per unit density. This is a reason why high-performing Aerospace structures tend to be composed of composites, ceramics, and metals as opposed to elastomers and polymers. Also note that in both charts using Young's modulus or Strength, CFRP provides a peak much higher than the metallic materials. This highlights the fact that carbon fiber composites provide state-of-the-art structural performance.

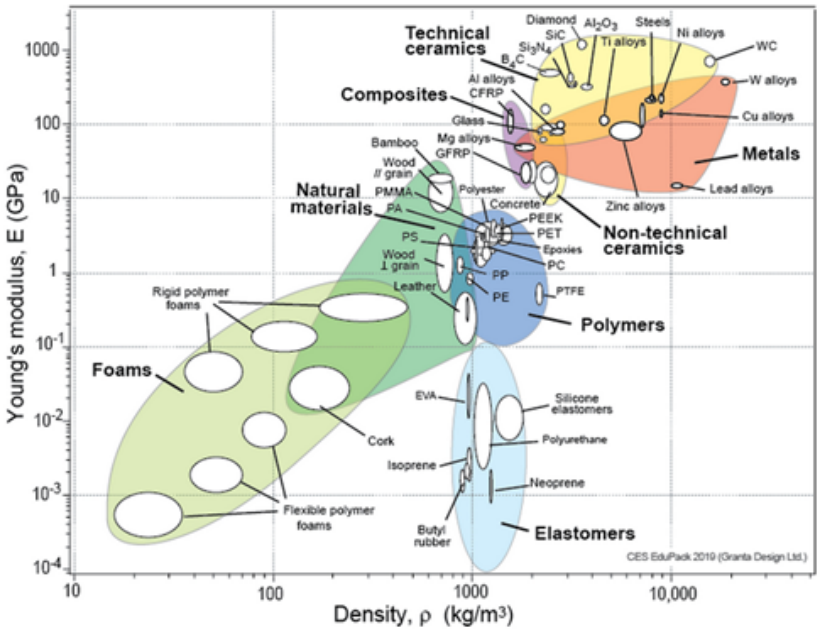

Figure 1.5: Ashby chart of Young's modulus vs density [13]

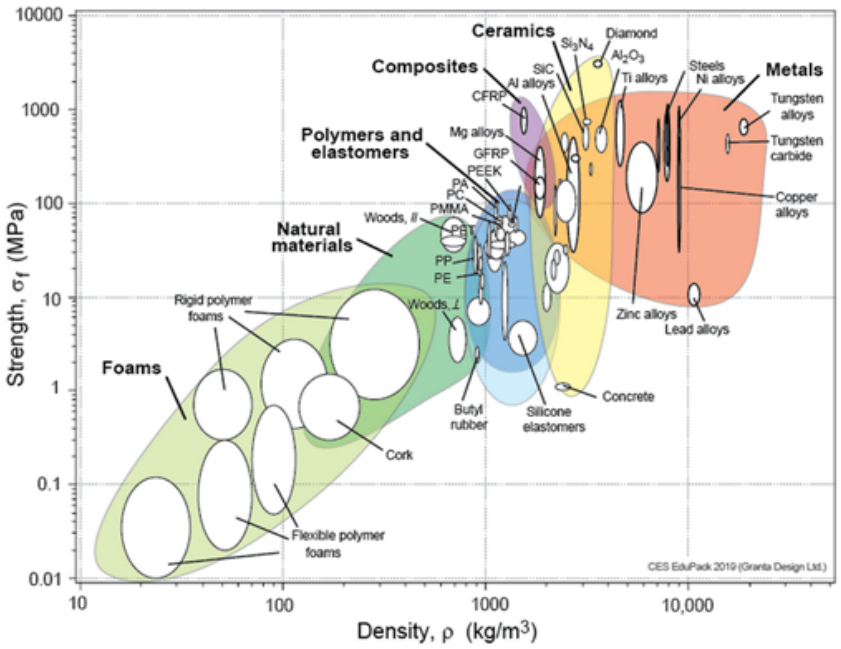

Figure 1.6: Ashby chart of strength vs density [13]

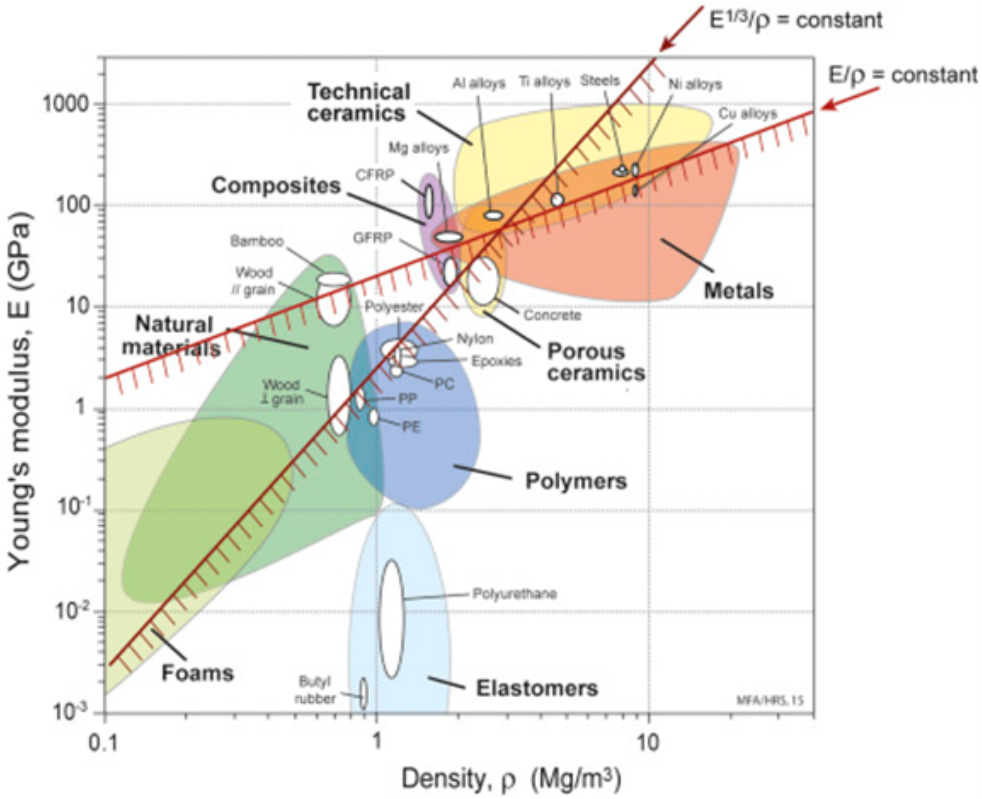

Figure 1.7: Ashby chart of Young's modulus vs density with guidelines for minimum mass designs [14]

a

Two metallic materials common in the aerospace industry will be considered, aluminum and titanium. Because there are dozens of aluminum and titanium alloys to choose from, a discussion involving these materials will be restricted to two alloys that find extensive use in the aerospace industry: aluminum 2024-T3 and Ti-4V-6Al. While these alloys generally do well to represent the performance capabilities of these material classes, there are likely other alloys that may better suit specific applications. For decades, CFRPs have replaced many formerly metallic structures in aircraft [15]. An Intermediate Modulus fiber/resin system is chosen to represent the class of carbon fiber composites (IM7/8552). These three material choices form the basis of this research and have their density, stiffness, strengths, and specific stiffness and strength values tabulated in Table 1.2. Note that the failure strength values given are based on yield strength for the metallic materials and the ultimate strength for the composite.

Table 1.2: Mechanical properties of aluminum, titanium, and IM7/8552 composite [16][17][18]

Material	Density (g/cm^3)	Young's Modulus (GPa)	Failure Strength (MPa)	Specific Stiffness ($GPa/(g/cm^3)$)	Specific Strength ($MPa/(g/cm^3)$)
Aluminum 2024-T3	2.71	68.3	234	25.2	86.3
Titanium Ti-6Al-4V	4.43	110	869	24.8	196
IM7/8552 (Longitudinal Properties)	2.71	171	2326	110	1500

1.3 Design with Composites Literature Review

Composites are fundamentally different from conventional materials. In metallic alloys such as Aluminum, the constituent elements are typically blended together homogeneously. This results in an isotropic material, meaning that structural properties such as the Young's Modulus and Yield

Strengths are consistent regardless of orientation. However, in the case of composite materials, there are two or more constituent materials that combine to form one structure. Some typical examples of composite materials include reinforced concrete, plywood, sandwich panels, and carbon fiber-reinforced polymers. This literature review will focus on Carbon Fiber Composites. These composites typically consist of thousands of fibers made of carbon that impregnate a polymer matrix.

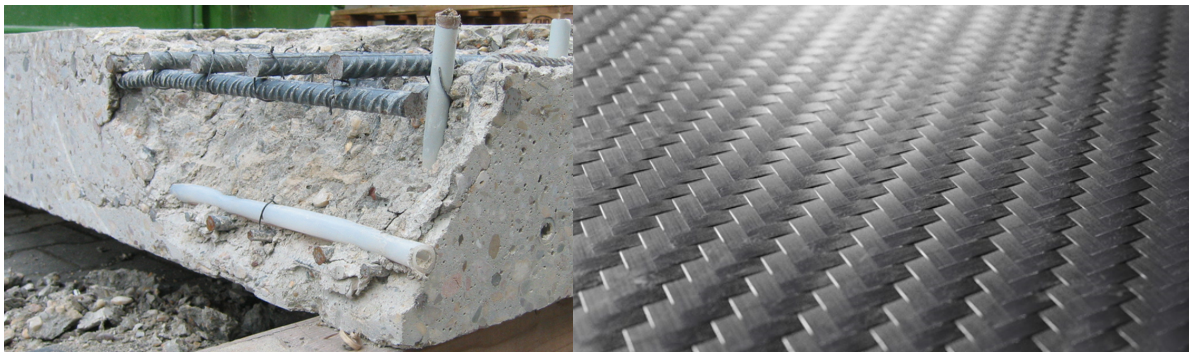

(a) Reinforced concrete [19] (b) Woven carbon fiber laminate [20]

Figure 1.8: Examples of composite materials

The properties of the carbon fiber and the matrix (or resin) tend to vary considerably. An example of this is given in Table 1.3 comparing the stiffness of IM6 carbon fibers in a PEEK resin. Figure 1.9 gives a visual representation of the fibers (black lines) in the matrix (blue), along with defined orientations 1 and 2. Note that along the fibers (direction 1), the Young's modulus is 161 GPa, while perpendicular to the fibers (direction 2) the modulus is 8.2 GPa. The fiber direction is nearly 20 times stiffer!

Table 1.3: IM6/PEEK composite mechanical properties [17]

Direction	Young's Modulus (GPa)
E_1	161
E_2	8.2

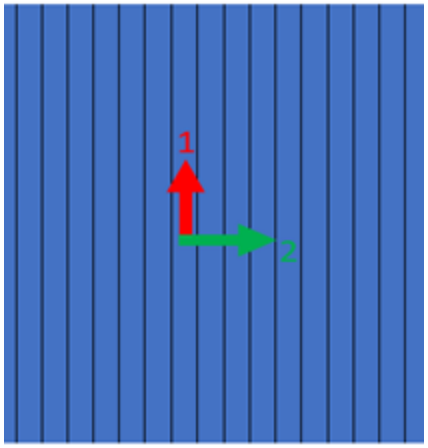

Figure 1.9: Composite plate with material axes shown. 1 runs parallel to the fibers, 2 runs transverse to the fibers [18]

There are many different types of carbon fiber composites as shown in Figure 1.10. There is continuous fiber (most popular), discontinuous fiber, particle reinforced, and sandwich panels. Continuous fibers tend to offer the best performance of carbon fiber composite laminae. This is because there are no breaks along the carbon fibers, the lamina benefits fully from the stiffness and strengths that the carbon fibers offer. The largest complication that occurs from this, however, is that the lamina is then very anisotropic in its properties. However, this is not necessarily a downside and can be leveraged to give extremely high-performing structures. In contrast, discontinuous fibers have short or "chopped" fibers in their laminae. One benefit of this process is that short fibers typically already exist in the matrix beforehand, so the technician can have an easier time physically assembling the laminate. However, these types of composites do suffer from reduced structural performance, while not necessarily being less dense; therefore, they are not as popular. Furthering the benefits of the previous category are the particle-reinforced composites. In this case, the creation of the part can be as easy as spraying the matrix with particle reinforcements inside. Additionally, these parts are typically isotropic or have properties that are uniform in all directions. However, it typically has the worst structural performance out of all other carbon fiber composite classes. Finally, sandwich panels are another popular choice of composite to use in the industry. As shown in Fig. 1.11, the sandwich panels are typically composed of several layers including a honeycomb core, two facings, and an adhesive to join these together. Sandwich panels provide

extreme stiffness for very low mass, often even outperforming solid continuous carbon fiber panels. The honeycomb core can be made from many different materials, such as Aluminum, Titanium, or the honeycomb can be replaced completely with foam instead. It is common for carbon fiber laminae to be used as part of the facings of these panels. However, some drawbacks include greater complications in manufacturing and the introduction of more possible failure modes. The focus for the rest of the thesis will be placed on continuous fiber composites.

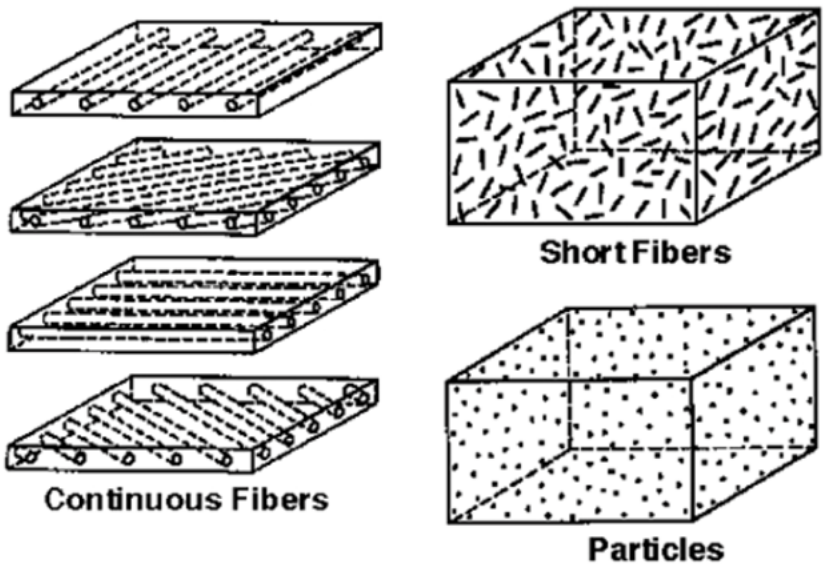

Figure 1.10: Types of carbon reinforced polymers [21]

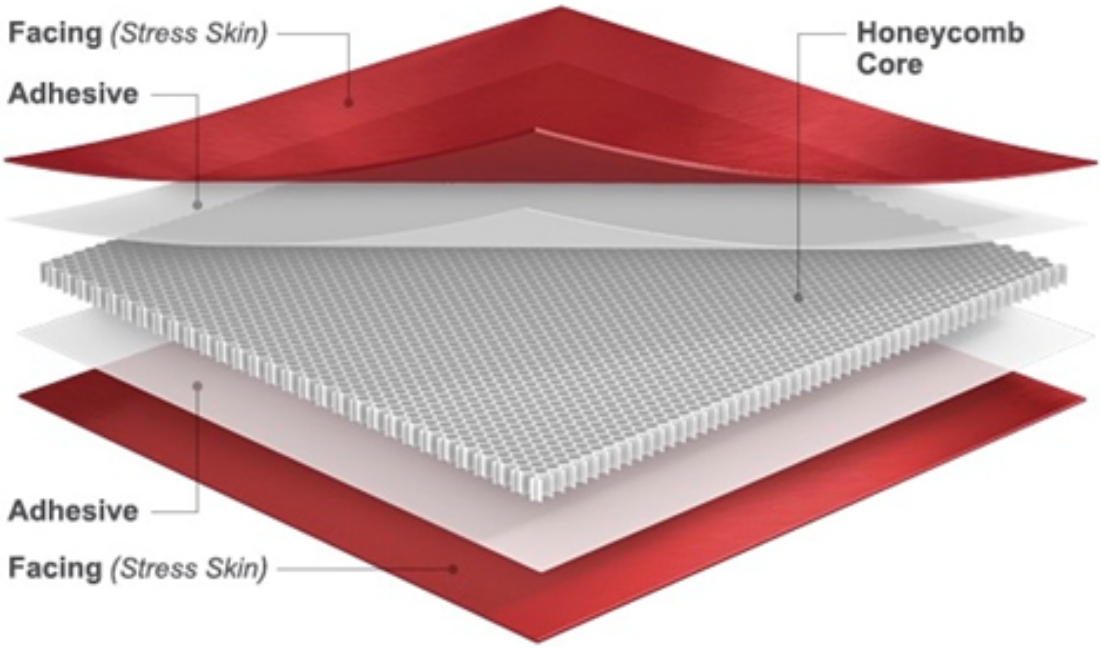

Figure 1.11: Parts of a sandwich panel [22]

There are many different selections of carbon fibers that exist, as well as selections for the matrix that they impregnate. There are virtually endless combinations of fibers and matrices that can make up a composite. The typical nomenclature for identifying the material consists of fiber/matrix. For example, IM7 fibers that are placed inside of a PEEK matrix would be IM7/PEEK. Carbon fiber composite structures are also typically formed via stacking a series of laminae (single plies). This structure is called a laminate. The laminate is identified using a laminate stacking sequence, which specifies the orientation of each lamina and the sequence in which they are to be stacked. These are typical of the form [first ply, next ply, ..., last ply]. For example, a simple laminate consisting of a 0-degree and a 90-degree ply (perpendicular set of laminae) is [0,90]. There are multiple different types of layups, such as quasi-isotropic, asymmetric, symmetric, and balanced, among others. For the current research, quasi-isotropic and symmetric layups are the most important. A quasi-isotropic layup results in a laminate that has the same planar mechanical properties regardless of orientation. For example, a [0,45,-45,90,90,-45,45,0] layup is quasi-isotropic and will have the same modulus of elasticity over the 0-degree to 90-degree range of orientations. Additionally, because this particular layup "mirrors" itself

about the midplane, this is also a symmetric layup. It is convenient to specify a symmetric layup with an "s" subscript, so the layup in question can also be called out as $[0,45,-45,90]_s$. Another useful tool in simplifying the callout of the stacking sequence is to indicate the number of times the sequence repeats with a sub-scripted number. For example, [0,90,0,90] can be simplified with $[0,90]_2$. The selection of laminate stacking sequence is of critical importance in the design of composite structures, and knowledge of this nomenclature will benefit the reader throughout the thesis.

In the case of metallic materials, several different failure modes exist. Some examples include yielding, brittle fracture, fatigue, and buckling. Composite materials can also experience these types of failures, but they can also fail in many more ways. Some examples include but are not limited to fiber tensile failure, fiber micro-buckling, fiber-matrix debonding, matrix cracking, and delamination. An example of each is presented in Fig. 1.12. Additionally, these failure modes are known to interact with each other. For example, matrix cracking can spread to the fibers and cause fiber-matrix debonding. This can then lead to fiber micro-bucking, delaminations, etc.

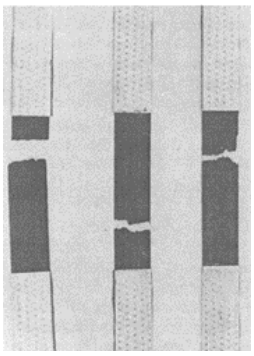

(a) Fiber tensile failure [23]

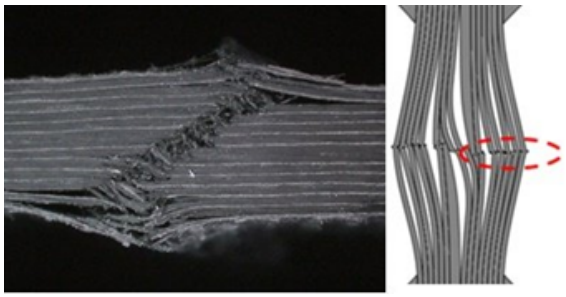

(b) Fiber micro-buckling [24]

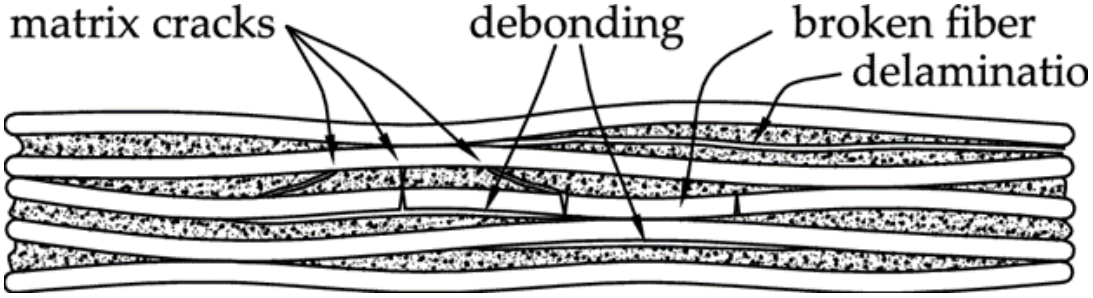

(c) Cross section of failing laminate [25]

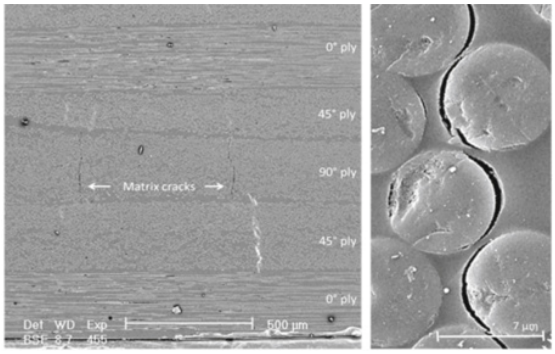

(d) Matrix cracking [26]

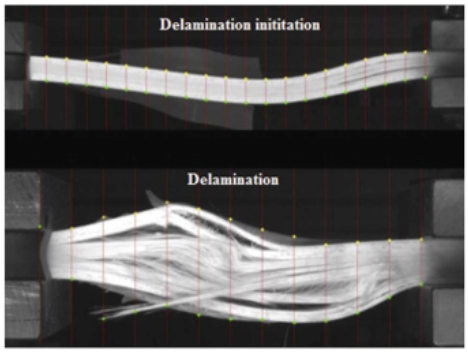

(e) Progression of delamination [27]

Figure 1.12: Examples of carbon fiber composite failures

Because of the large number of failure modes and their complex interactions, composite structure designers are faced with a great challenge in designing structures that are safe, especially ones which undergo many cycles. With metallic structures, it is common to assign a safety factor that reduces the maximum allowable stress that the structure experiences. For metalic structutes the common approach is to use the Von-Mises stress. A similar approach can be used in the safe design of composites, but with more nuance. First, it is important to recognize that a Von-Mises stress calculation in a composite structure does not give useful information. Instead, one should only look at the normal and shear local stresses in each lamina, as opposed to the global stresses in

the laminate. These stresses are indicated by normal stresses σ_1, σ_2, σ_3 and shear stresses τ_4, τ_5, τ_6. In the design of a structure which will not fail under these stresses, multiple options exist for determining a safe design: Max Stress, Tsai-Hill, Tsai-Wu, and others as shown in Fig. 1.13. In this figure the Normal Stress σ_2 is plotted against Shear Stress τ_6. This plot also contains multiple lines or curves based on some composite failure design criterion. Additionally, the plot contains data points of composite test specimen failures and their corresponding stresses at failure. The idea is based on the fact that according to this criterion, a safe structural design exists when maximum stresses are inside of these boxes. For example, in the case of the max stress criterion, a design is predicted to be safe when the maximum normal stress σ_2 is less than the maximum recorded normal strength F_2. Likewise, when maximum shear stress τ_6 is less than the recorded strength F_6, the design is considered safe. Therefore, according to the max stress criterion, any design with stresses that lie within that box space is considered safe. However, note that Fig. 1.13 shows some data points of failure that lie within these boxes! This is because the maximum stress failure criterion, while simple, does not take into account the complex stress interactions that occur when multiple stress components exist. This is a reason why other failure criteria such as Tsai-Hill exist.

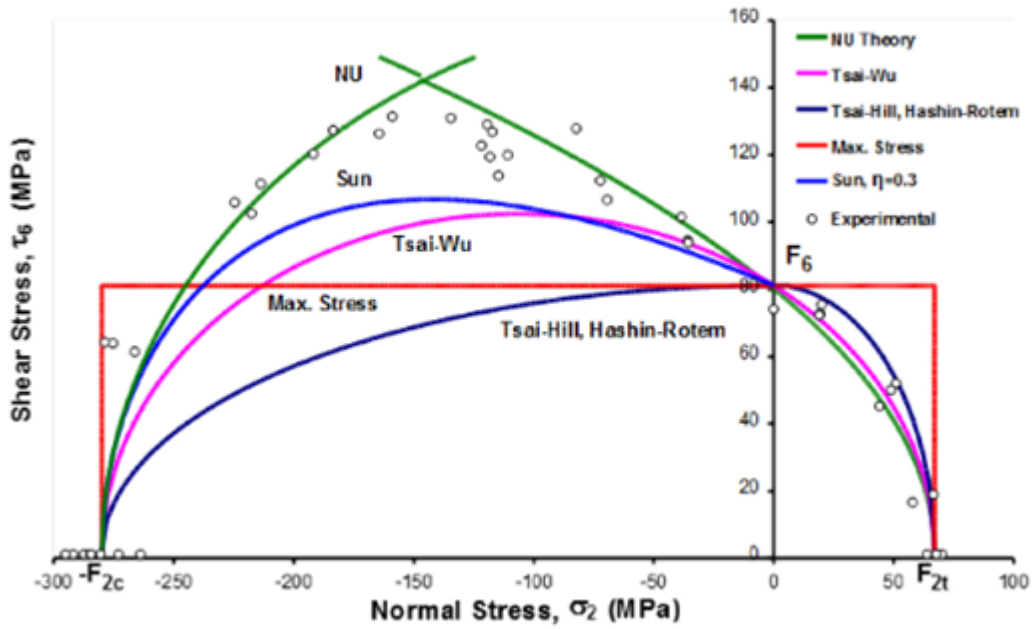

Figure 1.13: 2D stress plot of a carbon fiber composite with failure points and predicted failure Theories [28]

Finally, the composite structure designer also needs to be aware of the other limitations of using carbon fiber composites. One of the more important limitations involves the glass transition temperature of the matrix. Typically, at room temperature, the thermoset or thermoplastic resin is hard and stiff. This stiffness slightly but monotonously degrades as temperature increases. However, there is a temperature where the stiffness undergoes a very rapid decrease. This temperature is called the glass transition temperature, typically denoted as T_g, and is plotted in Fig. 1.14. This indicates a transition from a hard glassy state to a rubbery state for the resin. Glass transition temperatures vary depending on the resin, typically from 80 C to 160 C. Thermoplastic resins tend to have a higher T_g than thermosets. In the specific application of motor design, special attention needs to be paid to the maximum expected temperatures of the magnets as well as other components supported by the carbon fiber composite structure. In our case, the maximum temperatures of the rotor magnets will be around 100-120 C and therefore, some selectivity is needed in choosing a proper matrix for our carbon fiber structure. Another limitations to be aware of are is galvanic corrosion, which occurs when a carbon fiber composite is in contact with a galvanizing surface, such as aluminum. However, since no contact between the rotor structures and an aluminum surface is to be expected, this is outside the scope of the thesis.

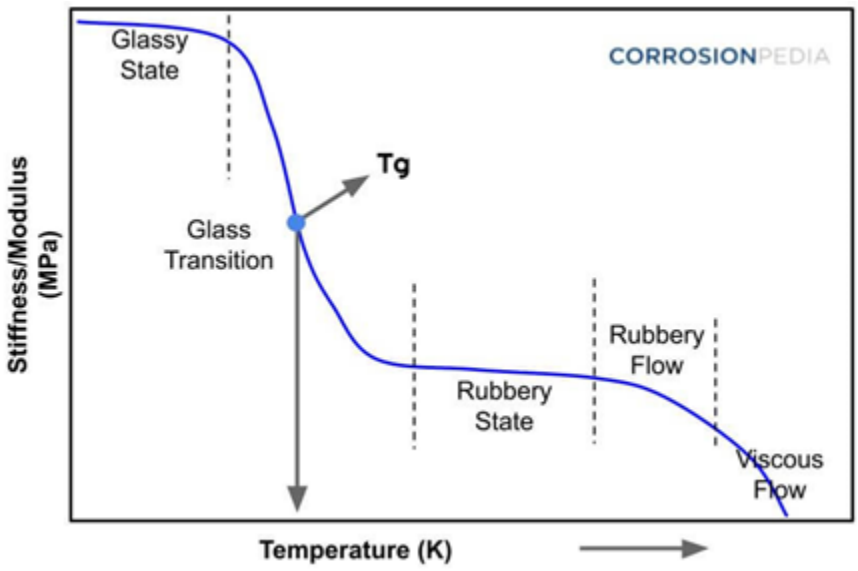

Figure 1.14: Example of a composite matrices glass transition temperature curve [29]

1.4 Research Objectives

Conventional combustion aircraft engines also have moved to more weight-efficient composite materials, like in the case of the Boeing 787 [14]. However, the relatively low maximum operating temperature of composites is a key limitation in combustion engines since the turbine combustion chamber can exceed 1000 °C. However, for the proposed electric motor, the rotor temperatures are not expected to exceed 100 °C. This enables the thorough use of carbon fiber composites in the rotors, facilitating extreme mass reduction, and further highlighting the competitive advantage of electric engines over conventional combustion engines in aerospace applications [18]. In the following chapters, given the initial electromagnetic design introduced, the mechanical design space for the rotor structure is thoroughly explored. Multiple configurations with carbon fiber polymers are optimized and compared against each other until a superior configuration emerges. Sensitivity studies are performed on the laminate stacking sequence and on the material properties generally available with carbon fiber composites. This will help find what design guidelines will tend to be most advantageous. Additionally, a genetic algorithm developed in Python is paired with Abaqus Finite Element Analysis (FEA) and used to find optimized rotor structure designs. From these studies, multiple scatter plots comparing mass and maximum deflection are formed and from that several optimal designs are presented and then compared. For the sake of completeness and fair comparison, these studies are repeated with aluminum, titanium, and a hybrid structure of aluminum and carbon fiber composites. These are then compared to provide the reader with an idea of the benefits of using carbon fiber composites in the rotor structure over conventional materials. Based on the lessons learned from the initial designs, a new set of electromagnetic designs are co-optimized with carbon fiber rotor structures, and a new global optimal configuration is obtained.

2. ROTOR STRUCTURAL DESIGN*

This section of the thesis will introduce the geometric parameters the rotor structure design must satisfy. Additionally, the most prominent load cases will be introduced as well. After this, the design space will be thoroughly defined, and some analysis will be performed to help the designer find guidelines that will point in the right direction for an optimal design. For example, given the wide array of composite choices, a sensitivity study will be conducted to determine which mechanical properties to prioritize over others. Finally, the three main structural configurations of the rotor will be introduced in this chapter and analyzed in the following sections.

2.1 Rotor Design Parameters

The electromagnetic configuration given in Figure 1.3 and detailed in Table 1.1 shows the interface parameters given to the structures team. As far as the rotor structure is concerned, the most important geometric parameters are the magnet size and location. The magnets are assembled into a ring around the outer perimeter of the rotor structure. This ring is composed of 80 different Neodymium magnets, assembled in a Halbach Array. The inner diameter of this is specified at 220 mm, the outer diameter at 270 mm, and the axial length at 10 mm. For the sake of centrifugal load considerations introduced later, this gives a magnet mass of 1443 g per rotor. The centrifugal force produced by the magnets drives the thickness of the retaining ring used to radially constrain the magnets at high rotational speeds. The overall rotor structure must be designed to meet these geometric constraints.

It is also estimated that at the full 250 kW load, the temperature of the magnets will reach up to 100 degrees Celsius. It is then important to pay attention to the Glass Transition Temperature of the carbon fiber based rotor structure. As a rule of thumb for designers, since we are expecting up to 100 C of temperature, the matrix selection should have a glass transition temperature of at least

*Part of this chapter is reprinted with permission from "Design of a Carbon Fiber Rotor in a Dual Rotor Axial Flux Motor for Electric Aircraft" by Chase Wiley, 2022. 2022 IEEE Energy Conversion Congress and Exposition (ECCE), Copyright 2022 by The Institute of Electrical and Electronics Engineers, Incorporated.

120 C. Fortunately, there exists many composite resins that meet this requirement. However, this is still an important limitation on the design and attention should be given to this.

2.2 Load Cases

Over the operating cycle of the motor, many forces act on the rotor structure. In particular, there are two main load cases to consider: the no-load (0 RPM) and the full load (5000 RPM).

In the no-load case, the rotor is completely stationary and only the axial attractive forces between the magnets and the stator iron act on it. No torque is being transmitted, and centrifugal forces are absent. However, the overall estimated axial attraction force per rotor is not trivial, as it is estimated to be 5750 N (1293 lbf). Additionally, for the sake of motor efficiency, the air gap between the magnets and stators should be designed to be as small as possible. In our design, it is specified that a nominal air gap of 1.25 mm exists in this region. This does not offer much space for the rotor structure to deflect at these high loads. In this design, we are targeting a design deflection of no more than 0.3mm at the 5750 N expected load. Thus, structural stiffness is paramount in this design. A free body diagram of this loading is shown in Fig. 2.1 with a 2D representation given in Fig. 2.2.

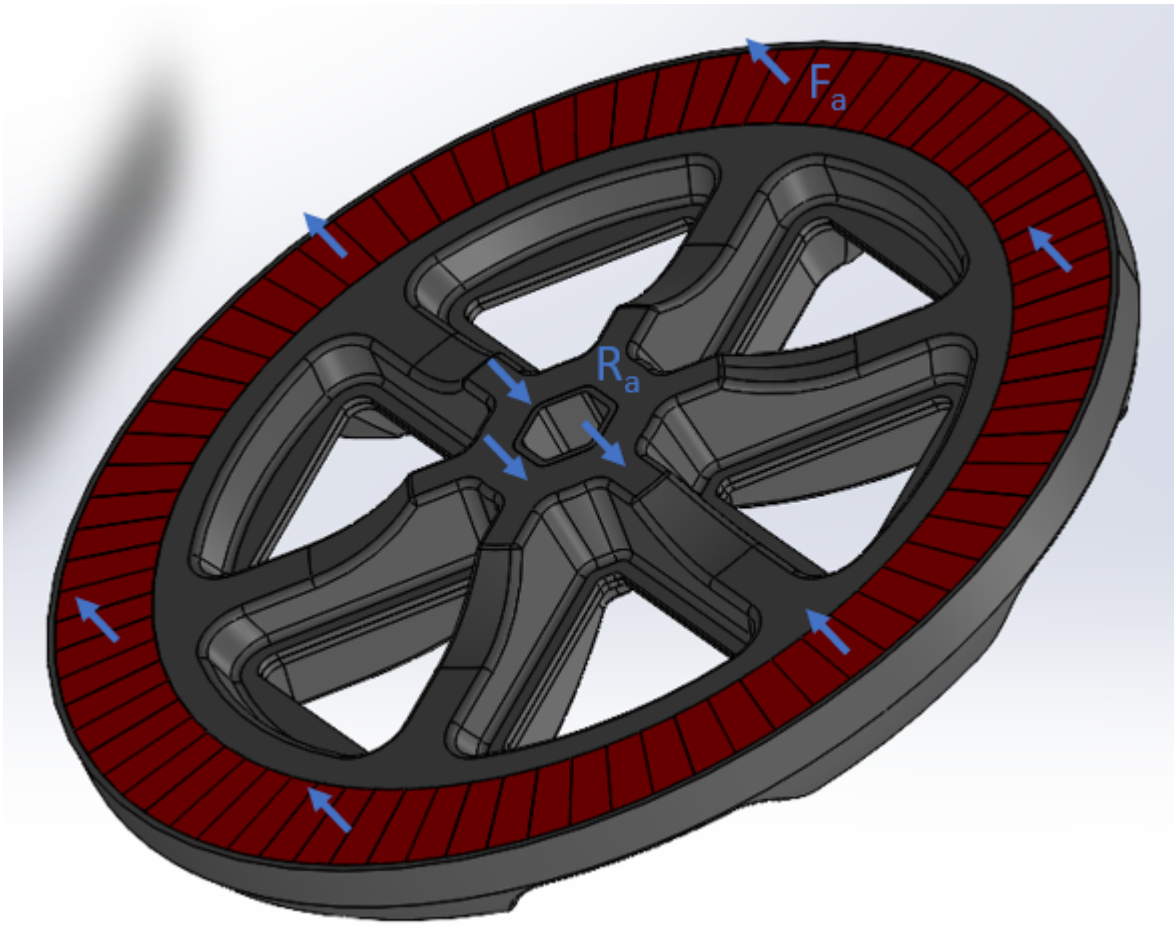

Figure 2.1: No RPM 3D free body diagram

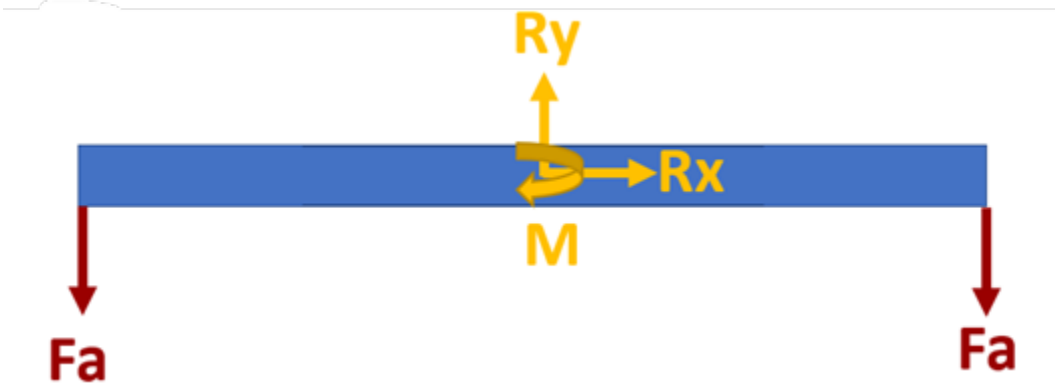

Figure 2.2: No 2D RPM free body diagram

The other load case involves the state in which the motor is spinning at full load – or 5000 RPM. In addition to the axial forces which exist in the no-load state, there is now a tangential force that is

transmitted from the magnets to the structure, and a large centrifugal force from the magnets and overall structure to support. A free-body diagram of these forces is given in Figure 2.3 with a 2D representation in Fig. 2.4. In the no-load case, much concern is given over the axial deflections and the corresponding shrinkage of the air gap. However, in this case, these concerns are somewhat alleviated due to the dynamic stiffness provided by the centrifugal forces. A visual example of this is by considering how the blades of a helicopter rotor will "sag" when not spinning, but will become stiff when operating at its rotational speed. Instead, more concern is placed on whether or not the structure can withstand the large centrifugal forces and the tangential forces which generate the torque of the motor. Table 2.1 gives the estimated total magnitudes of these forces. Note that Figures 2.2 and 2.4 are simply a 2D representation of a 3D load case, and that in reality the forces labeled act more or less evenly around the circumference of the rotor structure. For example, the axial force Fa has an overall magnitude of 5750 N, yet this overall magnitude is evenly distributed around the outer circumference as opposed to being concentrated into two regions as Fig. 2.2 may suggest.

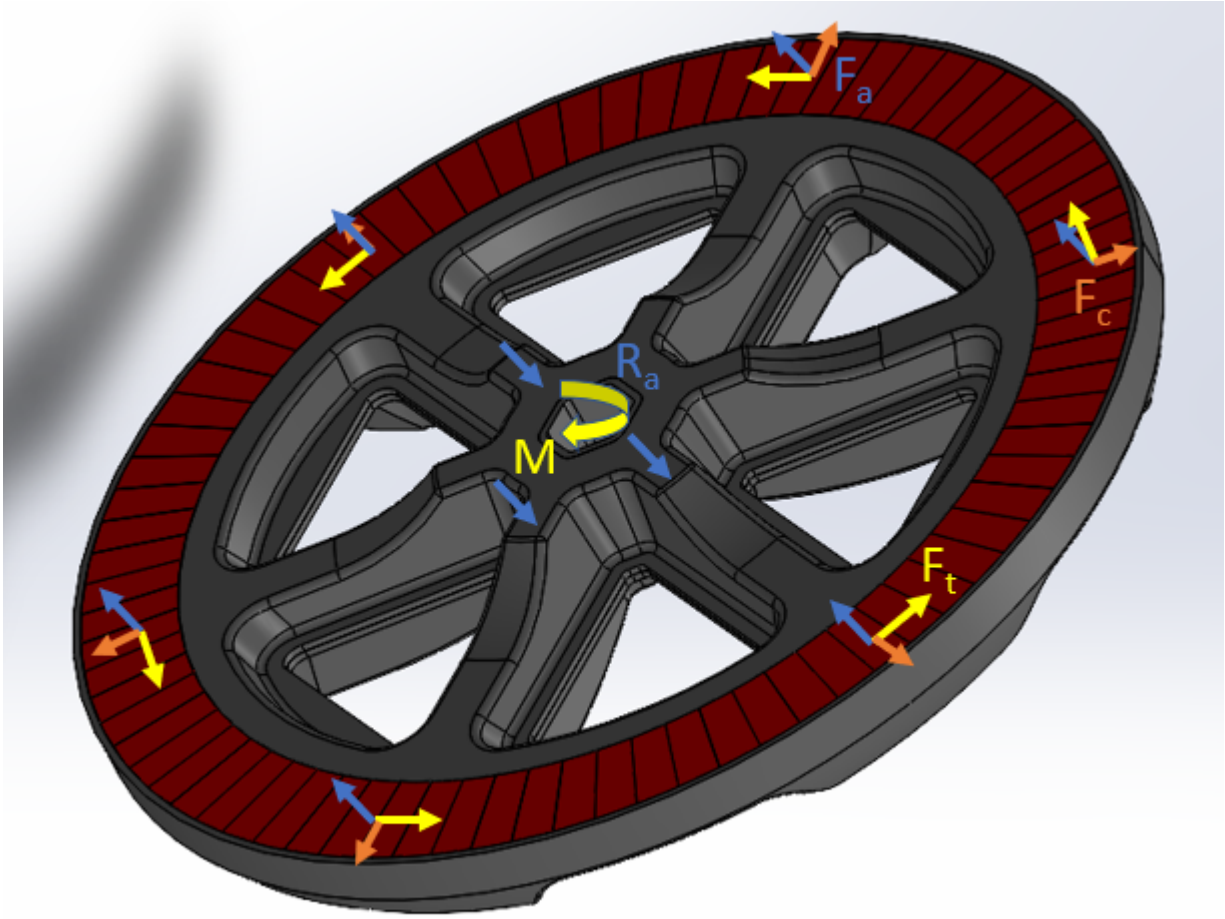

Figure 2.3: Full RPM 3D free body diagram

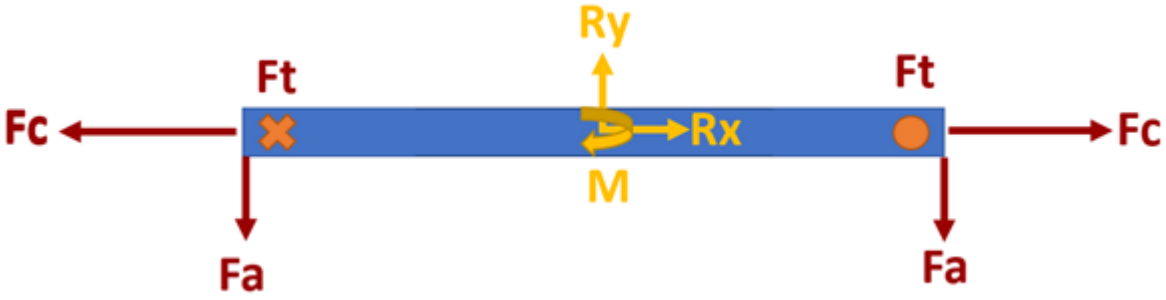

Figure 2.4: Full RPM free body diagram

Table 2.1: Summary of overall forces and magnitudes

Load Type	Distributed Force Magnitude (N/mm)	Total Integrated Force (N)
Axial, F_a	6.78	5750
Tangential, F_t	2.09	1769
Centripetal, F_c	63.97	53413

As will be seen throughout the rest of the thesis, the discussion will be centered around finding an optimal mass structure that is stiff. What about the strength of the structure? For the IM7/8552 composite structure, the longitudinal tensile strength is given as 2326 MPa and the transverse tensile strength as 62.3 MPa. The full RPM load case as given in Table 2.1 will cause the highest stresses in the structure. An example output of an FEA study done on the cutout disk structure (introduced in a later subsection) is given in Fig. 2.5. The highest stress S_{11} found is 247 MPa, and the highest S_{22} found is 11.5 MPa. When comparing with the strengths of the composite materials, safety factors of 9.4 and 5.4 exist respectively. These stress magnitudes are found to be characteristic of designs meeting the axial deflection constraint of 0.3 mm in the no RPM load case. Due to the large values of factors of safety, using the maximum stress failure criterion is acceptable for the structure. Additionally, when later evaluating each design with FEA a script automatically checks for broken stress constraints in each model and will filter structures that violate the stress constraints out of consideration. Thus, it is more interesting then to focus the following studies on stiffness and axial deflections of the structure.

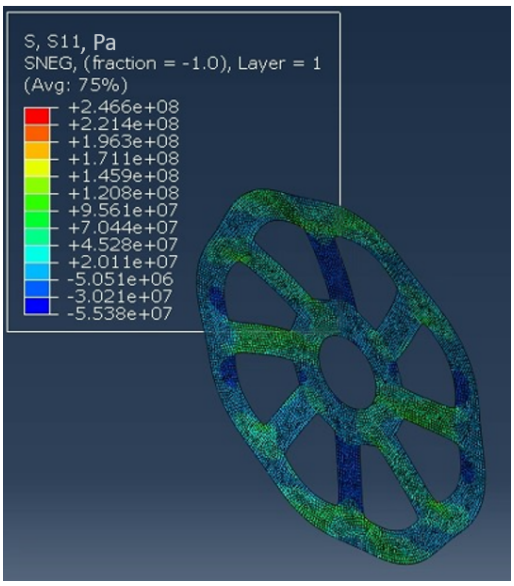

(a) FEA output with largest S_{11}

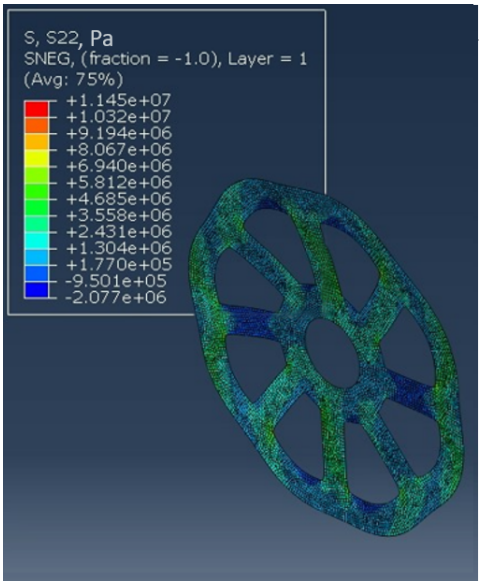

(b) FEA output with largest S_{22}

Figure 2.5: FEA outputs of cutout disk structure under full RPM load case

2.3 Critical Rotor Speed

Since the entire rotor will be undergoing rotational speeds from 0 to 5000 RPM, it is imperative that the rotor assembly be designed such that it's critical speed does not get excited. Fig. 2.6a shows an in context view of the entire rotor assembly including two rotor structures, the shaft, and bearings. To estimate the critical speed of the shaft, the method of using influence coefficients is used as given in chapter 7, section 6 of [30]. Fig. 2.6b will approximate the rotor assembly with all relevant forces and locations given. Selecting 303 Stainless Steel as the shaft material gives a young's modulus of 193 GPa [31]. Other key shaft geometric parameters include an overall length of 116 mm, outer diameter of 20mm, and an inner diameter of 14 mm. Knowing that each rotor has a magnet weight of 1.5 kg, and approximating the structure to weigh 1.0 kg each, then F1 can equal to F2 at 2.5 kg of force, or 24.5 N each. Then, finding the critical speeds according to this method gives the first resonant speed at 10,100 RPM. Since the maximum design speed is 5,000 RPM, resonance is not to be expected.

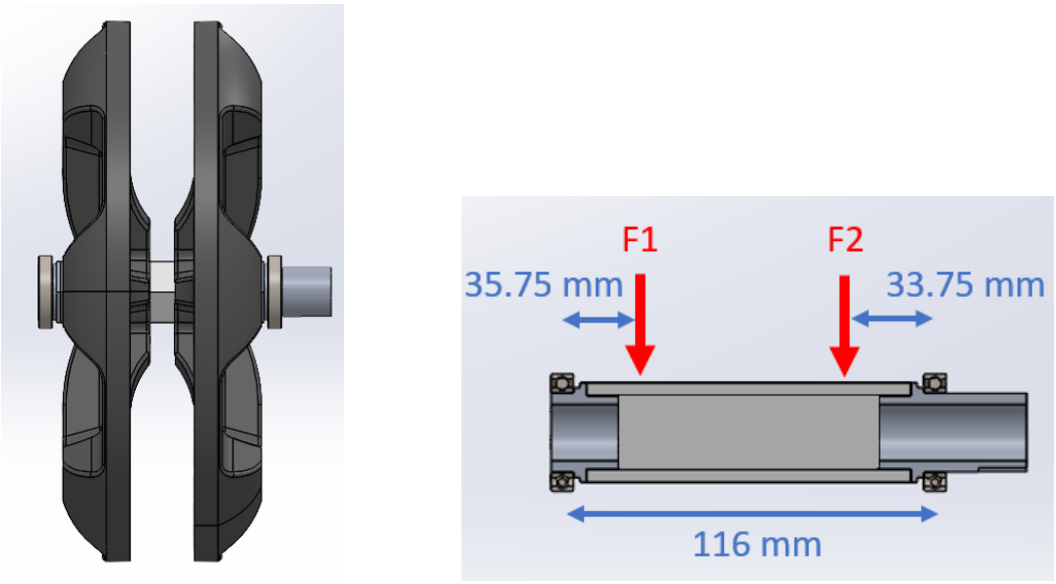

(a) Side view of rotor (b) Simply supported shaft used in analysis

Figure 2.6: Figure of the rotor assembly and supporting shaft

2.4 Design Space

The introduction chapter provided the reader a brief primer on basic composite terminology. As mentioned before, carbon fiber composites are identified with a selection of fiber and matrix in the form of fiber/matrix. Because there are hundreds of different fibers to choose from, and just as many resins, there is a virtually endless selection of carbon fiber composites that exist in the market. A general idea of the mechanical properties over a wide range of composites are provided in Figs. 2.7 and 2.8. These Tables are taken from [17] and give a good overview of composite material properties. Note how each table lists up to 30 different properties for each material! While we may not need many of these properties in the present analysis, there will still be several properties that are relevant to our study, which need to be paid attention to. Section 2.5 provides a "sensitivity" study which will show the mechanical property that is most important in the design of a composite structure that is stiff in bending.

		AS4/ 3501-6 [21]	AS4/ APC2 PEEK	AS4/ 3502 [39]	IM6/ PEEK	IM6/ 3501-6 [39,40]	SE84 [41]	T700/ RS-36 [42]
Density [g/cc]	ρ	1.58	1.6	1.57	1.56	-	-	-
Longit. Modulus [GPa]	E_1	126	138	133	160.6	161	124.3	135
Transv. Modulus [GPa]	E_2	11	10.2	9.3	8.2	9.65	8.14	10.3
Shear Modulus [GPa]	G_{12}	6.6	5.7	3.74	4.14	5.2	4.49	4.4
Poisson's ratio	ν_{12}	0.28	0.3	0.34	0.31	0.3	0.32	0.34
Poisson's ratio	ν_{23}	0.4	-	0.46	0.45	-	-	-
Longit. Tens. Str. [MPa]	F_{1t}	1950	2070	1778.8	2337.3	2379	2751	2200
Transv. Tens. Str. [MPa]	F_{2t}	48	86	53.5	46.9	-	-	-
L. Compr. Str. [MPa]	F_{1c}	1480	1360	1406.5	1000	1752	1180	1900
T. Compr. Str. [MPa]	F_{2c}	200	638	238.5	-	-	-	-
Shear Str. [MPa]	F_6	79	186	102	119	-	-	-
Shear Str. [MPa]	F_4	-	150	-	-	-	-	-
Ult.[a] L. Tens. Strain [%]	ϵ_{1t}	1.38	1.45	1.24	1.46	0.65	1.2	1.63
Ult. T. Tens. Strain [%]	ϵ_{2t}	0.436	0.88	0.55	0.6	-	-	-
Ult. L. Comp. Strain [%]	ϵ_{1c}	1.175	1.67	1.62	0.8	0.95	0.95	1.41
Ult. T. Comp. Strain [%]	ϵ_{2c}	2	1.85	-	-	-	-	-
Ult. Shear Strain [%]	γ_{6u}	2	-	5.1	-	-	-	-
Toughness Mode I [J/m^2]	G_{Ic}	220	1700	189	960	-	-	-
Toughness Mode II [J/m^2]	G_{IIc}	-	2000	570	-	-	-	-
Longit. CTE [ppm/°C]	α_1	-1	0.5	-0.89	-0.09	-	-	-
Transv. CTE [ppm/°C]	α_2	26	30	23	28.8	-	-	-
Stress-free Temp. [°C]	SFT	177	143	208	271	-	-	-
L. Moist. Exp. [ppm][b]	β_1	0	-	0	-	-	-	-
T. Moist. Exp. [ppm]	β_2	0.2	31	46.7	-	-	-	-
Fiber Vol. Fraction	V_f	0.6	0.61	0.59	0.55	-	-	-
Void Content	V_v	-	0.005	0.001	0.002	-	-	-
Fiber Misalignment [deg]	s_α	1.7	2.74	-	1.52	-	-	-
Ply Thickness [mm]	t_k	0.125	0.125	0.139	0.125	-	0.28	0.312
tr(Q) [GPa][c]		151.1	160.6	150.9	177.9	182	142.3	155.4
G' [GPa][c]		26.34	30.06	30.53	36.99	36.24	27.53	30.48

[a]Ultimate. Also called "strain-to-failure." [b]ppm=10^{-6}.
[c]Calculated in Section 6.5 using properties listed above.

Figure 2.7: Typical carbon fiber composite mechanical properties, 1 [17]

Symbol[a]	Units	T300/ 914-C [21]	T800/ 3900-2 [43]	IM7/ 8551-7 [44]	IM7/ 8552	IM7/ 977-2 [43]	IM7/ MTM45 -1 [45]	IM6/ Avimid K [1,46,47]	T300/ 934 [1,46,47]
ρ	[g/cc]	1.57	1.61	1.56	1.55	1.6	-	-	-
E_1	[GPa]	138	155.8	151	171.4	142	157.9	134	128
E_2	[GPa]	11	8.89	9	9.08	9.17	7.7	9.8	7.2
G_{12}	[GPa]	5.5	5.14	5.6	5.29	4.79	3.6	5.5	4
ν_{12}		0.28	0.3	0.3	0.32	0.32	0.36	0.3	0.3
ν_{23}		0.4	0.064	0.184	0.4[b]	-	0.4	0.361	0.501
F_{1t}	[MPa]	1500	2414	2562	2326.2	2537	2465	2326	1500
F_{2t}	[MPa]	27	70.3	73.8	62.3	71.72	52	37	27
F_{1c}	[MPa]	900	917	916	1200.1	908	1252	1000	900
F_{2c}	[MPa]	200	-	-	199.8	-	193	200	200
F_6	[MPa]	100	267	241	92.3–120	281	48	63	100
F_4	[MPa]	-	-	-	137.2	-	-	-	-
ϵ_{1t}		1.087	1.36	1.6	1.62	1.6	-	-	-
ϵ_{2t}		0.245	0.88	0.9	-	0.88	-	-	-
ϵ_{1c}		0.652	0.6	0.72	0.94	0.69	-	-	-
ϵ_{2c}		0.182	-	-	-	-	-	-	-
γ_{6u}		4	-	-	3.22	-	-	-	-
G_{Ic}	[J/m^2]	220	-	-	277	-	255.1	258	208
G_{IIc}	[J/m^2]	-	-	-	788	-	508.1	-	-
α_1	[ppm/°C][c]	−1	-	-	−5.5	-	−5.5	−0.09	−0.09
α_2	[ppm/°C]	26	-	-	25.8	-	28.5	28.8	28.8
SFT	[°C]	120	-	-	176	-	180	-	-
β_1	[ppm]	-	0.0095	-	-	-	-	-	-
β_2	[ppm]	-	0.321	-	-	-	-	-	-
V_f		0.6	0.649	0.573	0.591	0.6	0.587	-	-
V_v		-	0.001	-	-	-	-	-	-
s_α	[deg]	-	1.75	1.27	1.59	-	-	-	-
t_k	[mm]	0.125	0.14	0.159	0.125	-	0.14	0.144	0.144
tr(Q) [d]	[GPa]	160.9	175.8	172.1	192	162.8	173.9	155.8	143.9
G' [d]	[GPa]	30.4	34.9	33.26	38.62	31.78	36.67	29.21	28.89

[a]See Table 1.3 for nomenclature. [b]G_{23}=2.8–5.9 MPa (reported in source).
[c]ppm=10^{-6}. [d]Calculated in Section 6.5 using properties listed above.

Figure 2.8: Typical carbon fiber composite mechanical properties, 2 [17]

Also given in the primer was a brief introduction to the different ways one can create a laminate stacking sequence. It is in our interest to keep the design space as broad as possible such that we converge on globally optimal solutions. However, we still only wish to perform the study on feasible and not overly complicated solutions. Then, the only constraint that will be placed on the laminate stacking sequence is that we will only consider symmetric sequences. This is to avoid

the complications arising from using asymmetric laminates. The following section will explore the effect of ply orientation and the number of plies for a particular laminate thickness.

2.5 Preliminary Composite Design Guidelines

Figures 2.7 and 2.8, list 30 different properties of various composite materials. For the scope of this thesis, we are interested in the optimal design arising from the nominal loading cases at room temperature and neglecting any humidity effects. We are also more interested in achieving a stiff design (to minimize deflections) and therefore, we can put aside the strengths of composite materials for now. For this, we only need the first 5 rows of mechanical properties: the density, longitudinal and transverse Youngs modulus, shear modulus, and Poisson's ratio. This is sufficient to perform linear elastic analysis, as well as quantify the mass of each structure. Focusing on these material properties, the following Table 2.2 provides the range.

Table 2.2: Carbon fiber composite material property ranges for sensitivity study

Property	Min	Max
Density (kg/m^3)	1,550	1,610
E_1 (MPa)	124,300	171,400
E_2 (MPa)	7,200	11,000
G_{12} (MPa)	3,600	6,600
ν_{12}	0.28	0.36

The no-load case causes the most deflections in the structure due to the lack of centrifugal stiffening and optimizing for stiffness for this case is paramount. Using this material design space, 5 evenly spaced values of each property were looked at and a total of $5^4 = 625$ unique designs were evaluated for maximum displacement using virtual work on an arbitrarily chosen quasi-isotropic simply supported square plate with an evenly distributed out-of-plane loading. To compare the effects of varying one design variable over another, factor effects plots were generated. In case the reader is not familiar with factor effects or "sensitivity" plots, these can be used to obtain one

plot per design variable that allows for a fair comparison. The plot with the largest slope shows the largest relative effect of that design variable while having no slope (horizontal line) indicates little or no effect of that design variable on the performance metric of interest. In this case, are 5 points on each plot, and data points computed on the plot are calculated by averaging the variation of all other design variables while keeping that specific design variable of interest constant. For example, in Fig. 2.9a using longitudinal stiffness E_1, the domain is from 124.3 GPa to 171.4 GPa. Since there are 5 data points to consider, the values of E_1 considered are 124.3, 136.1, 147.9, 159.6, and 171.4 GPa. The first data point given in the E_1 plot in Fig. 2.9arepresents the average of all deflections of plate designs with every variation of E_2, G_{12}, and ν_{12} while holding E_1 constant at 124.3 GPa. This process is repeated for each data point in each plot.

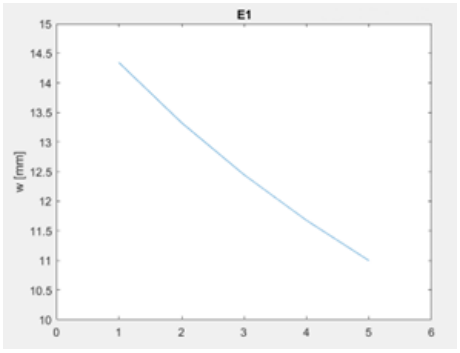

(a) E_1 sensitivity

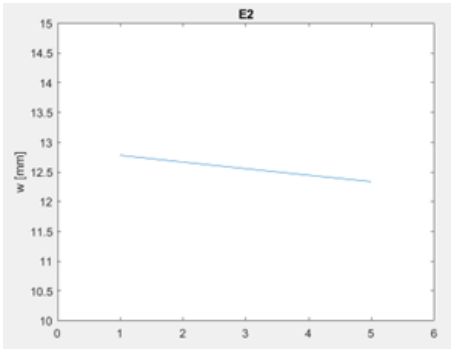

(b) E_2 sensitivity

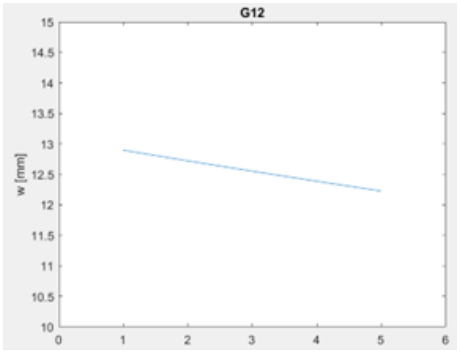

(c) G_{12} sensitivity

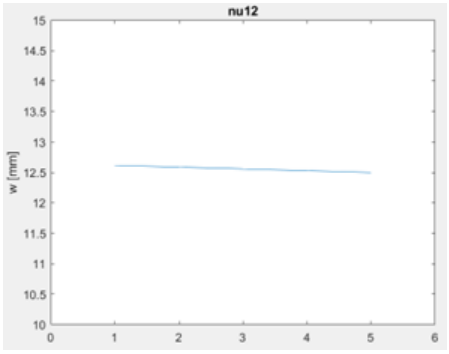

(d) ν_{12} sensitivity

Figure 2.9: Factor effects plots of composite material properties on axial deflection

Based on the factor effects plots, E_1 has the greatest effect in determining deflections due to the relatively dominant slope. Therefore, this property should be prioritized in material selection. In contrast, ν_{12} has nearly a flat slope, so it can be concluded that this property is not very important

in overall stiffness, and we can eliminate this design variable from future consideration. Both E_2 and G_{12} have a small slope, so these should fall under secondary consideration in material selection in order to find an optimal design.

From the materials given in Figures 2.7 and 2.8, IM7/8552 has the largest longitudinal stiffness (E_1). The rest of the thesis will then focus on this composite material in the subsequent design and analysis.

The two load cases introduced in Section 2.2 are evenly distributed along the edges. Because of this, having the structure stiffer in a certain orientation will result in an inefficient design. Hence, a quasi-isotropic layup would give minimum deflection, and therefore, only quasi-isotropic ply orientations were considered. However, it is important to acknowledge the fact that a quasi-isotropic laminate is not the same as an isotropic laminate when bending is involved [17]. Then, there may be a certain sequence in stacking quasi-isentropic laminates which result in an isotropic design. Two quasi-isotropic layups are proposed in Table 2.3 and with accompanied FEA deflection results in Fig. 2.10. A value for the chosen geometry, material properties, number of plies and their orientations are kept constant. The only thing variable is the sequence in which these plies are stacked. Note that in the "Right" FEA model given in Table 2.3 and shown in Fig. 2.10, perpendicularly oriented plies neighbor each other. Alternatively, in the other case, similarly oriented plies neighbor each other. As shown in Table 2.3, although the same number of plies and ply orientations are used, a different stacking order gives almost half of the deflection! Then, it can be concluded that when directly neighboring plies are oriented perpendicularly to each other, an optimally stiff structure is achieved.

Table 2.3: Ply sequence study

FEA Model	Laminate Stacking Sequence	Maximum Deflection (mm)
Left	$[18,36,54,72,90,-72,-54,-36,-18,0]_s$	0.03925
Right	$[0,90,18,-72,36,-54,54,-36,72,-18]_s$	0.02481

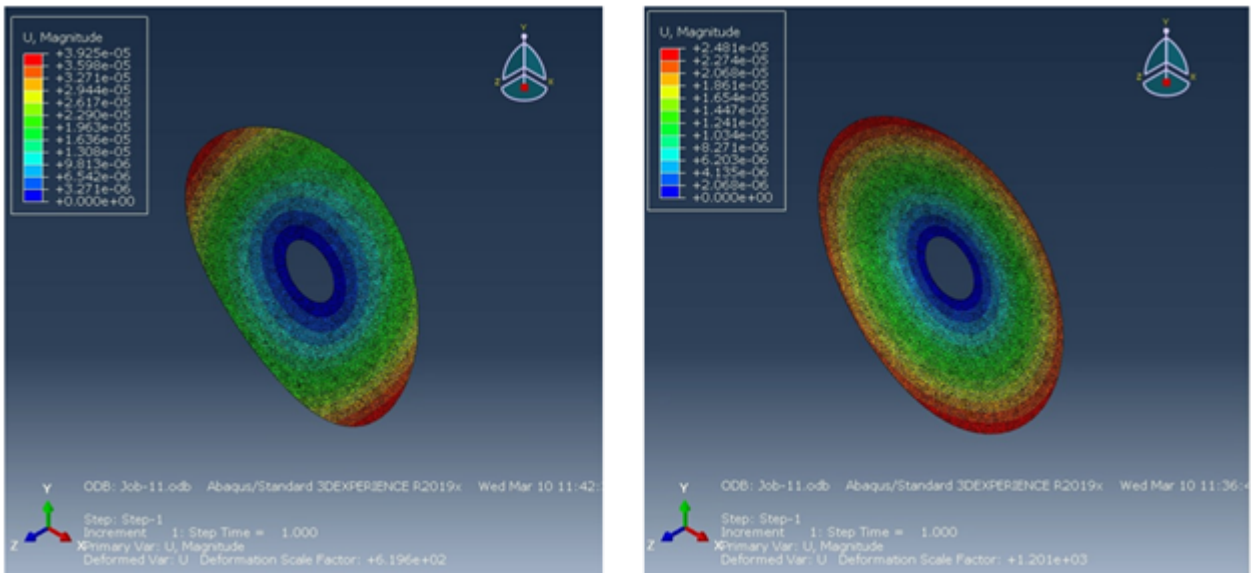

Figure 2.10: Output of ply sequence study. Laminate asymmetrically stiff in bending in left, laminate with axi-symmetric bending stiffness in right.

By establishing the guidelines that we need quasi-isotropic layups and perpendicular plies, we can investigate the effect of the number of plies used for a constant laminate thickness. Limiting our consideration to this stacking sequence: $[0,90,45,-45]_{n,s}$ where n is the number of times that sequence is repeated, Table 2.4 is generated and Fig. 2.11 shows the maximum deflection resulting from FEA.

Table 2.4: Ply repetition study

n	Ply Thickness (mm)	Overall Thickness (mm)	Maximum Deflection (mm)
1	2.25	18	0.1898
2	1.125	18	0.1497
4	0.5625	18	0.1373
6	0.375	18	0.1342

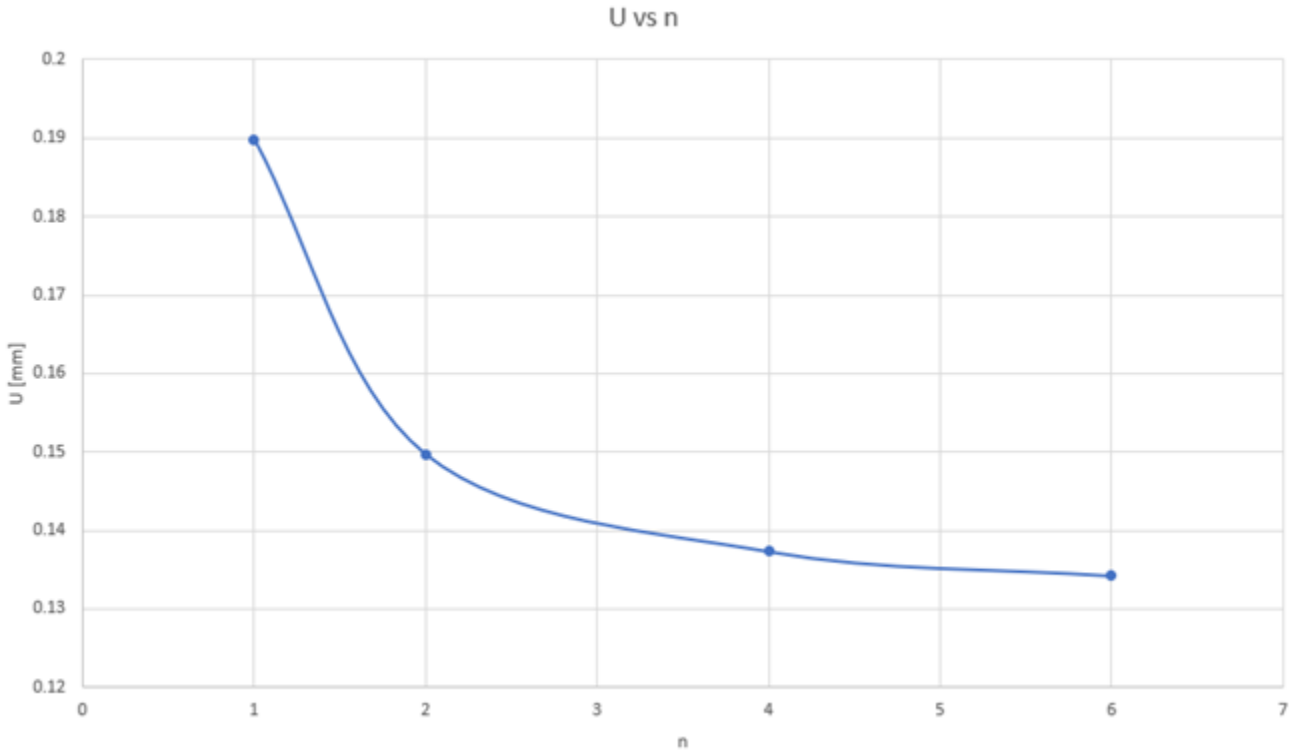

Figure 2.11: Ply repetition study comparing stacking sequence repetitions to maximum axial deflections

It is important to note that quasi-isotropic layup guarantees similar mechanical properties in all in-plane directions. However, because we are primarily dealing with a transverse load out of the plane, quasi-isotropic layups do not guarantee similar bending stiffness properties within the plane. This means a non-isotropic laminate that is composed of a quasi-isotropic layup can exist [17]. However, the results in Figure 2.11 suggest that by repeating the plies more often, the structure acts more isotropic in bending and results in minimal overall deflections. Ideally, an infinite number of repetitions would yield a perfectly isotropic structure made of composites, but because plies can only be so thin (about 0.125 mm per lamina), a practical limit exists. Figure 2.11 suggests that repeating the stacking sequence at n = 4 or more will yield a sufficiently isotropic design.

2.6 Structural Design Configurations

Multiple structural design configurations are also explored. This section introduces the geometry as well as the design space of each. From Table 1.1, motor parameters which the structure must

satisfy are given. Each configuration must then be able to support magnets around the periphery and the magnet array has an inner diameter 220 mm, outer diameter 270 mm, and height of 10mm. For supporting the large centrifugal forces, each configuration consists of a 2mm thick carbon fiber retaining ring wrapped around the outer perimeter of the magnets. Chapter 3 will describe the analysis performed on each, the results from the mass optimization study, and compare the configurations against one another.

2.6.1 Solid Disk Configuration

The first configuration considered was a basic composite structure, essentially a solid disk with a circular cutout feature for the shaft and a pocket feature around the periphery for mounting the magnet array. The model we designed is shown in Figure 2.12. The in-context cutout view is given in Figure 2.13, with the magnets, retaining ring, and shaft included.

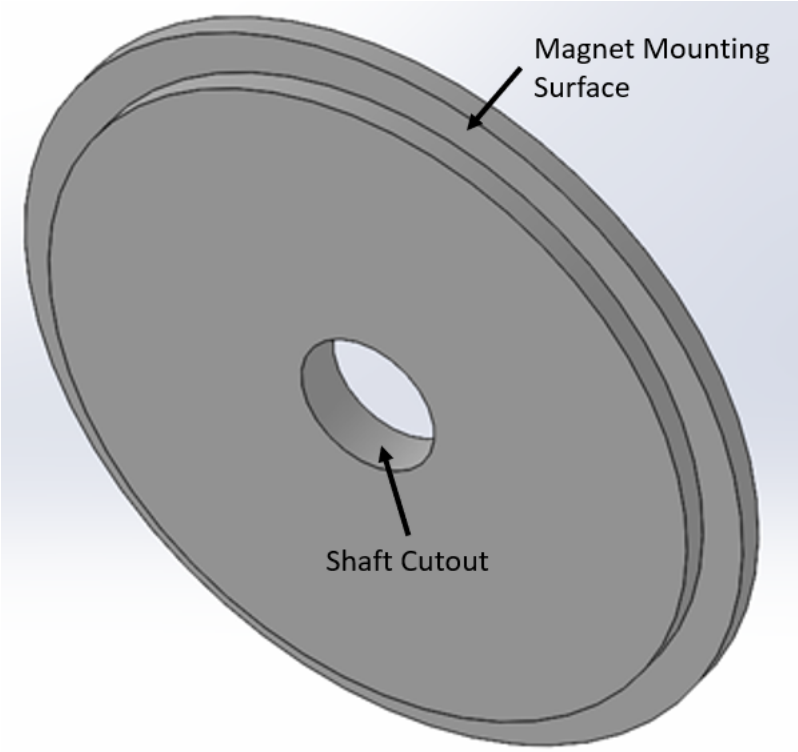

Figure 2.12: Isometric view of solid disk rotor structure.

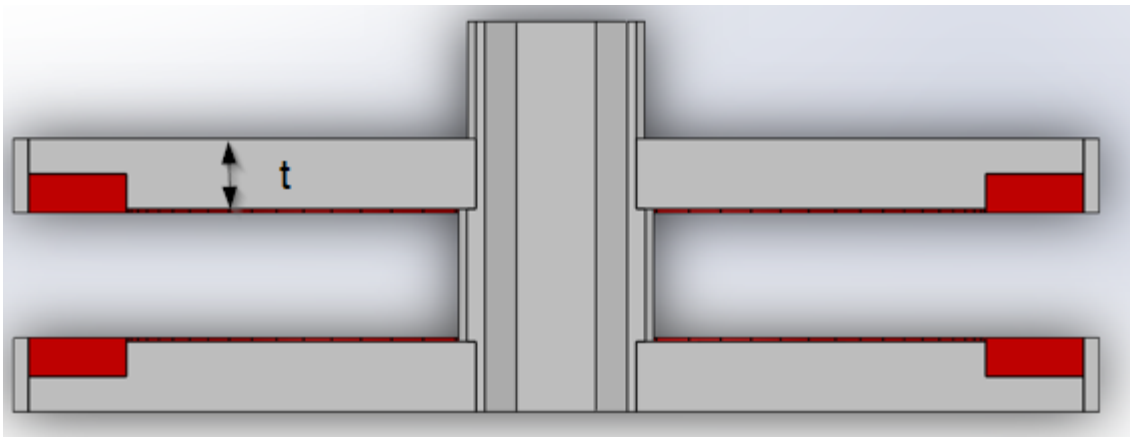

Figure 2.13: Cutout view of solid disk rotor with magnets in red.

The layup used in this configuration follows the guidelines given in Section 2.5. A quasi-isotropic layup is given with the laminate stacking sequence $[0,90,45,-45]_{4,s}$. In this layup, neighboring pairs of plies are perpendicular, and the sequence repeats itself 4 times before reflecting about the neutral axis for symmetry.

Because most of the design variables at this time are constrained (rotor outer diamater [OD], shaft OD, laminate stacking sequence, retaining ring design, etc.), and considering the fact that this type of structure is relatively simple, there is only one design variable left to characterize performance – the overall thickness. This parametric study is performed by varying the thickness t labeled in Figure 2.13, and the laminate stacking sequence remains the same; however, the ply thickness should vary with the overall thickness of the laminate. Note that, in reality, carbon fiber plies have a discrete thickness (usually around 0.125mm), and typically cannot continuously vary as they do in this study. However, the following analysis is meant to only provide a theoretical benchmark for performance which should be similar to that of a more practical design.

2.6.2 Cutout Disk Configuration

The next rotor structural configuration is slightly more complicated than the former. This configuration consists of the same quasi-isotropic laminate as before, but this time contains cutouts with differing geometries to improve the overall bending stiffness of the structure. For example, from beam theory, Fig. 2.14 shows the cross-section of a rectangular beam and the corresponding

moment of inertia I. It can be seen that by increasing the height of the beam, the moment of inertia – and hence the bending stiffness – increases at a cubic rate. The underlying idea is that if we cut out some of the mass of the solid disk and then re-apply the same mass as added thickness, then for the same weight a stiffer structure could emerge. Figure 2.15 shows a top view of this structure, while Fig. 2.16 puts this design into the context of the overall assembly.

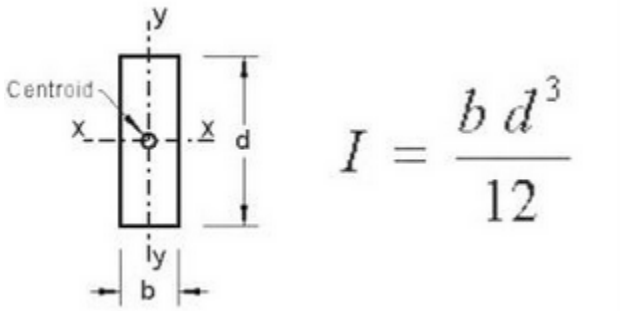

Figure 2.14: Rectangular beam with bending moment of inertia formula [32]

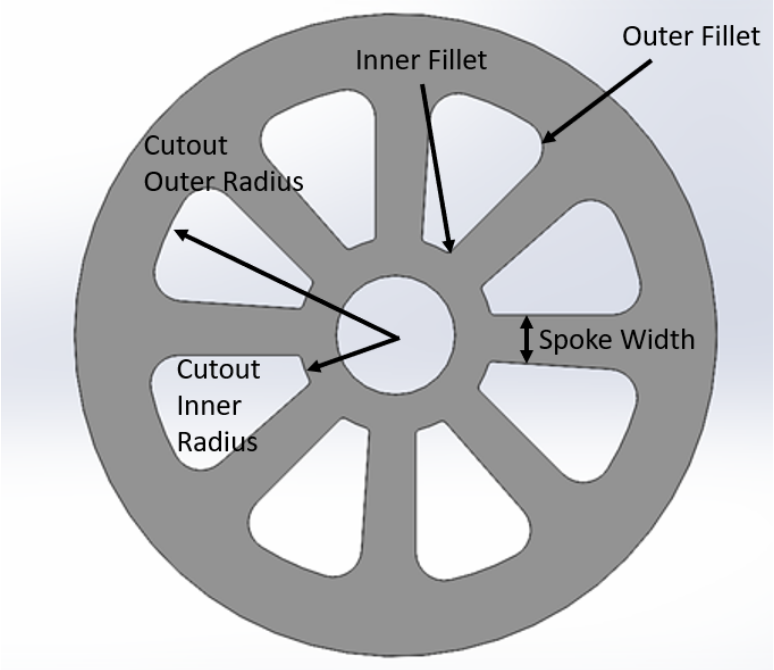

Figure 2.15: Top view of cutout disk rotor

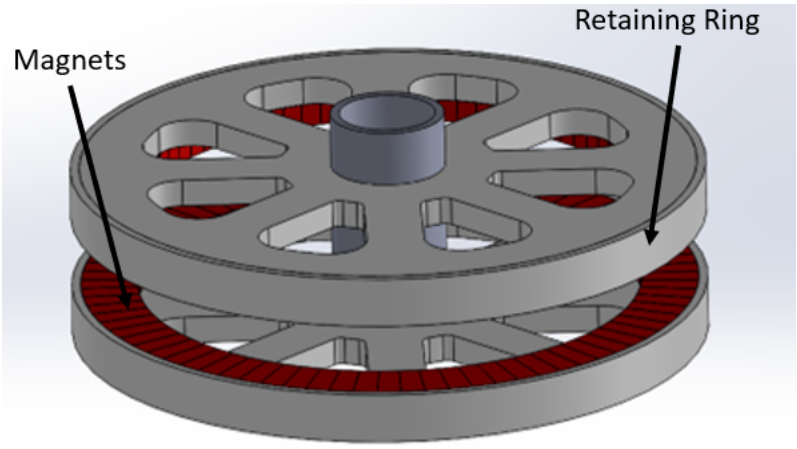

Figure 2.16: Isometric view of cutout disk rotor with magnets in red

In addition to the varying disk thickness, in this design the cutout geometry also varies. This includes the following design variables: the number of spokes resulting from the cutouts, the width o f the spokes from the cutout, the inner radius of the cutout, the outer radius of the cutout, the inner fillet size of the cutout, and the outer fillet size of the cutout. This means we now have seven design variables to consider for this configuration.

2.6.3 Cutout Disk with Stiffeners Configuration

The previous design seeks to take advantage of optimally increasing bending stiffness by adding cutouts to the disk geometry. However, because of the limitation of using a quasi-isotropic laminate in the entire structure, the advantages of carbon fiber's anisotropy are not leveraged. This third configuration attempts to introduce some anisotropic structure to add to the stiffness. The way this particular configuration is achieved is by adding unidirectional stiffeners along the length of the spokes of the Cutout Disk Configuration. An example of this is shown in Fig. 2.17.

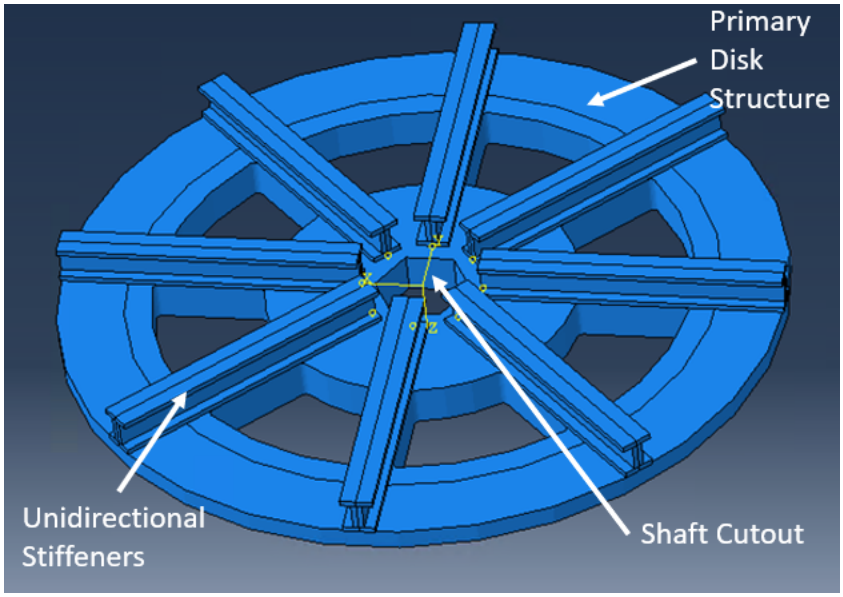

Figure 2.17: Isometric view of cutout disk with stiffeners rotor structure

In addition to the same design variables involved in the space of the Cutout Disk, additional variables related to the stiffeners are included. These are the stiffener cross section (box, I beam, L beam, hat, etc.), stiffener flange width, stiffener web height, stiffener thickness t, and stiffener length. The stiffener cross-section design variables are indicated in Fig. 2.18. This means that there are a total of 7 + 5 = 12 design variables to consider. However, the assumption is made that the flange width of the stiffener is equal to the width of the spoke underneath, and therefore, one design variable can be eliminated. Also, the stiffener length is arbitrarily held constant from the edge of the rotor disk at 100 mm long each. This reduces the total number of design variables down to ten for the analysis.

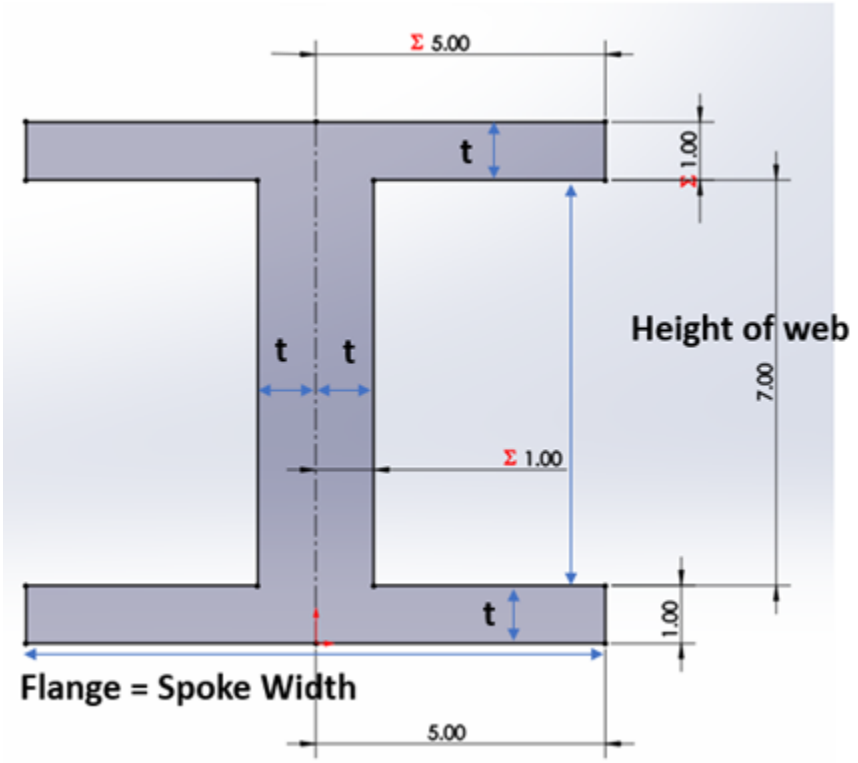

Figure 2.18: Beam cross section with design variables labeled

An important note regarding unidirectional layups is that it is poor practice to design a composite part with 100% unidirectional plies. The reason for this is that it is easy for crack growth to propagate along the length of the fibers. As a rule of thumb, it is good practice to always have some off-axis plies to help support the structure. In our case, we introduce 10% of 90° plies, 10% of 45° plies, and 10% of -45° plies in each of our "unidirectional structures". So this means that from now on when we refer to unidirectional layups, we really mean 70% unidirectional layups.

2.6.4 Unidirectional Spoked Disk Configuration

The final configuration to consider is a close derivative of the previous design. In this configuration, unidirectional stiffeners are still used to help promote bending stiffness. However, in this case, the quasi-isotropic region below these stiffeners is completely eliminated. This results in a model composed of several different parts, each with its own functions. These regions are shown in Fig. 2.19, with an arbitrary mass breakdown of each in Table 2.5 (normalized to 1000 g). The idea behind this is that by dividing the structure into these 3 main sections, more design variables

may exist to help optimize each section according to some unique function they achieve. These sections are 1) the magnet mounting disk, 2) the spokes, and 3) the root. The magnet mounting disk simply holds the magnets, the spokes transfer the load to the root, and the root transfers the load to the shaft while providing a stable root condition. The magnet mounting disk has the largest area and accounts for over half of the mass, despite least affecting the overall structural deflections due to being the farthest from the root. This allows parts that minimally affect the overall deflection reduction to have low mass while also introducing unidirectional box beams along the spokes to maximize bending stiffness. Figure 2.20 shows what this type of structure looks like.

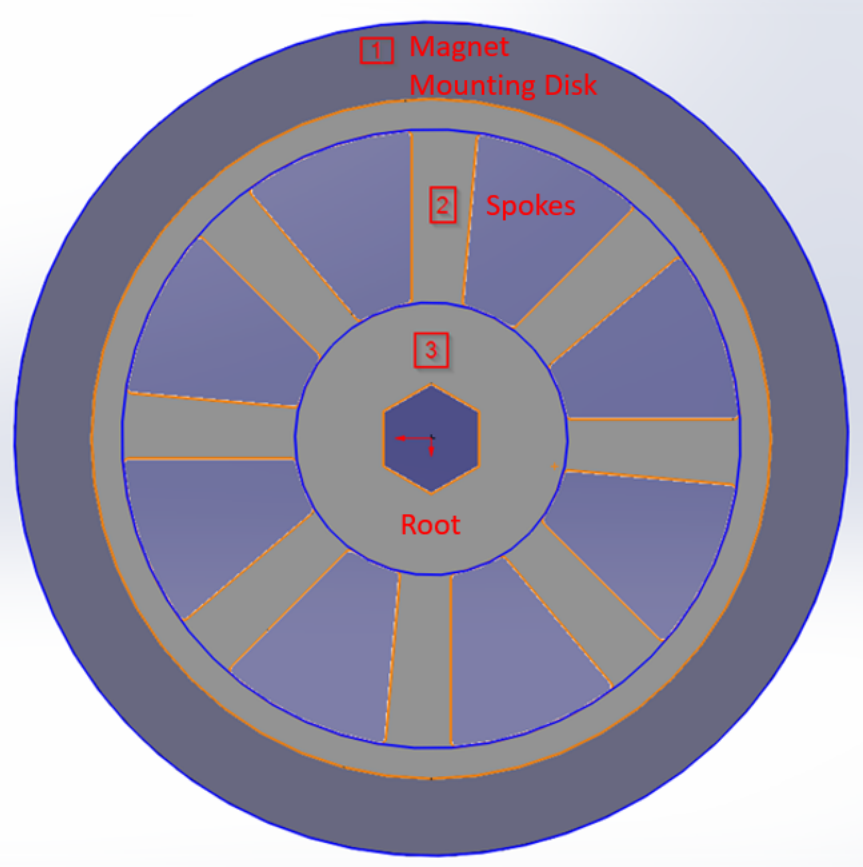

Figure 2.19: Breakdown of rotor structure segments

Table 2.5: Rotor structure segment mass breakdown

Section	Mass (g)
1	539
2	284
3	177

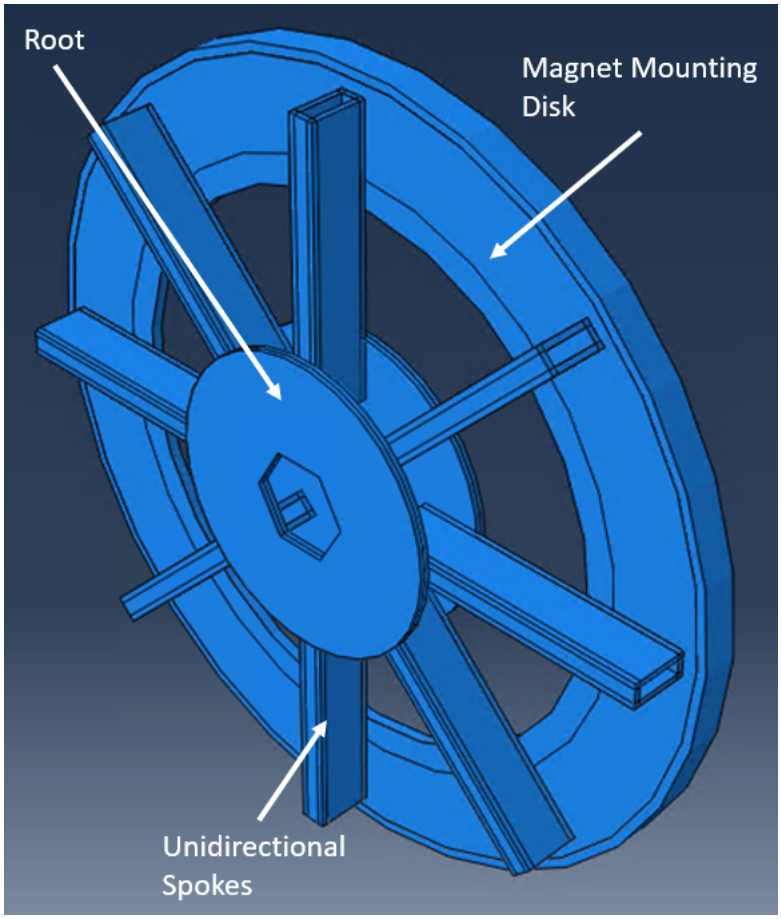

Figure 2.20: Isometric view of unidirectional spoked disk rotor

The design variables are similar to the previous configuration, except now that the cutouts do not exist in the quasi-isotropic layups to make spokes, some previous variables can be eliminated such as the inner and outer fillets. It is best to consider the design variables section by section.

Section 1, the magnet mounting disk, is essentially a quasi-isotropic layup that is a very large annulus. This section contains all the parameters regarding the positioning and support of the

magnets. This fixes the outer diameter to 270mm. However, the inner diameter and thickness are still variable. Thus, this section has only 2 design variables.

Section 2, the spokes, has many of the same variables as in the Cutout Disk with Stiffeners configuration. These spokes are also unidirectional, and the length is fixed here in a similar fashion. This means that the geometric variables are then the stiffener cross-section, stiffener flange width, stiffener web height, and stiffener thickness t. Additionally, there exists the discrete variable of the number of stiffeners. Thus, this section has 5 different variables.

Section 3, the root, is also a simple structure consisting of essentially two quasi-isotropic circular segments with a shaft hole in the center. These plates "sandwich" the spokes to provide maximal stiffness. The variables to consider here are the outer diameter and the thickness. The shaft hole is a constraint driven by the shaft design and will remain constant in the studies. This means this section has only two design variables.

Thus, there are a total of 2 + 5 + 2 = 9 variables to consider in this design space.

2.6.5 Design Variable Summary

There are 4 unique configurations to analyze, and for convenience the summaries of each design variables are listed in the tables below:

Table 2.6: Solid disk design space

Design Variable	Lower Limit	Upper Limit
Disk Overall Thickness	6 mm	14 mm

Table 2.7: Cutout disk design space

Design Variable	Lower Limit	Upper Limit
Disk Overall Thickness	12 mm	18 mm
Number of Spokes	4, 6, 8, 10	
Spoke Width	2 mm	50 mm
Cutout Inner Radius	50 mm	80 mm or Outer Radius
Cutout Outer Radius	60 mm or Inner Radius	110 mm
Inner Fillet	2 mm	10 mm
Outer Fillet	2 mm	30 mm

Table 2.8: Cutout disk with stiffeners design space

Design Variable	Lower Limit	Upper Limit
Disk Overall Thickness	12 mm	18 mm
Number of Spokes	4, 6, 8, 10	
Spoke Width	5 mm	25 mm
Cutout Inner Radius	35 mm	75 mm or Outer Radius
Cutout Outer Radius	60 mm or Inner Radius	100 mm
Inner Fillet	2 mm	10 mm
Outer Fillet	2 mm	30 mm
Stiffener Cross Section Type	T, I, L, Box, Hat	
Web Height	1 mm	50 mm
Stiffener Thickness, t	1 mm	15 mm

Table 2.9: Unidirectional spoked disk design space

Design Variable	Lower Limit	Upper Limit
Root Radius	40 mm	60 mm
Root Thickness	2 mm	10 mm
Beam Height	5 mm	35 mm
Beam Width	5 mm	20 mm
Beam Thickness	2 mm	5 mm
Number of Beams	6, 8, 10	
Beam Cross Section Type	T, I, L, Box, Hat	
Magnet Mounting Disk Inner Diameter	190 mm	210 mm
Magnet Mounting Disk Thickness	3 mm	12 mm

3. ROTOR STRUCTURAL ANALYSIS AND OPTIMIZATION*

This section introduces the models used in the analysis of the four different unique configurations that were introduced in the previous chapter. Each model has a finite element model associated with it and was developed using Abaqus software [33]. A unique and critical feature of using Abaqus is that the models can be generated with a Python script. This enables the user to create scripts for running structural analysis. Furthermore, an optimizer can be used in conjunction with the finite element analysis (FEA) to automatically analyze thousands of designs while searching for the optimal mass design. In this thesis, an optimizer was generated using Python and Abaqus FEA. The optimization script follows a genetic algorithm sequence, which will be introduced in the first section. Then each FEA model and optimization results are sequentially introduced in the following sections using the four different rotor structural configurations. Then, the best performing configuration will be re-optimized using Aluminum and Titanium for comparison purposes. Finally, all of the results are summarized and compared against each other.

It was found that in each configuration, only the no RPM load case needed to be considered. Also, in general, each structure's mass was determined by overall stiffness (or maximum allowable deflections) as opposed to stress. Very rarely the models generated would violate the stress constraints, and when they did the optimization script would remove those candidates from the analysis. Hence, the study in the following section will primarily focus on structural stiffness and overall deflections for the no RPM load case only since that is the worst-case scenario for the rotor structure.

3.1 Genetic Algorithm Optimizer

The four different configurations given in section 2 will be mass-optimized and then compared with each other. While the first configuration, the solid disk, only has one design variable and

*Part of this chapter is reprinted with permission from "Design of a Carbon Fiber Rotor in a Dual Rotor Axial Flux Motor for Electric Aircraft" by Chase Wiley, 2022. 2022 IEEE Energy Conversion Congress and Exposition (ECCE), Copyright 2022 by The Institute of Electrical and Electronics Engineers, Incorporated.

therefore, determining optimal solutions are trivial, while the other configurations have up to ten design variables, which makes the design space very large and difficult to find the optimal structure. Hence, an optimization algorithm is needed to help find optimal solutions in this large design space. The algorithm need only target single objective optimizations, as the interest is in producing designs with minimal mass that do not break deflection or stress constraints.

The optimization algorithm chosen is a Genetic Algorithm. This particular algorithm will first randomly spawn initial designs within the design space, evaluate performance, then spawn new generations of designs based on the higher performing ones. The general sequence follows:

1. Spawn N designs in the initial generation
2. Evaluate the designs for performance and violated constraints
3. Regenerate new generation of N designs based on best performing designs of the previous generation
4. Repeat steps 2 and 3 until a sufficient number of designs are evaluated

The reader may wish to read more about the Genetic Algorithm in [34]. The genetic algorithm created for this thesis was scripted in Python and works with Abaqus FEA software. The goal is to find the minimum mass designs which do not violate deflection or stress constraints for the no RPM case.

To verify the operation of the Genetic Algorithm, test functions can be employed to determine success. Figure 3.1 shows the mathematical space of three different test functions the algorithm was tested against. In particular, the Beale, Goldstein-Price, and Eggholder functions were used. The formulae are given below and each function's space is represented in Fig. 3.1. The algorithm successfully found solutions to each of these problems before conducting optimization analysis of the different structural configurations.

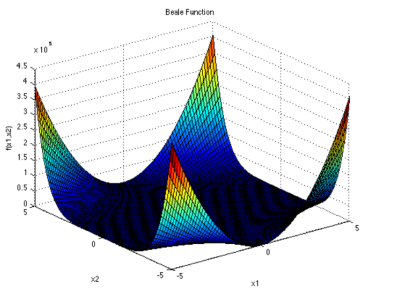

$$f(\mathbf{x}) = (1.5 - x_1 + x_1x_2)^2 + (2.25 - x_1 + x_1x_2^2)^2 + (2.625 - x_1 + x_1x_2^3)^2$$

(a) Beale function [35]

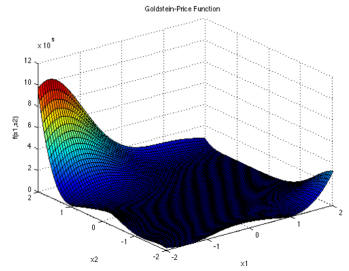

$$f(\mathbf{x}) = [1 + (x_1 + x_2 + 1)^2(19 - 14x_1 + 3x_1^2 - 14x_2 + 6x_1x_2 + 3x_2^2)] \times [30 + (2x_1 - 3x_2)^2(18 - 32x_1 + 12x_1^2 + 48x_2 - 36x_1x_2 + 27x_2^2)]$$

(b) Goldstein-Price function [36]

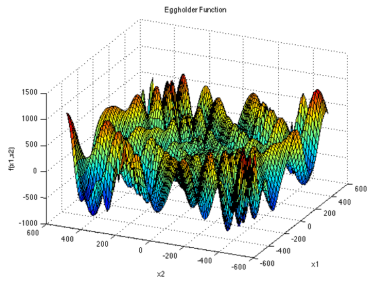

$$f(\mathbf{x}) = -(x_2 + 47)\sin\left(\sqrt{\left|x_2 + \frac{x_1}{2} + 47\right|}\right) - x_1\sin\left(\sqrt{|x_1 - (x_2 + 47)|}\right)$$

(c) Eggholder function [37]

Figure 3.1: Test functions

3.2 Solid Disk Configuration

The solid disk given in Fig. 2.12 is a simple structure with only one design variable to vary: the overall plate thickness. Details surrounding the laminate stacking sequence were given in Section 2.6.1. Essentially a quasi-isotropic layup of $[0,90,45,-45]_{4,S}$ is used in all cases, and ply thicknesses is treated as a continuous variable.

3.2.1 Solid Disk FEA Model

Figure 3.2 shows the model of the solid disk created in Abaqus. The structure is a 2d shell, with a fixed boundary condition to simulate the shaft root condition and an evenly distributed load around the circumference to simulate the loading the structure experiences according to Table 2.1. As shown in Fig. 3.2, three different load components are included to simulate the results of the full RPM case: one simulating axial forces normal to the structural plane, one simulating torque transmission via a force tangent to the circumference, and one acting radially outwards to simulate centrifugal loading. However, since no RPM causes the most deflections, the data points collected

and reported in the following section will only consist of the distributed load acting normal to the plane, which is the attractive force between the magnets and the stator iron and has a magnitude of around 5 kN (loading conditions are discussed in detail in Chapter 2). Figure 3.3 shows a contour plot example of the resulting axial bending deflections of the structure due to this force.

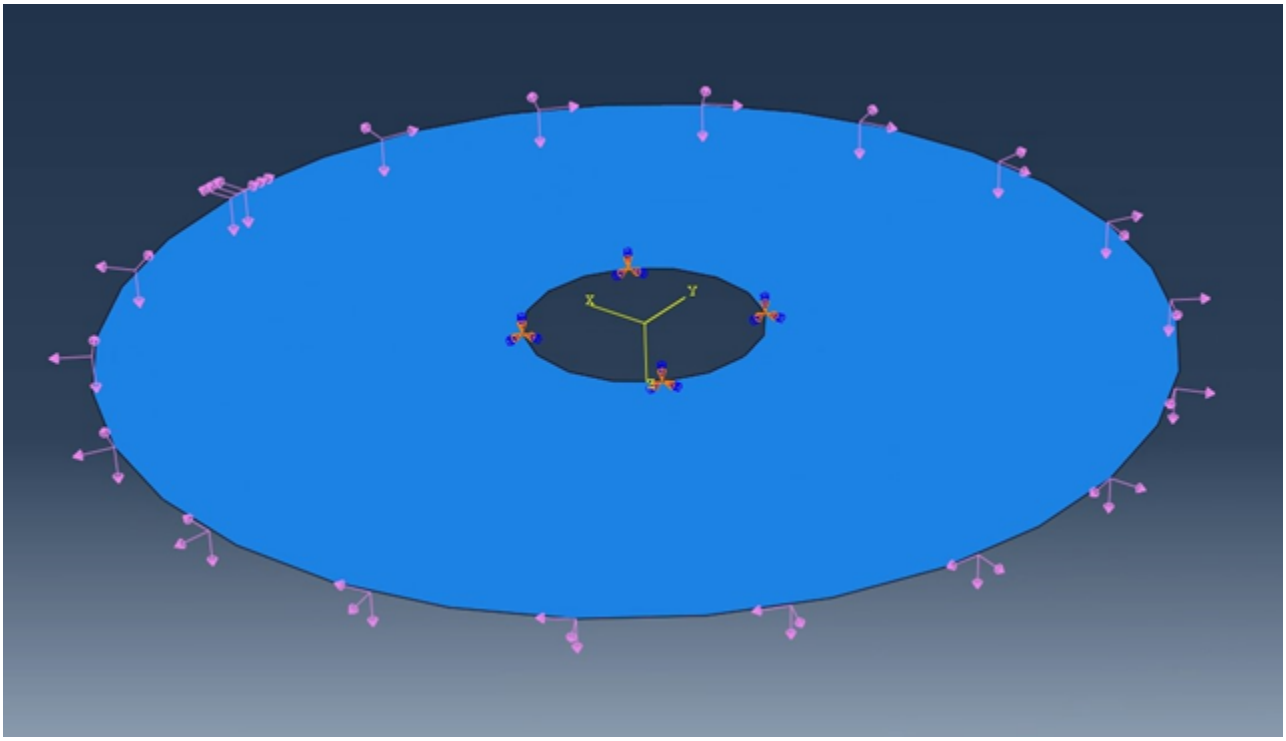

Figure 3.2: Solid disk FEA model

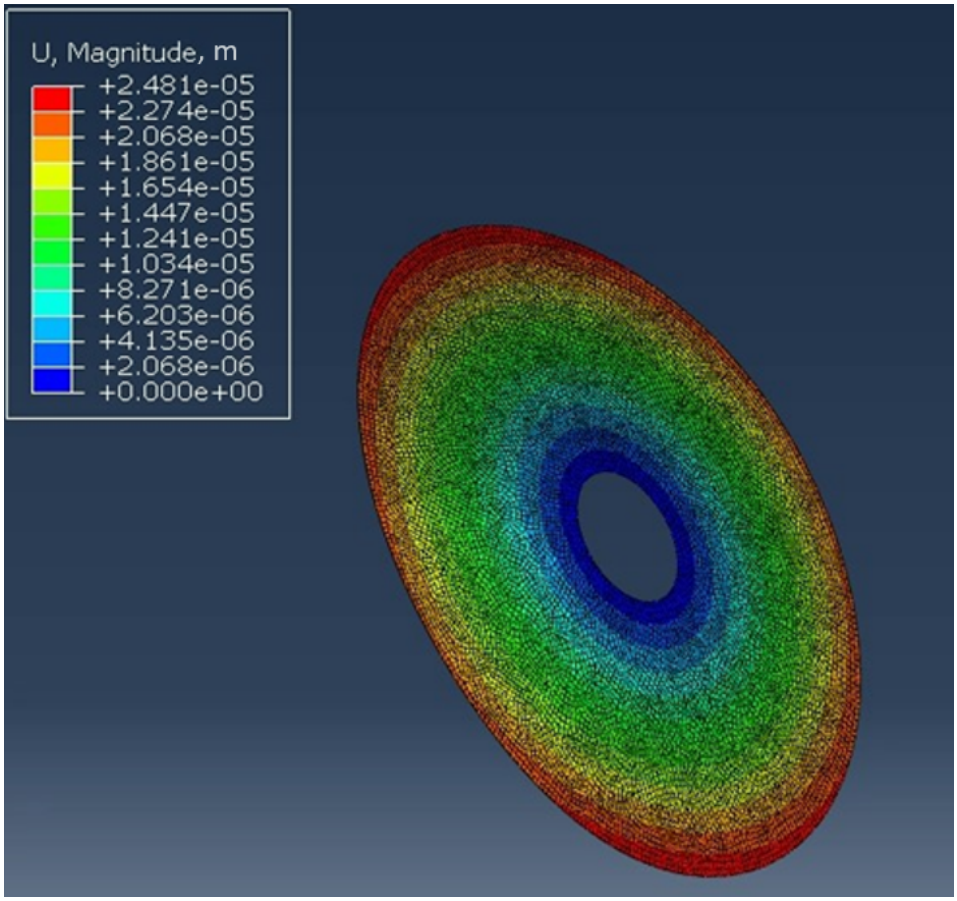

Figure 3.3: Solid disk FEA model with axial deflection output

3.2.2 Solid Disk Optimization

By using the FEA model and only varying ply thickness, the following deflection vs mass plot was obtained for the performance of the solid disk. Because this design space only consisted of one variable, this is the only study necessary to obtain a mass-optimized design. Figure 3.4 plots maximum deflection as a function of rotor mass (which is a function of thickness). To satisfy our deflection constraint of 0.3 mm, a mass of 1,000g is needed.

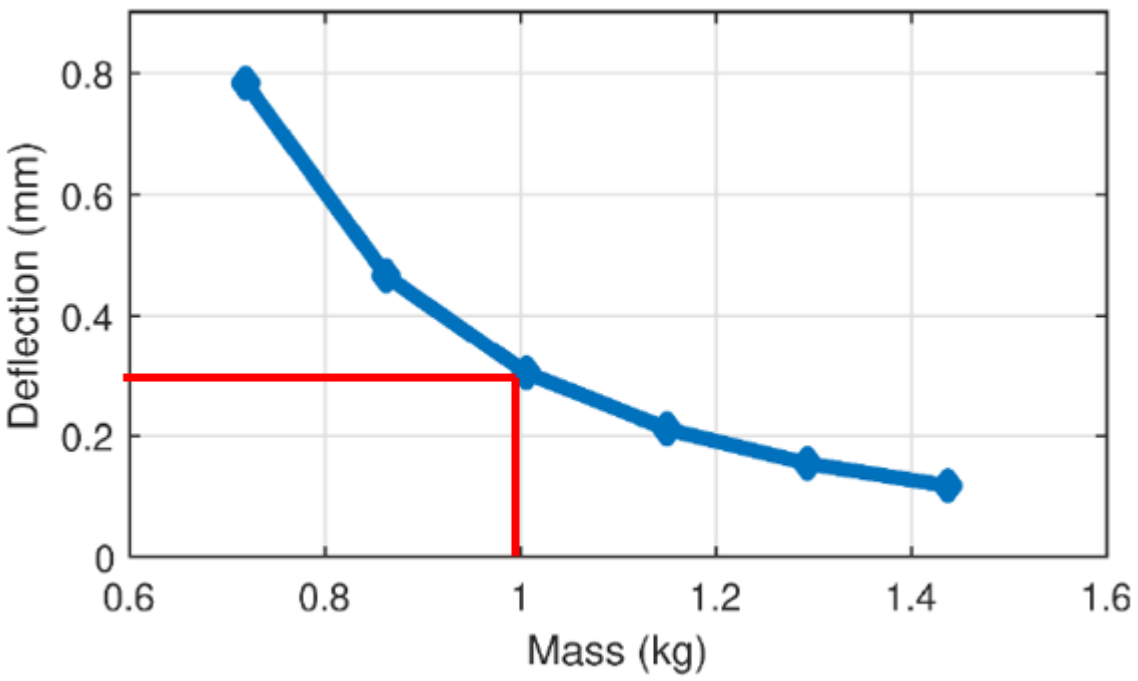

Figure 3.4: Solid disk mass vs maximum axial deflection [18]

3.3 Cutout Disk Configuration

The structure shown in Fig. 2.16 is a solid disk structure with cutouts introduced into it. Due to the added geometry of the cutouts, this configuration has a design space with seven different variables to consider. The design space with the variations of the cutout shapes are represented in Fig. 3.5. Figure 3.6 provides a diagram showing designs with different number of spokes, and Fig 3.7 shows an example of a quasi-isotropic layup with some lamina fibers oriented along the spokes for the 6-spoke configuration. Table 3.1 provides the proper laminate stacking sequence used for each configuration.

Figure 3.5: Example of cutout geometry

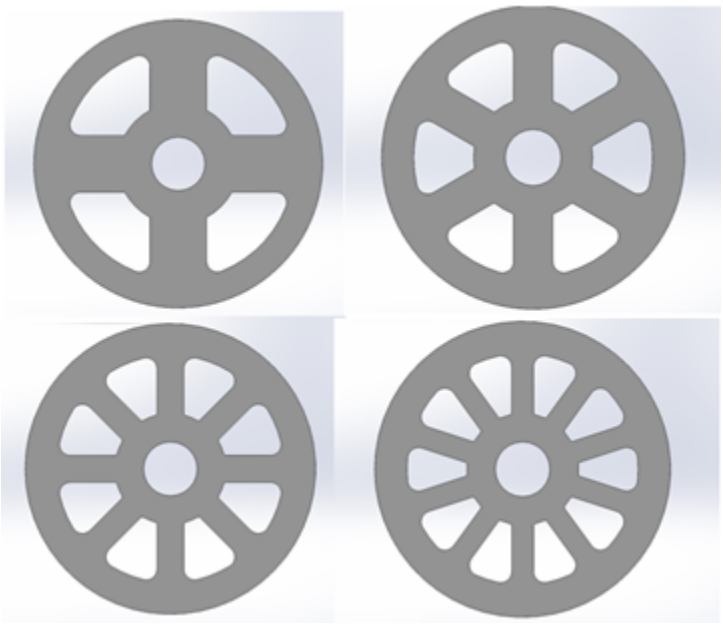

Figure 3.6: Example of 4, 6, 8, and 10 spoked geometry

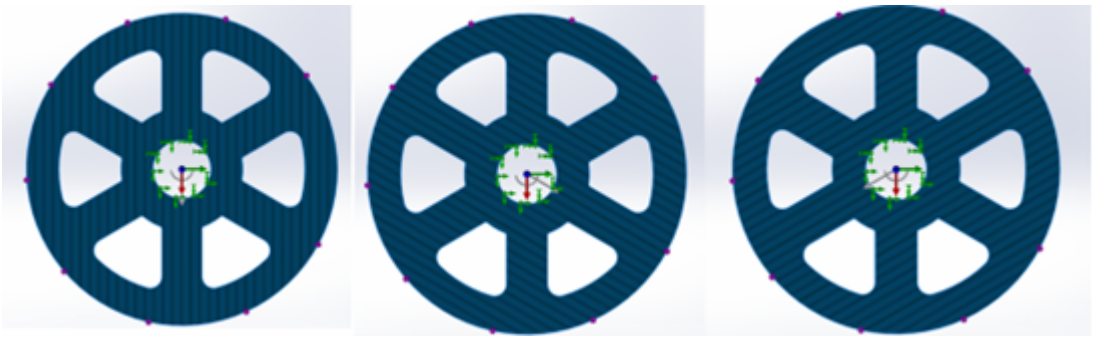

Figure 3.7: Example of cutout spoke and layup orientation

Table 3.1: Laminate stacking sequence for each 4, 6, 8, 10 spoked designs

Number of Spokes	Laminate Stacking Sequence
4	$[0,90]_{4,s}$
6	$[0,60,-60]_{4,s}$
8	$[0,90,45,-45]_{4,s}$
10	$[0,36,-72,-36,72]_{4,s}$

3.3.1 Cutout Disk FEA Model

The Abaqus FEA model created for the cutout disk is shown in Fig. 3.8. Again, this model uses 2D shell elements and considers a load case just like that of the solid disk model: a cantilevered boundary condition at the shaft and a distributed axial load around the circumference of the structure. Figure 3.9 provides an example of a typical FEA output (axial deflections in this case) from this load condition.

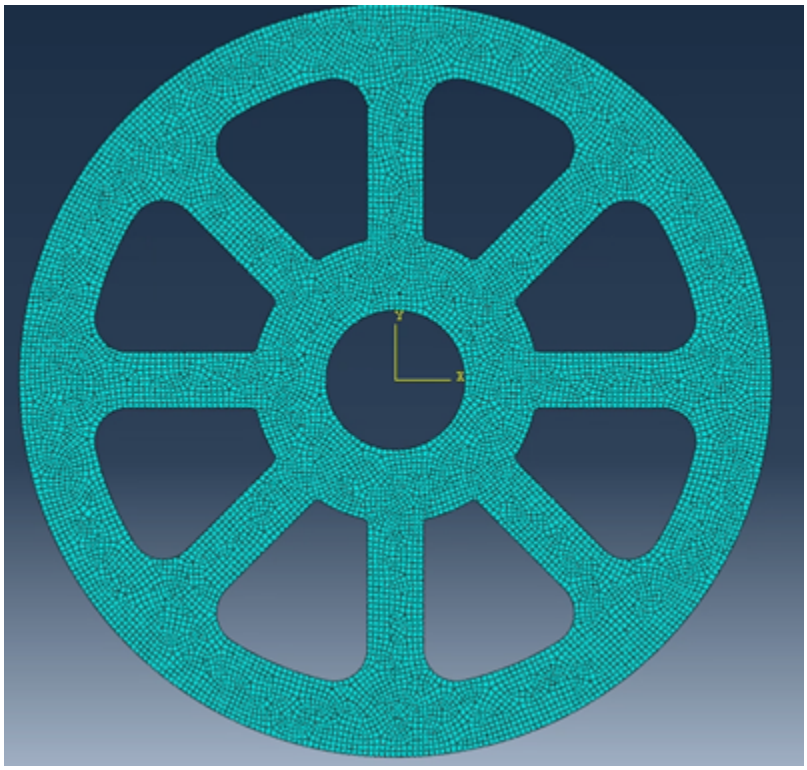

Figure 3.8: Cutout disk FEA model

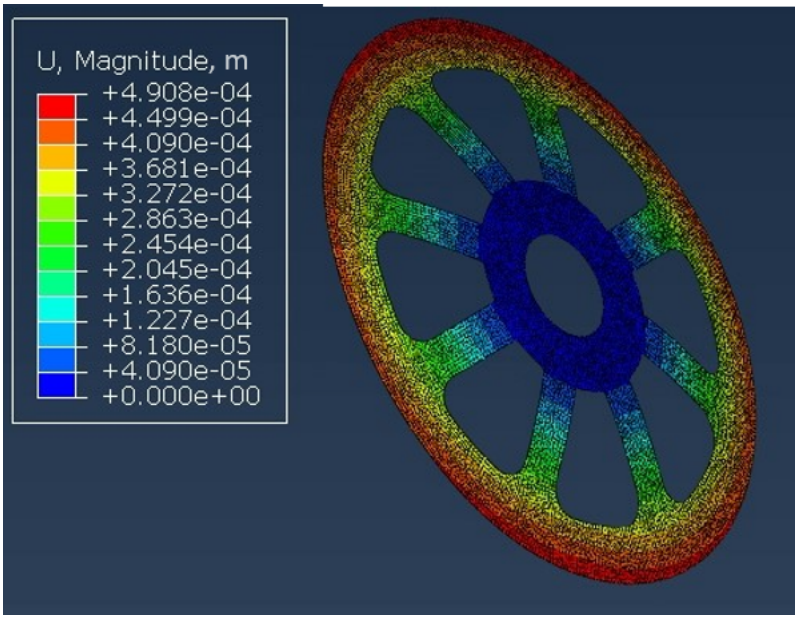

Figure 3.9: Cutout disk FEA model with axial deflection output

3.3.2 Cutout Disk Optimization

For the Genetic Algorithm based optimization study, one design variable is eliminated to significantly reduce the computational time in converging onto an optimal design. This is the number of spokes, as we have a discrete number between 4, 6, 8, and 10 spokes to consider. Towards this, four different designs are considered – each with the same overall thickness but different number of spokes. To account for the mass differences, the spoke shapes were modified until the structural masses of all the four designs were within 1% of each other. These designs are shown in Fig. 3.6, with the details regarding the number of spokes, stacking sequence, and subsequent deflection performance provided in Table 3.2. Note that in all cases aside from the 4-spoked configuration, the laminate stacking sequences are quasi-isotropic and aligned such that some fibers run directly parallel to the spokes. Deflection vs number of spokes are plotted against each other in Fig. 3.10. 8-spoke designs tend to give minimal deflections, and therefore, it is assumed that eight spokes will result in a mass optimal rotor structure for our loading condition. Hence, only 8-spoke designs will be considered in the proceeding study. This subsequently reduces the overall design space by 75%.

Table 3.2: Study on maximum deflection for each 4, 6, 8, 10 spoked design

Number of Spokes	Laminate Stacking Sequence	Ply Thickness (mm)	Maximum Deflection (mm)	Mass (g)
4	$[0,90]_{4,s}$	0.750	0.928	758
6	$[0,60,-60]_{4,s}$	0.500	0.898	763
8	$[0,90,45,-45]_{4,s}$	0.375	0.841	756
10	$[0,36,-72,-36,72]_{4,s}$	0.300	0.872	759

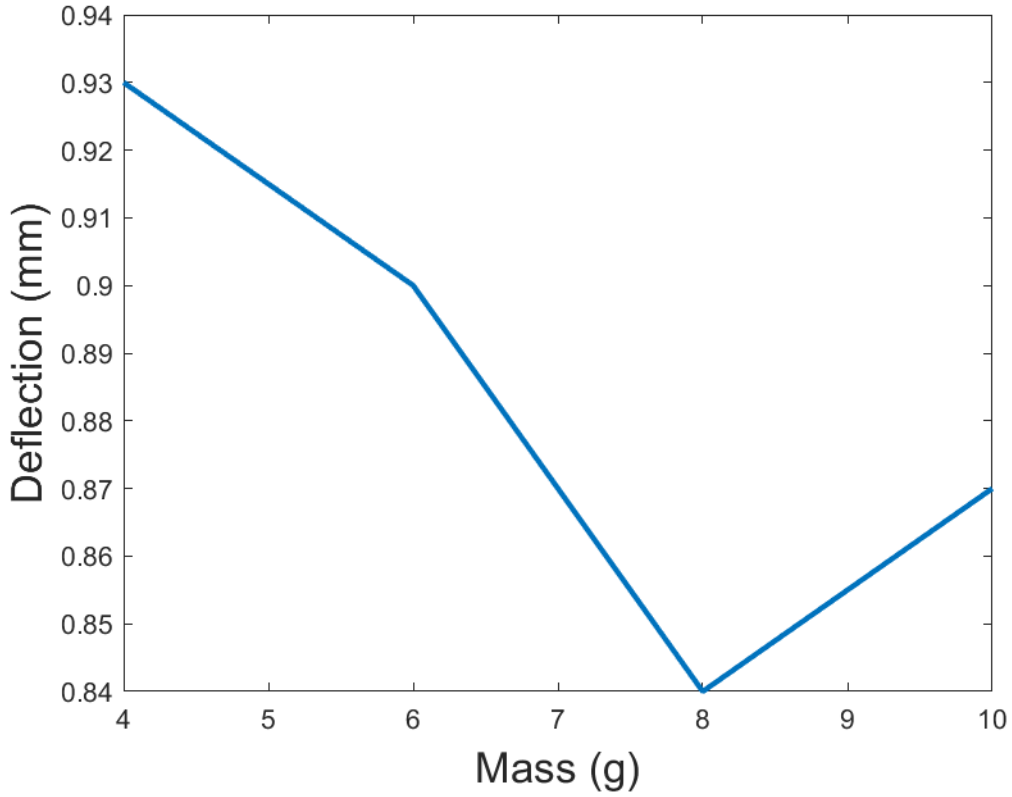

Figure 3.10: Cutout disk spoke vs max axial deflection

With the elimination of the number of spokes variable, and focusing solely on 8-spoke configurations, the Genetic Algorithm script generated Fig. 3.11. A total of 10 generations are examined, with 20 data points per generation, giving 200 total models to analyze. For a deflection constraint of 0.3 mm, an optimal mass of 941 grams is achieved, which is around 60 grams lighter than the

solid disk design previously considered. This design is given in Fig. 3.12.

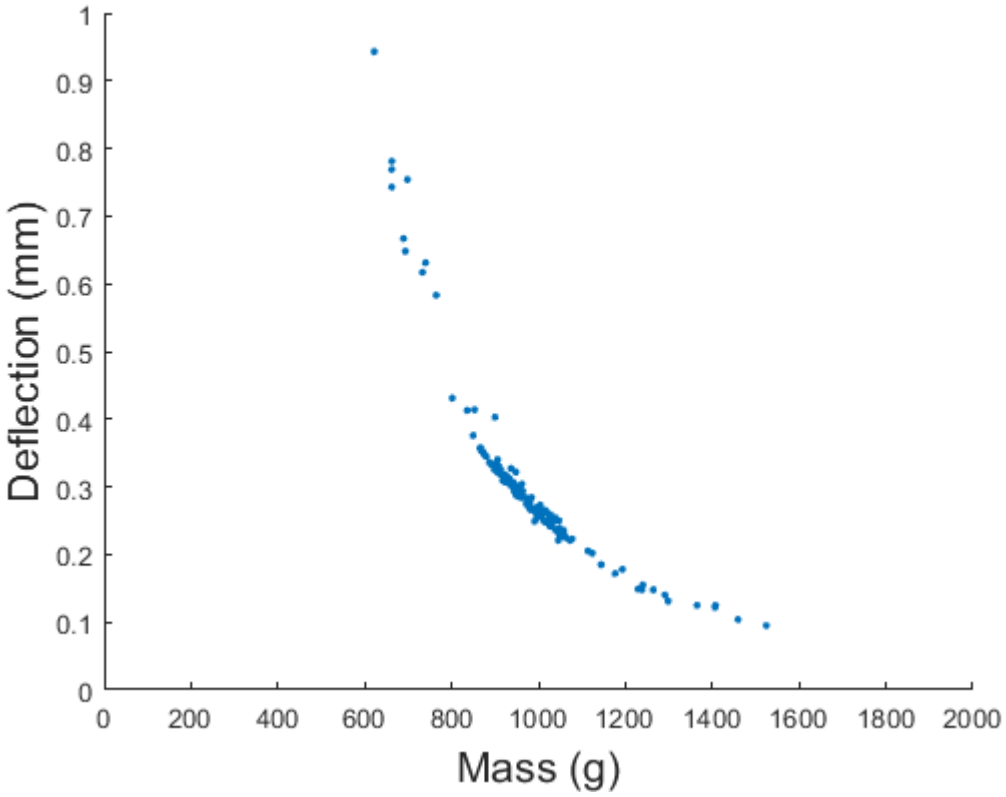

Figure 3.11: Design masses vs maximum axial deflections of cutout disk structure

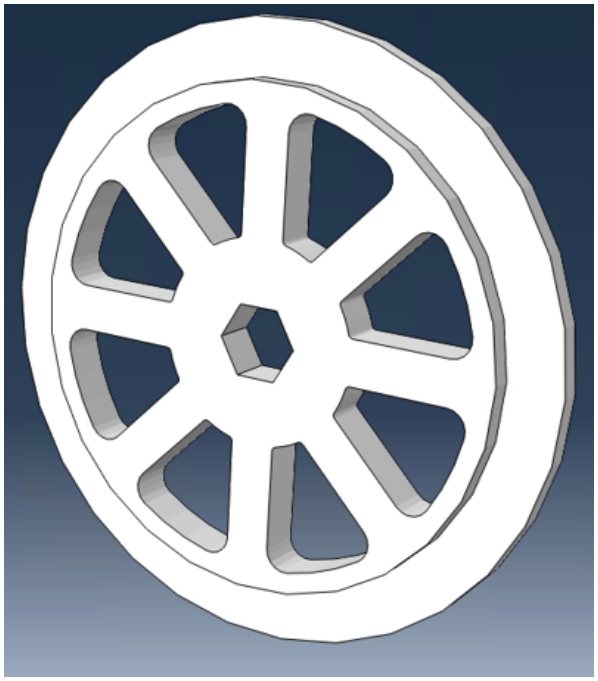

Figure 3.12: Optimal cutout disk structure

3.4 Cutout Disk with Stiffeners Configuration

This configuration is another advancement from the previous cutout disk, this time with unidirectional spokes added to the top of the structure as shown in Fig. 2.17. This configuration shares a similar design space as the previous, however, with added design variables for the inclusion of the unidirectional stiffeners. Overall, ten different design variables are to be considered. To simplify this space, the same assumption used previously that 8-spoke disks provide an optimal mass structure will be reused here. However, there are still other nine design variables to consider, with one being a discrete variation of the stiffener cross-section.

3.4.1 Cutout Disk with Stiffeners: FEA Model

The FEA model used to simulate this configuration utilizes the same quasi-isotropic 2d shell structure for the cutout rotor disk. However, this time a new component is added to the model: the stiffener. The stiffener is modeled as a 2d shell which is then "tied" to the surface of the main structure along the spoke. Figure 3.13 shows these models with the shell thickness rendered. Similarly, to the previous models, the boundary condition is fixed at the shaft, and a distributed

normal force exists around the outer circumference to simulate the axial forces at 0 RPM. An example of the FEA predicted deflections is provided in Fig. 3.14.

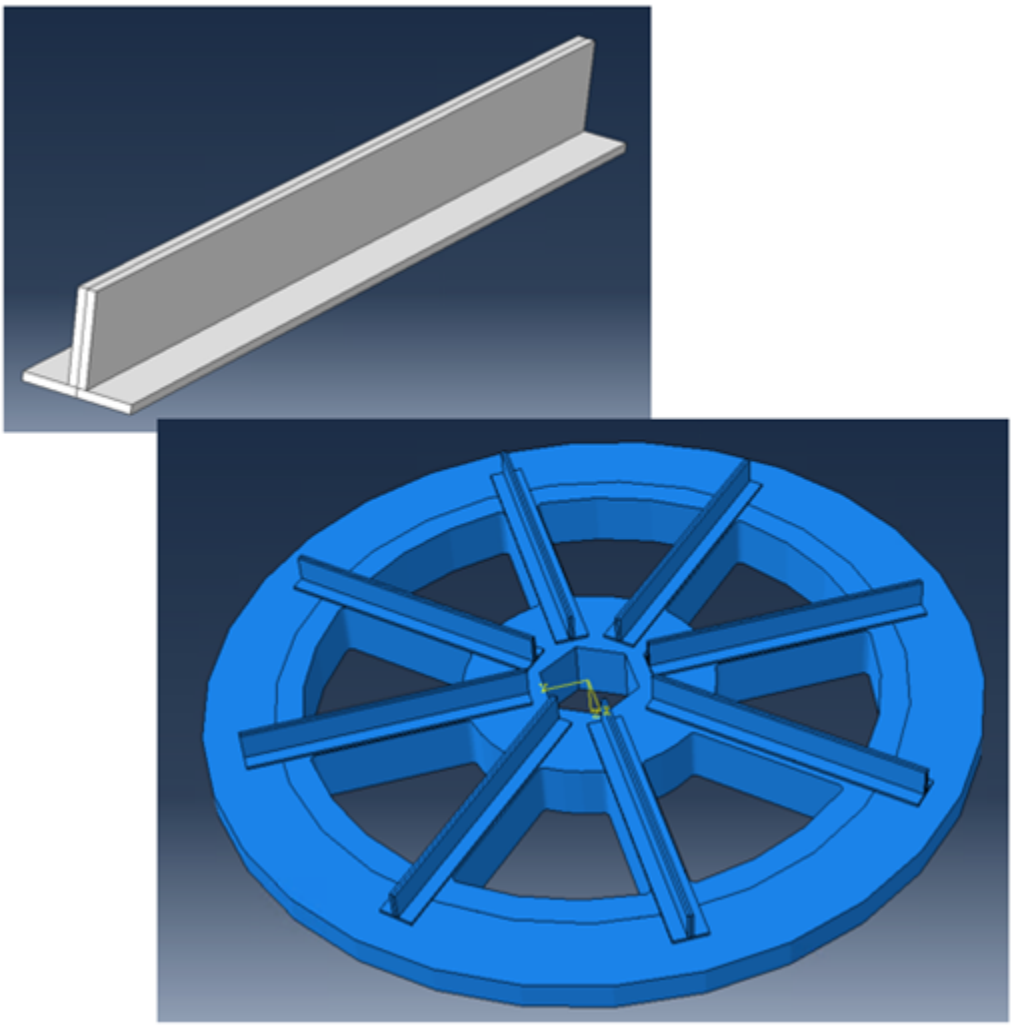

Figure 3.13: Cutout disk with stiffeners FEA model

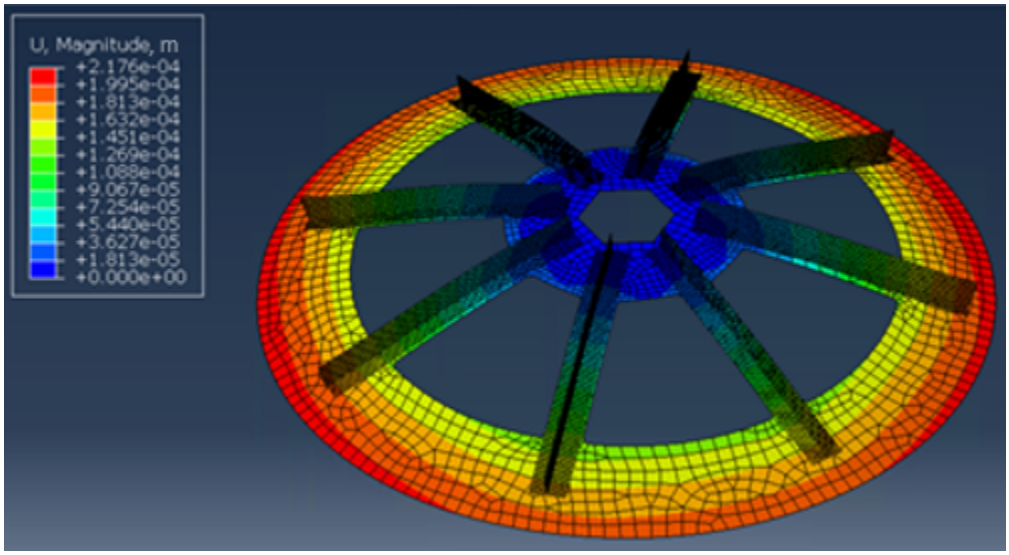

Figure 3.14: Cutout disk with stiffeners FEA model with axial deflection output

3.4.2 Cutout Disk with Stiffeners Optimization

Because there are nine design variables to consider (reduced from 10 with the assumption that 8-spoke structures give the best results), it would be wise to further constrict the design space before employing the genetic algorithm. One way to do this is to evaluate which stiffener cross-section types give the most bending inertia per unit area. Table 3.3 lists out the different stiffener types, the area of each cross-section, and corresponding bending inertia about the horizontal axis. Figure 3.15 shows diagrams of each stiffener cross-section. For a fair comparison, stiffeners of a constant maximal height of 10mm are only considered. Additionally, the other geometric parameters were modified until the cross-sectional areas fell within 1% of each other. Then, a fair basis of comparison for the bending moment of inertia can be assessed. Table 3.3 shows that I type and Box type stiffeners give the most stiffness per unit area, thus these types of stiffeners are assumed to give the best structural deflection performance, so the other cross sections were dropped out from consideration. Because both I and Box type stiffeners give equal moments of inertia, either are acceptable for analysis but it makes sense to only focus on one. The I type is chosen for further study, eliminating another design variable, and reducing the design space by 80%.

Table 3.3: Bending moments of inertia of constant area, height, and width stiffener cross sections

Stiffener Type	Area (mm^2)	I_{xx} (mm^4)
T	49.8	468
I	49.6	622
L	49.6	408
Box	49.6	622
Hat	49.6	510

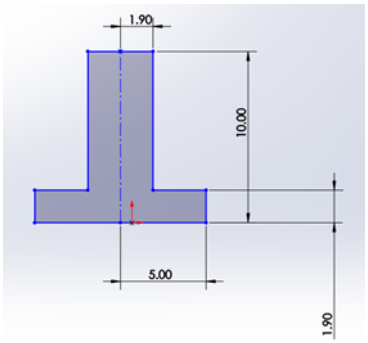

(a) T stiffener

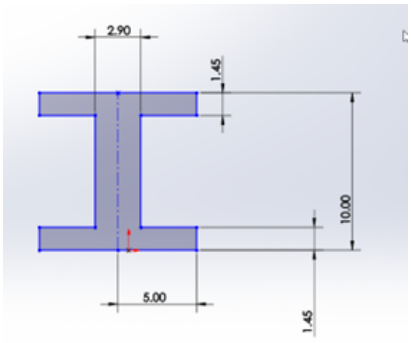

(b) I stiffener

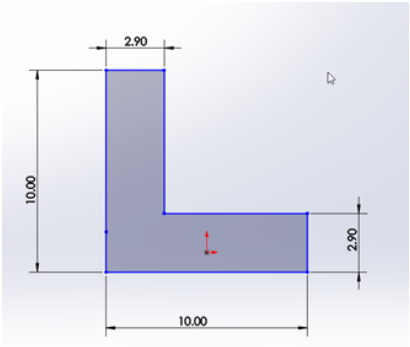

(c) L stiffener

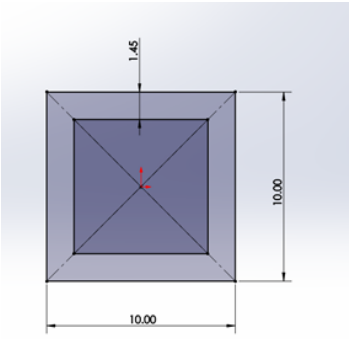

(d) Box stiffener

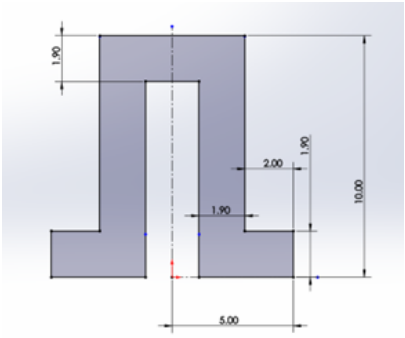

(e) Hat stiffener

Figure 3.15: Constant area and height stiffener cross sections

Additionally, results from the optimization of the cutout disk can aid in further eliminating design variables specific to the cutout disk. For example, in the optimization of the cutout disk, the variables Inner Fillet and Outer Fillet both were minimized in the mass optimal design. The intuition gained from this allows us to assume the same in the mass optimization of this configuration. Therefore, two more design variables are eliminated by setting the fillet sizes to a constant of 2mm. Finally, it was also found that mass optimal designs maximized the cutout outer radius, so this will also be held constant at 100mm. To summarize, the initial 10 design variables are now

reasonably reduced to 5 and are summarized in Table 3.4.

Table 3.4: Cutout disk with stiffeners design space version 2

Design Variable	Lower Limit	Upper Limit
Disk Overall Thickness	12 mm	18 mm
Number of Spokes	8	
Spoke Width	5 mm	25 mm
Cutout Inner Radius	35 mm	75 mm or Outer Radius
Cutout Outer Radius	100 mm	
Inner Fillet	2 mm	
Outer Fillet	2 mm	
Stiffener Cross Section Type	I (Box is equally acceptable)	
Web Height	1 mm	50 mm
Stiffener Thickness, t	1 mm	15 mm

This design space is now explored using a total of 10 generations, with 25 designs in each, giving a total of 250 models examined in Fig. 3.16. The design falling closest to both optimal mass and the deflection constraint of 0.3mm is shown in Fig. 3.17. This has an optimal mass of 849 grams, which is 150 grams lighter than the baseline solid disk design.

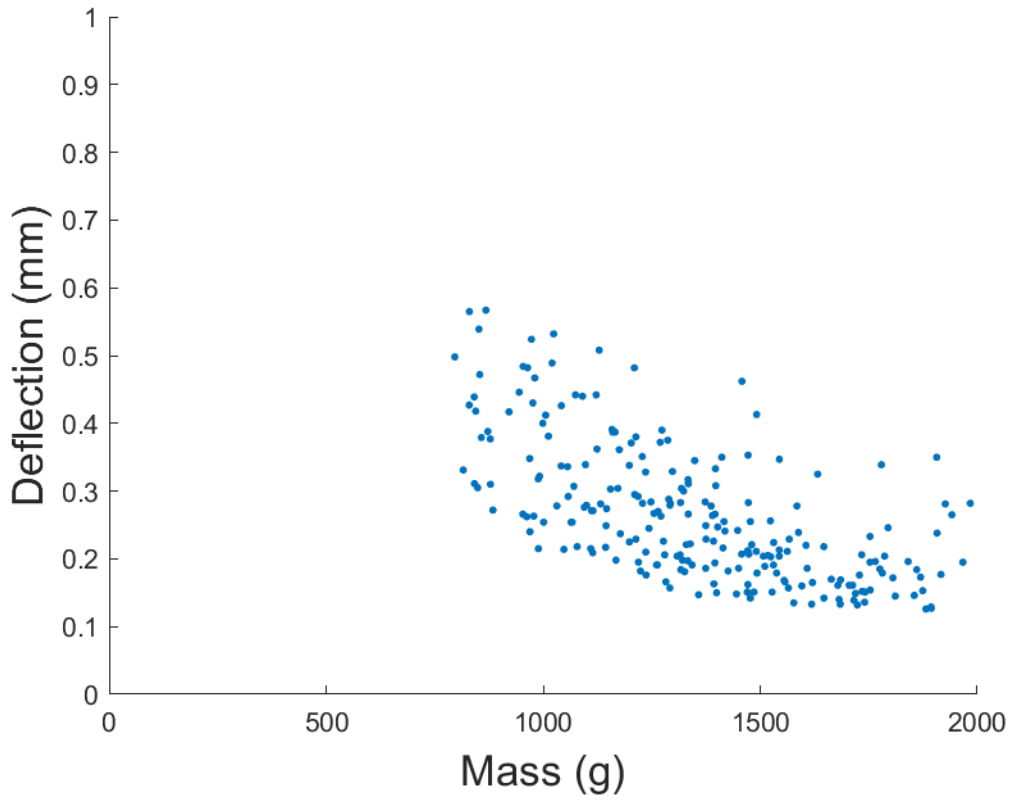

Figure 3.16: Design masses vs maximum axial deflections of cutout disk with stiffeners structure

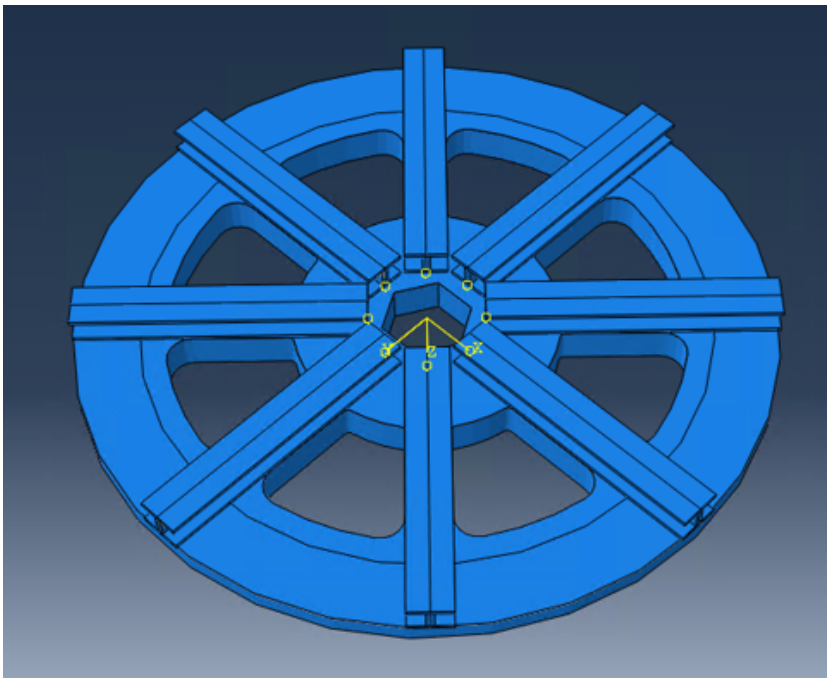

Figure 3.17: Optimal cutout disk with stiffeners structure

3.5 Unidirectional Spoke Disk Configuration

This configuration is the final major structural configuration of the present study. Again, it is a slight deviation from the previous configuration, where instead of having unidirectional stiffeners completely above a quasi-isotropic laminate, the quasi-isotropic laminate is cutout below the stiffeners between the outer diameter of the root and the inner diameter of the magnet mounting disk. In this design, the only linkages between the root and the magnet mounting disk are the unidirectional beams. Additionally, the root is no longer a single plate, but now is split in two, with one "tied" to either side of the beams. Table 2.9 provides the nine overall design variables for this configuration. Another design variable previously ignored is the retaining ring thickness. It was previously ignored due to the assumption that the retaining ring does not contribute much to the overall bending stiffness of the rotor and should have a thickness enough to handle the large centrifugal forces produced by the magnets and maintain structural integrity at 5000 RPM. It will be found later that this assumption holds true. Regardless, a minimum thickness of 2 mm is determined via both hoop stress against the 5000 RPM centrifugal loading and a minimum practical thickness for a unidirectional carbon fiber ring. As discovered in section 3.4.2, it was determined that beam cross sections of a box or I type performed the best. The same assumption applies in this case. Then, the overall number of design variables remains constant at 9. The updated design variable for this design are provided in Table 3.5.

Table 3.5: Unidirectional spoked disk design space version 2

Design Variable	Lower Limit	Upper Limit
Root Radius	40 mm	60 mm
Root Thickness	2 mm	10 mm
Beam Height	5 mm	35 mm
Beam Width	5 mm	20 mm
Beam Thickness	2 mm	5 mm
Number of Beams	6, 8, 10	
Beam Cross Section Type	I or Box	
Magnet Mounting Disk Inner Diameter	190 mm	210 mm
Magnet Mounting Disk Thickness	3 mm	12 mm
Retaining Ring Thickness	2 mm	8 mm

3.5.1 Unidirectional Spoked Disk: FEA Model

Like the previous models, the FEA model is generated in Abaqus using 2d shell elements. The boundary conditions are fixed at both shaft connection points on the root plates. Since the model is composed of multiple sub-parts (two root disks, magnet mounting disk, retaining ring, and N number of stiffeners), an assembly must be used. These are combined using "tie" interactions. The axial force is evenly distributed along the magnet mounting disk, on the magnet mount surfaces. Figure 3.18 shows an example of a 6-spoked configuration with I beams. Figure 3.19 gives an example of analysis output (deflections) from this.

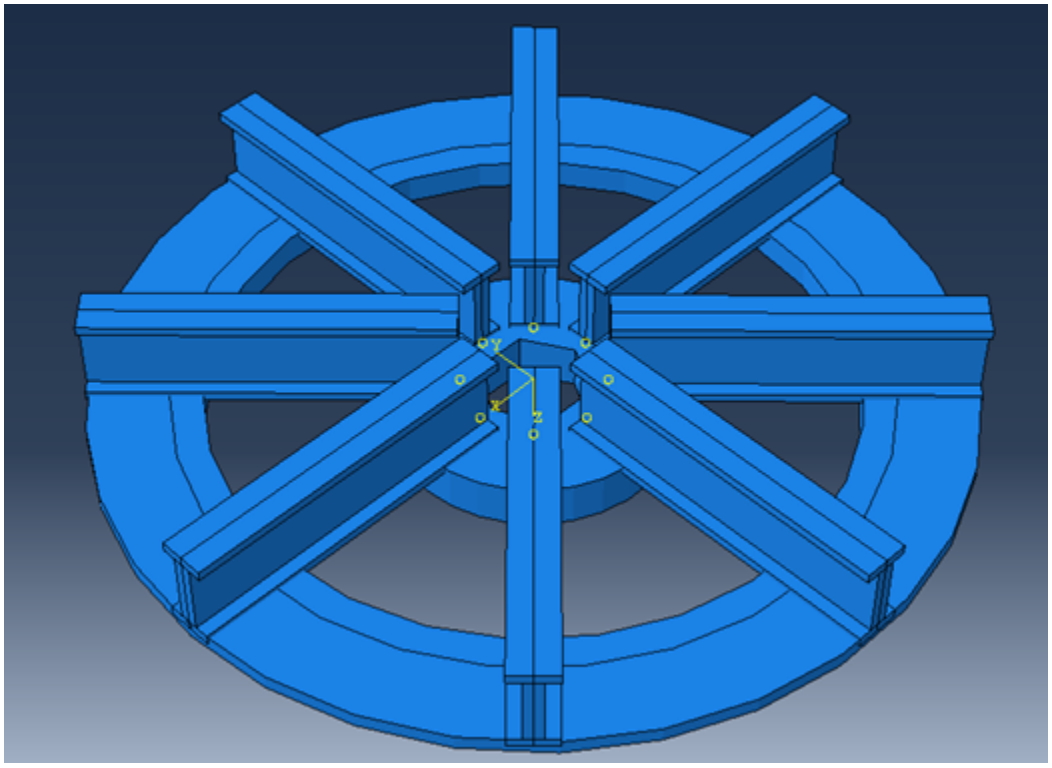

Figure 3.18: Unidirectional spoked disk FEA model

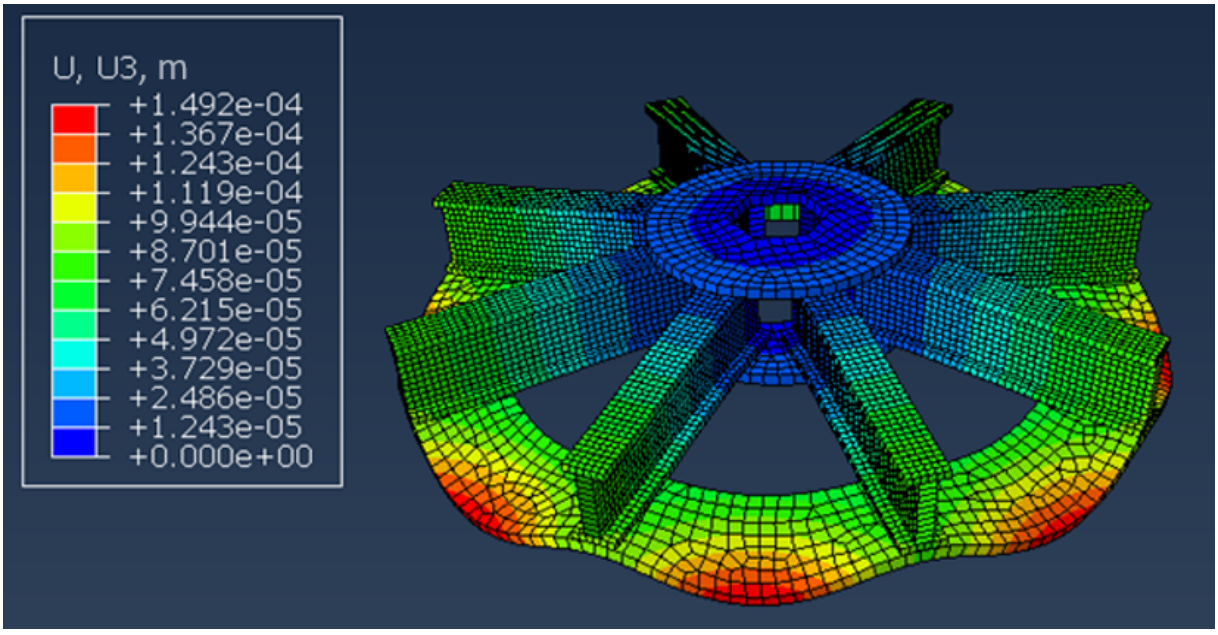

Figure 3.19: Unidirectional spoked disk FEA model with axial deflection output

3.5.2 Unidirectional Spoked Disk: Design Space Reduction

Because the design space for this configuration is extremely large, it can be very difficult for the genetic algorithm optimizer to converge to an optimal solution. It then becomes prudent to attempt to either eliminate non-important design variables or at the very least further restrict their design space. This can be accomplished by using a design of experiment study. These studies sweep the present design space and give an overarching sensitivity study of each parameter. In other words, this study reveals which of the nine design variables are most important in terms of finding a mass-optimal stiff design, and which variables are least important.

First, a Taguchi orthogonal array is used to efficiently characterize the design space. These arrays will use a certain number of factors (design variables) and evaluate them according to certain levels (typically an integer). These levels are based on the factor's range. For example, for a factor with three levels, the first level is the lower bound value, the second level is the median value between the lower and upper bound, and the third level is the upper bound value. In our case, we have nine design variables (factors) which needs to be evaluated at three levels each. [38] contains Taguchi arrays that can be used for the study. A 13-factor array at three levels is available, and since we only have nine factors we can still use this but ignore the final four columns. The array in Fig. 3.20 is used along with the design variable ranges provided in Table 3.5. Results are provided in Fig. 3.21.

X1	X2	X3	X4	X5	X6	X7	X8	X9
-	-	-	-	-	-	-	-	-
0.0	0.0	0.0	0.0	0.0	0.0	0.0	0.0	0.0
0.0	0.0	0.0	0.0	0.5	0.5	0.5	0.5	0.5
0.0	0.0	0.0	0.0	1.0	1.0	1.0	1.0	1.0
0.0	0.5	0.5	0.5	0.0	0.0	0.0	0.5	0.5
0.0	0.5	0.5	0.5	0.5	0.5	0.5	1.0	1.0
0.0	0.5	0.5	0.5	1.0	1.0	1.0	0.0	0.0
0.0	1.0	1.0	1.0	0.0	0.0	0.0	1.0	1.0
0.0	1.0	1.0	1.0	0.5	0.5	0.5	0.0	0.0
0.0	1.0	1.0	1.0	1.0	1.0	1.0	0.5	0.5
0.5	0.0	0.5	1.0	0.0	0.5	1.0	0.0	0.5
0.5	0.0	0.5	1.0	0.5	1.0	0.0	0.5	1.0
0.5	0.0	0.5	1.0	1.0	0.0	0.5	1.0	0.0
0.5	0.5	1.0	0.0	0.0	0.5	1.0	0.5	1.0
0.5	0.5	1.0	0.0	0.5	1.0	0.0	1.0	0.0
0.5	0.5	1.0	0.0	1.0	0.0	0.5	0.0	0.5
0.5	1.0	0.0	0.5	0.0	0.5	1.0	1.0	0.0
0.5	1.0	0.0	0.5	0.5	1.0	0.0	0.0	0.5
0.5	1.0	0.0	0.5	1.0	0.0	0.5	0.5	1.0
1.0	0.0	1.0	0.5	0.0	1.0	0.5	0.0	1.0
1.0	0.0	1.0	0.5	0.5	0.0	1.0	0.5	0.0
1.0	0.0	1.0	0.5	1.0	0.5	0.0	1.0	0.5
1.0	0.5	0.0	1.0	0.0	1.0	0.5	0.5	0.0
1.0	0.5	0.0	1.0	0.5	0.0	1.0	1.0	0.5
1.0	0.5	0.0	1.0	1.0	0.5	0.0	0.0	1.0
1.0	1.0	0.5	0.0	0.0	1.0	0.5	1.0	0.5
1.0	1.0	0.5	0.0	0.5	0.0	1.0	0.0	1.0
1.0	1.0	0.5	0.0	1.0	0.5	0.0	0.5	0.0

Figure 3.20: Taguchi L27 orthogonal array [38]

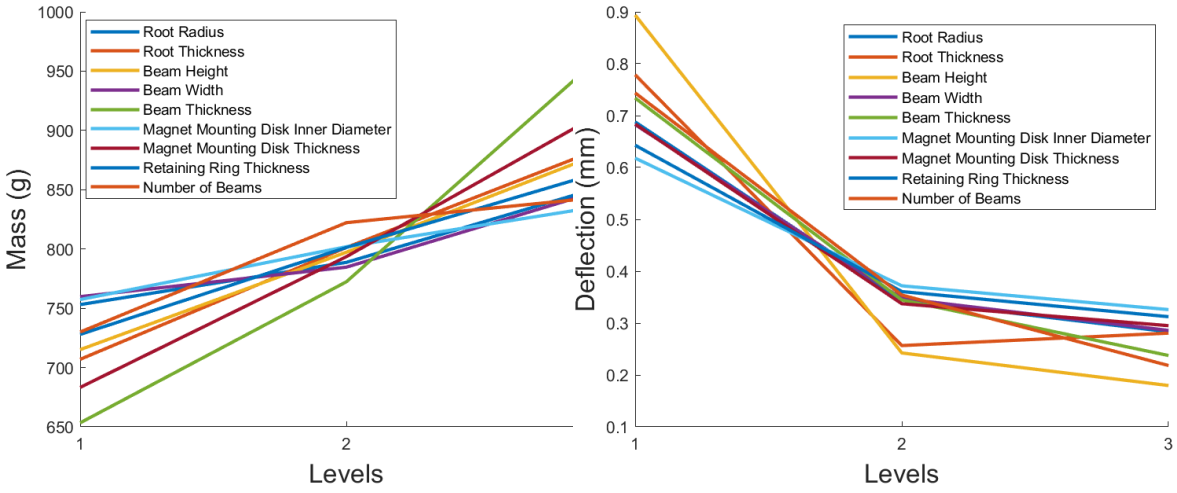

(a) Mass factor effects plot (b) Axial deflection factor effects plot

Figure 3.21: Factor effects plots for unidirectional spoked disks

When evaluating factor effects plots (sensitivity plots), the factors with the greatest effects will have the largest slopes. Alternatively, factors with the least effects will resemble a flat horizontal line. Figure 3.21a shows that the factors with the greatest effects on mass are the beam thickness and the magnet mounting disk thickness. The least effects on mass are the number of beams when between levels 2 and 3 (8 and 10 beams) and the magnet mounting disk inner length. The factors with the most effects on deflection, as given in Fig. 3.21b, are the beam height and the root thickness. Those with the least effect are the magnet mounting disk inner length and the retaining ring thickness. A step-by-step evaluation of some of the design variables of interest is now discussed, with corresponding design space changes summarized in Table 3.6.

- Beam Thickness: Because this has the highest effect on overall mass while having a moderate effect on deflection, it is prudent to slightly reduce the upper bound of this from 5 mm to 3 mm.

- Magnet Mounting Disk Thickness: This variable has the second highest effect on mass and not much influence over deflection. The upper limit is reduced from 12 mm to 6 mm.

- Number of Beams: This is the only remaining discrete variable, and eliminating one of the three options would significantly reduce the amount of work. In terms of mass, no

significant changes are observed between L2 and L3; however, there are some considerable effects between L2 and L3 for deflection. Because a clear conclusion cannot be drawn, no update will be made here.

- Root Thickness: This design variable has a moderate effect on mass, but also a sweet spot with deflection. The upper bound of root thickness can be narrowed on this sweet spot, going from 10 mm to 5 mm.

- Beam Height: This design variable has a moderate effect on mass, but the largest effect on the deflection. The lower bound will be increased from 5 mm to 15 mm if we use 6-beam designs, but for a higher number of beams, the upper bound will reduce from 35 mm to 25 mm.

- Magnet Mounting Disk Inner Length: This design variable has insignificant effects on both mass and deflection, and therefore, it can be eliminated entirely. It shall be set to 10 mm.

Table 3.6: Unidirectional spoked disk design space version 3

Design Variable	Lower Limit	Upper Limit
Root Radius	40 mm	60 mm
Root Thickness	2 mm	5 mm
Beam Height	10 mm	25 mm
Beam Width	5 mm	15 mm
Beam Thickness	2 mm	3 mm
Number of Beams	6, 8, 10	
Beam Cross Section Type	I or Box	
Magnet Mounting Disk Inner Diameter	200 mm	
Magnet Mounting Disk Thickness	3 mm	6 mm
Retaining Ring Thickness	2 mm	3 mm

Finally, to address whether or not a specific number of beams is superior to another, a short study using random sampling of the design space for the 6-beam, 8-beam, and 10-beam designs is conducted. Random sampling is done by generating designs randomly, as long as they are within the design space. In this study, 50 designs of each are sampled and deflection vs mass are plotted against each other in Fig. 3.22. Three design spaces are evaluated and tend to perform similarly to each other. Because of this, no clear superior design comes from varying the number of beams, and this remains a design variable to optimize around.

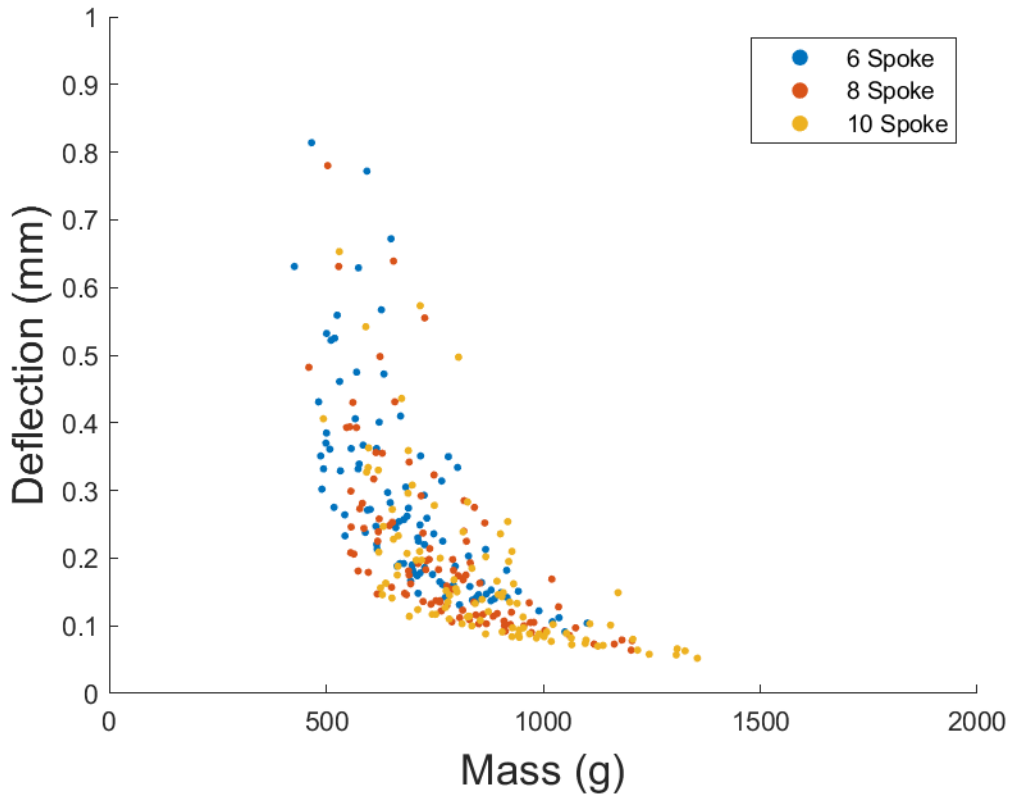

Figure 3.22: Design masses vs maximum axial deflections of cutout disk structure of unidirectional spoked beams with 6, 8, and 10 beams

3.5.3 Unidirectional Spoked Disk Optimization

With the design space narrowed, the genetic algorithm optimizer can now be employed to tackle the new design space. First, three separate optimizations were conducted with the 6-spoke, 8-spoke, and 10-spoke designs. Their design spaces are evaluated in Figs. 3.23, 3.24, and 3.25, respectively, which contain data from random sampling done in Section 3.5.2 and the

genetic algorithm optimizer. The genetic algorithm worked as intended in finding minimum mass solutions, which satisfy the 0.3 mm deflection constraint. The optimal masses for the 6-, 8-, and 10-spoke designs, respectively, are 474 g, 447 g, and 468 g. Again, technically the 8-beam design is optimal, but both the 6 and 10-beam optimal design masses fall within 6% of the best design, meaning that practically speaking these designs are nearly identical in performance – especially when considering the fact that this study was limited to the number of points computed. The rest of the thesis will focus primarily on the optimization of the 10-beam configuration unless otherwise stated otherwise.

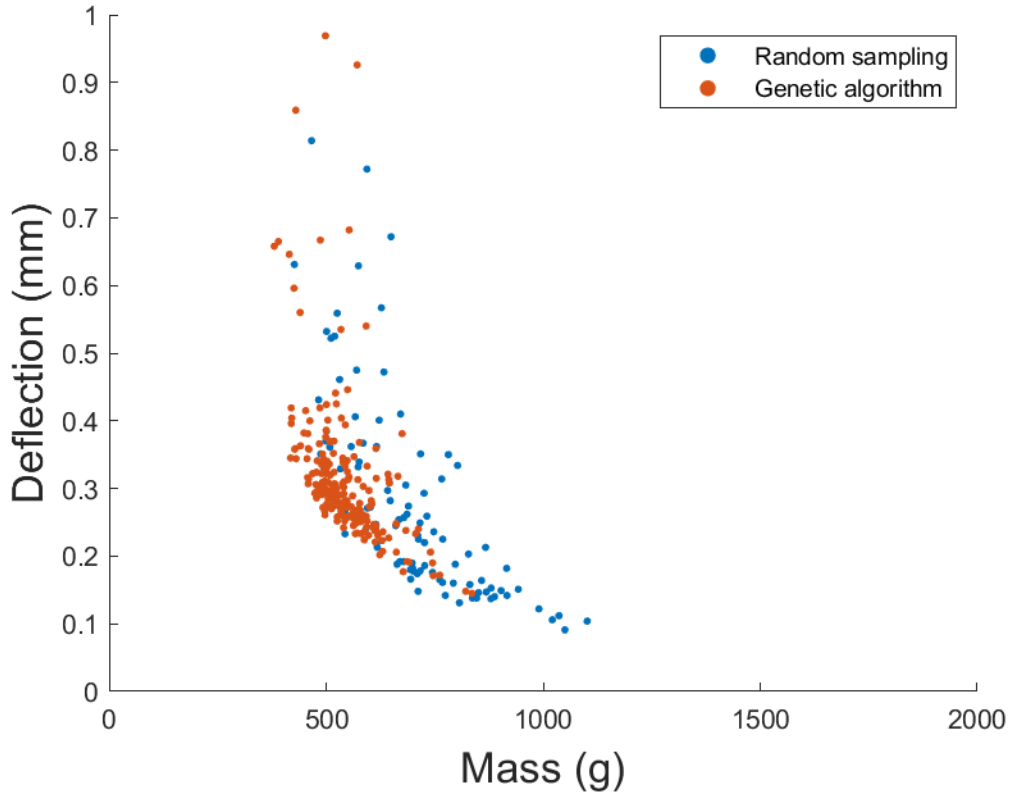

Figure 3.23: Design masses vs maximum axial deflections of unidirectional spoked beam structure with 6 beams

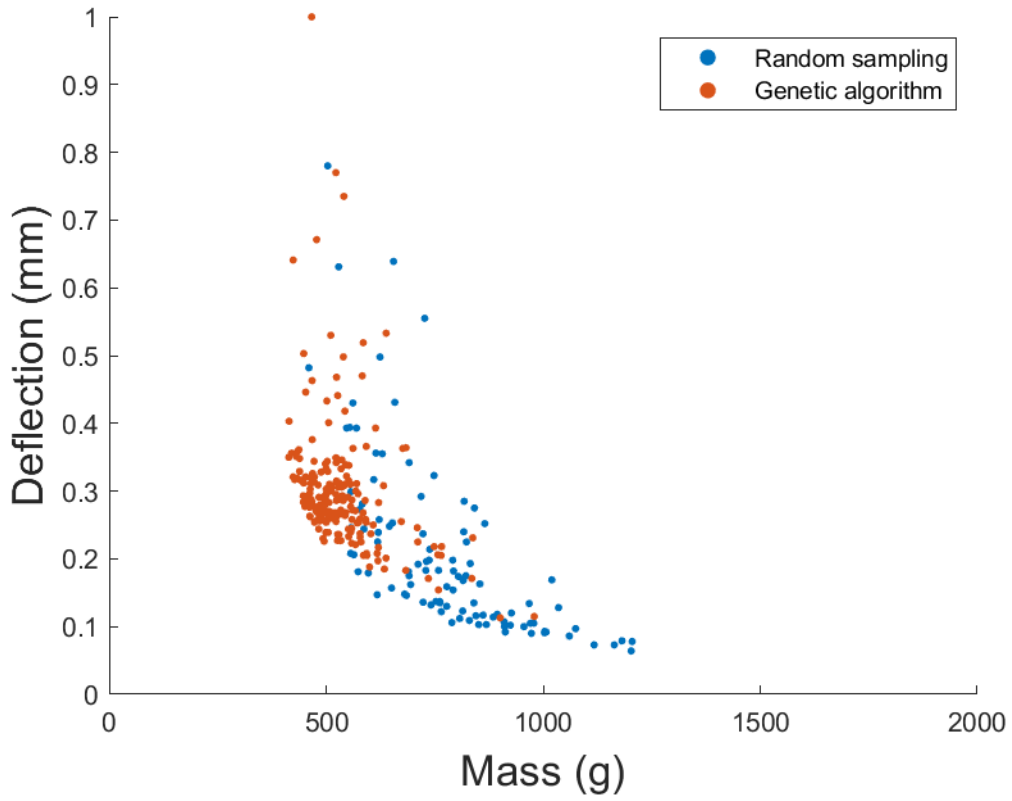

Figure 3.24: Design masses vs maximum axial deflections of unidirectional spoked beam structure with 8 beams

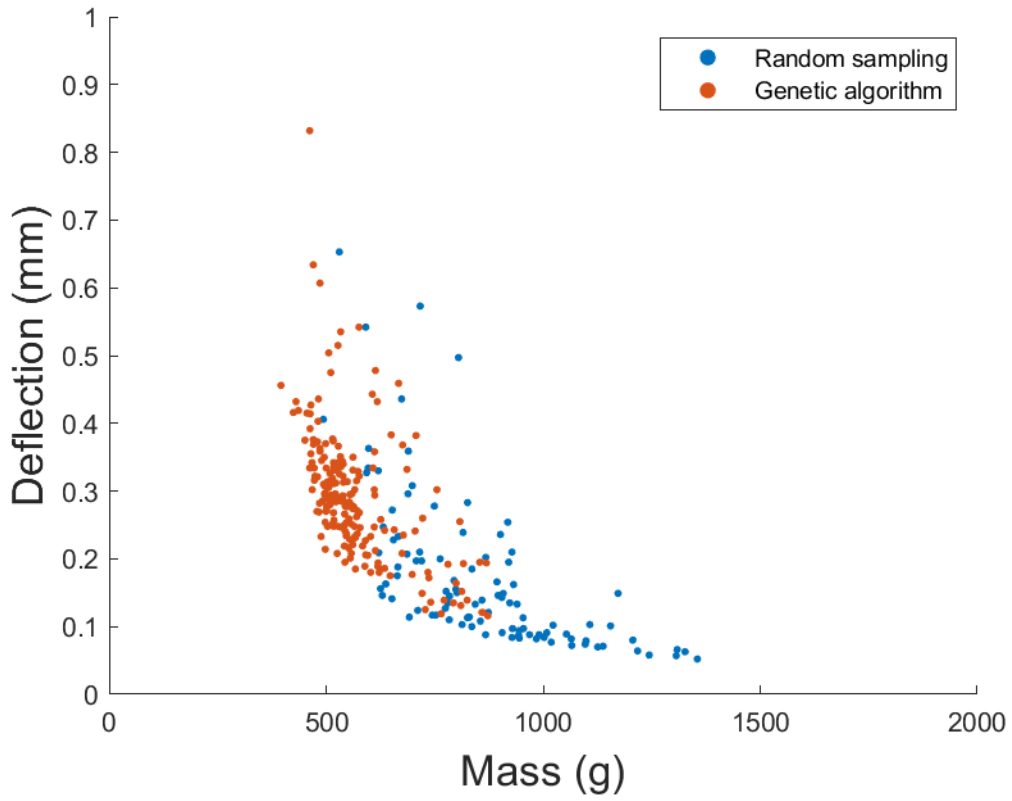

Figure 3.25: Design masses vs maximum axial deflections of unidirectional spoked beam structure with 10 beams

With the design space further narrowed to 7 design variables, the final composite structure optimization is conducted as follows. Optimization runs consisted of 100 data points per generation and 20 generations in total. Each FEA model took approximately 1.5 minutes to solve, and therefore, this study required about 50 hours to run. Regardless, Fig. 3.26 contains the evaluated design space resulting from this study. The resulting optimal structural mass is 406 grams for 0.296 mm of deflection, and the design is given in Fig. 3.27. Note that this design only weighs 40% of the baseline optimal solid disk design. Table 3.7 provides the final values of the design variables in this optimal design.

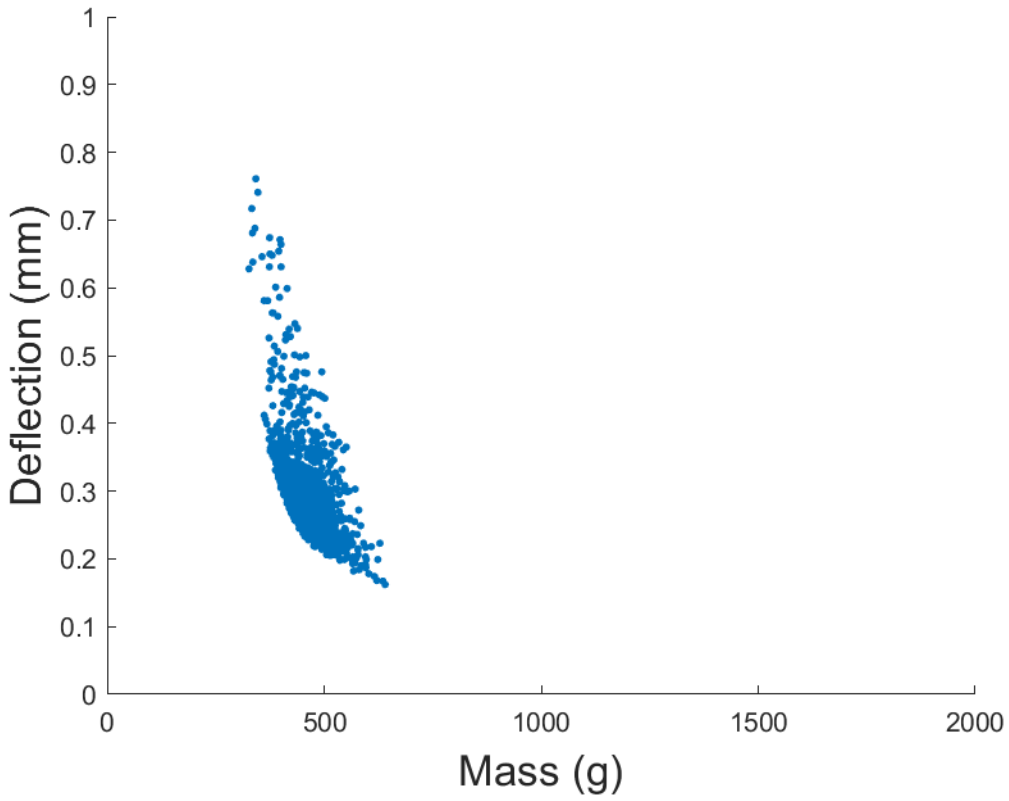

Figure 3.26: Design masses vs maximum axial deflections of unidirectional spoked disk structure

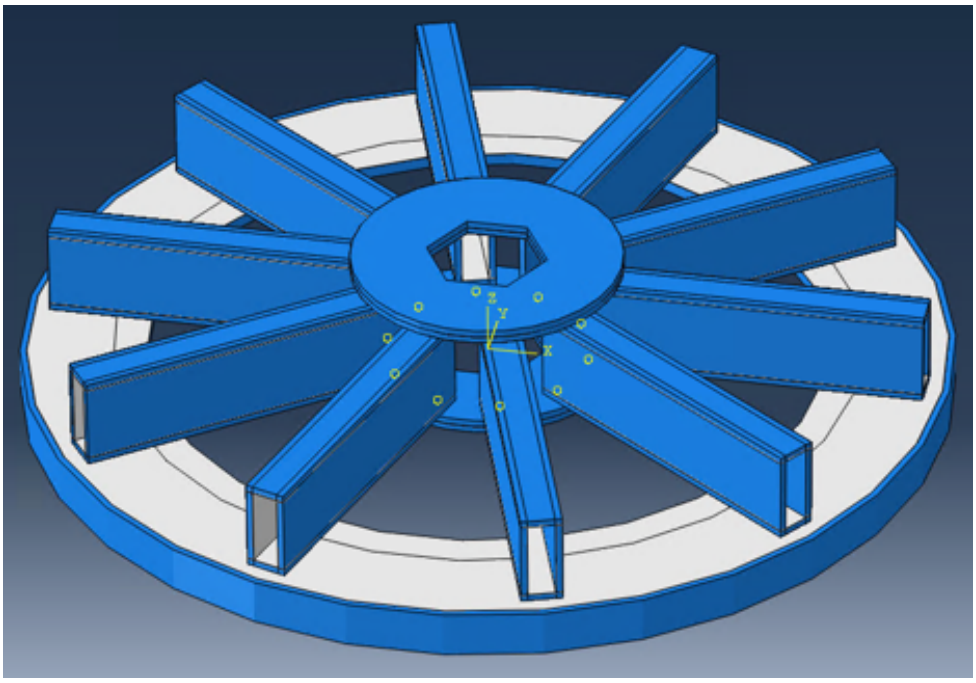

Figure 3.27: Optimal unidirectional spoked disk structure

Table 3.7: Unidirectional spoked disk optimal design variables

Design Variable	Optimal Value
Root Radius	40.0 mm
Root Thickness	4.05 mm
Beam Height	23.5 mm
Beam Width	8.03 mm
Beam Thickness	2 mm
Number of Beams	10
Beam Cross Section Type	Box
Magnet Mounting Disk Inner Diameter	200 mm
Magnet Mounting Disk Thickness	3.81 mm
Retaining Ring Thickness	2.07 mm

3.6 Metallic Structure Optimization

It is also important to compare the optimal carbon fiber rotor structure with a metalic structure to fully understand the performance gains of using composite load bearing stuctures for electric motors. Towards this, three different metalic rotor structures using Aluminum and Titanium alloys were analyzed. Table 1.2 provides the mechanical properties of specific Aluminum and Titanium alloys compared against the IM7/8552 composite used throughout this study. Aluminum 2024-T3 has been widely used in the aerospace industry as a strong, lightweight structural material for many decades. Additionally, Titanium Ti-6Al-4V (90% Titanium, with 6% Aluminum and 4% Vanadium) is also commonly used for aerospace applications. While other Aluminum or Titanium alloys will certainly benefit more in particular applications, using these alloys to characterize the material classes is suitable for this current study. The Young's modulus is provided in Table 1.2 along with the failure strength. These values are conservatively obtained from the Metallic Materials Properties Development and Standardization (MMPDS) [16] and converted to metric units. These materials are assumed to be isotropic. For a fair comparison with the composite

structure, the design space is very similar to that used in the composite rotor structure. However, because of the large difference between the classes of materials, a new and broader design space is provided in Table 3.8. Note that the retaining ring minimum thickness was driven by a minimum 2mm laminate in the composite case. In this case, hoop stress is used with the centrifugal loading to minimally size each retaining ring based on the material strength. With a given design rotational speed of 5000 RPM, the corresponding magnet masses of 1443 grams per rotor, and conservatively using the radial distance from the center of rotation to the furthest point of the magnets at 135 mm, an estimate of the total centrifugal force experienced is 53.5 kN. By dividing this value by the outer circumference, the edge loading is 63 kN/m. If this loading is treated as applying internal pressure to a thin ring, then the hoop stress can be found and used to help determine the minimum thickness necessary for the retaining ring. The pressure is found by distributing the edge load across the height of the magnets, in this case, 10 mm, which computes a pressure of 6.3 MPa. Given that a failure of the retaining ring will result in the catastrophic destruction of the motor, a large safety factor was applied to the material strengths given in Table 1.2 and are identified in Table 3.9. A safety factor of 3 was applied to both Aluminum and Titanium's yield strength, while 4 was applied to every material's ultimate strength (including the unidirectional composite). The lower strength found is the one used as the design strength for sizing the minimum retaining ring thickness.

Table 3.8: Metallic spoked disk design space

Design Variable	Lower Limit	Upper Limit
Root Radius	40 mm	60 mm
Root Thickness	1 mm	5 mm
Beam Height	10 mm	30 mm
Beam Width	5 mm	15 mm
Beam Thickness	1 mm	3 mm
Number of Beams	10	
Beam Cross Section Type	Box	
Magnet Mounting Disk Inner Diameter	200 mm	
Magnet Mounting Disk Thickness	2 mm	8 mm
Retaining Ring Thickness	Minimum Computed	Minimum Computed + 3 mm

Table 3.9: Minimum retaining ring thicknesses

Material	Strength Safety Factor	Design Strength (MPa)	Minimum Thickness (mm)
Al 2024-T3	3	75	11.3
Ti-6Al-4V	4	195	4.36
IM7/8552	4	582	1.46

The genetic algorithm is employed with the design variables given in Table 3.8. Similar to the composite structure optimization, 100 data points are generated with each generation with a total of 20 generations evaluated. Figure 3.28 contains the results from the Aluminum rotor study, and Fig. 3.29 contains that of the Titanium study. Optimal masses and deflections are 831 g with 0.299 mm bending deflection for the Aluminum design, and 819 g with 0.286 mm deflection for the Titanium design. Identified optimal design variables are provided in Table 3.10.

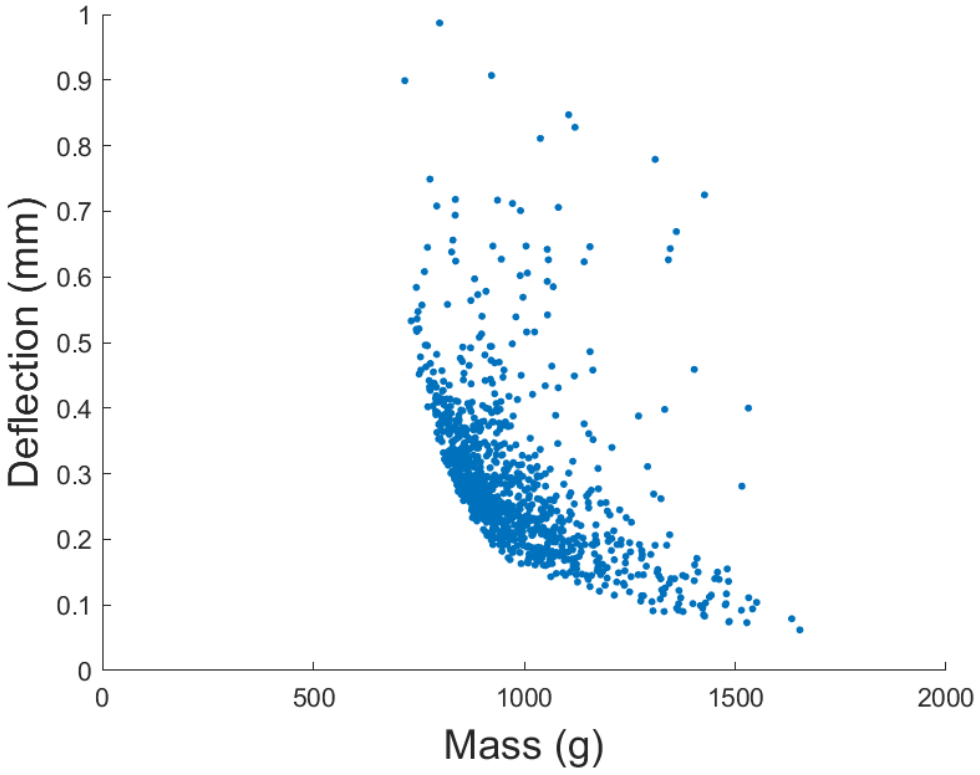

Figure 3.28: Design masses vs maximum axial deflections of aluminum spoked disk structure

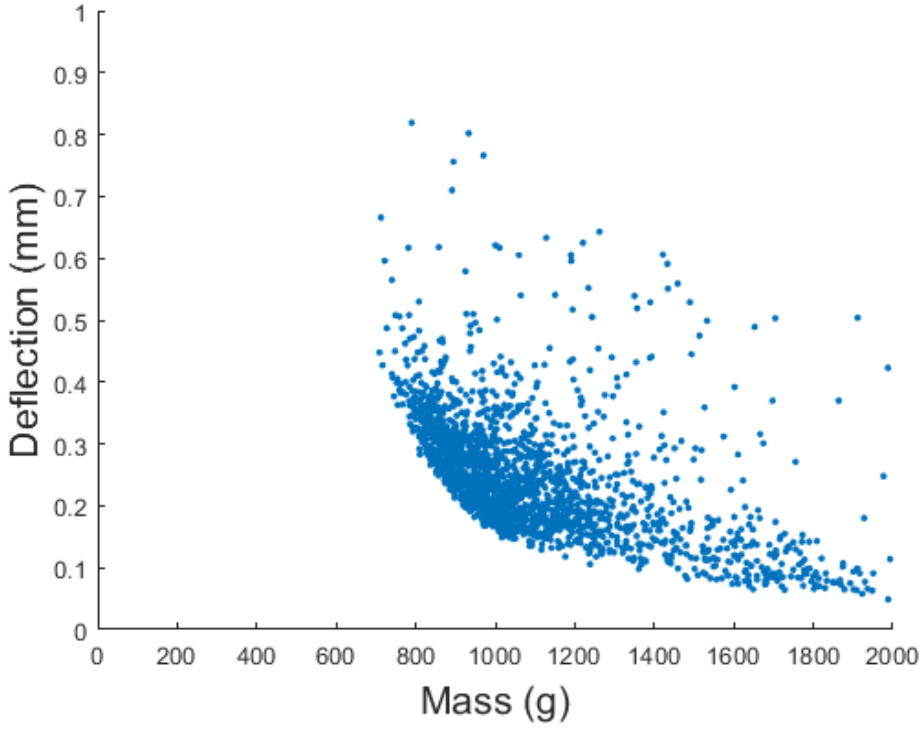

Figure 3.29: Design masses vs maximum axial deflections of titanium spoked disk structure

Finally, a hybrid Aluminum structural design with a carbon fiber composite retaining ring is optimized. This is simply the same study performed with the aluminum, except the unidirectional IM7/8552 retaining ring (with a 2mm minimum thickness) is used. Figure 3.30 shows the results from this, with an optimal design giving 600 g of mass and 0.283 mm of deflection. The identified optimal design variables are also given in Table 3.10.

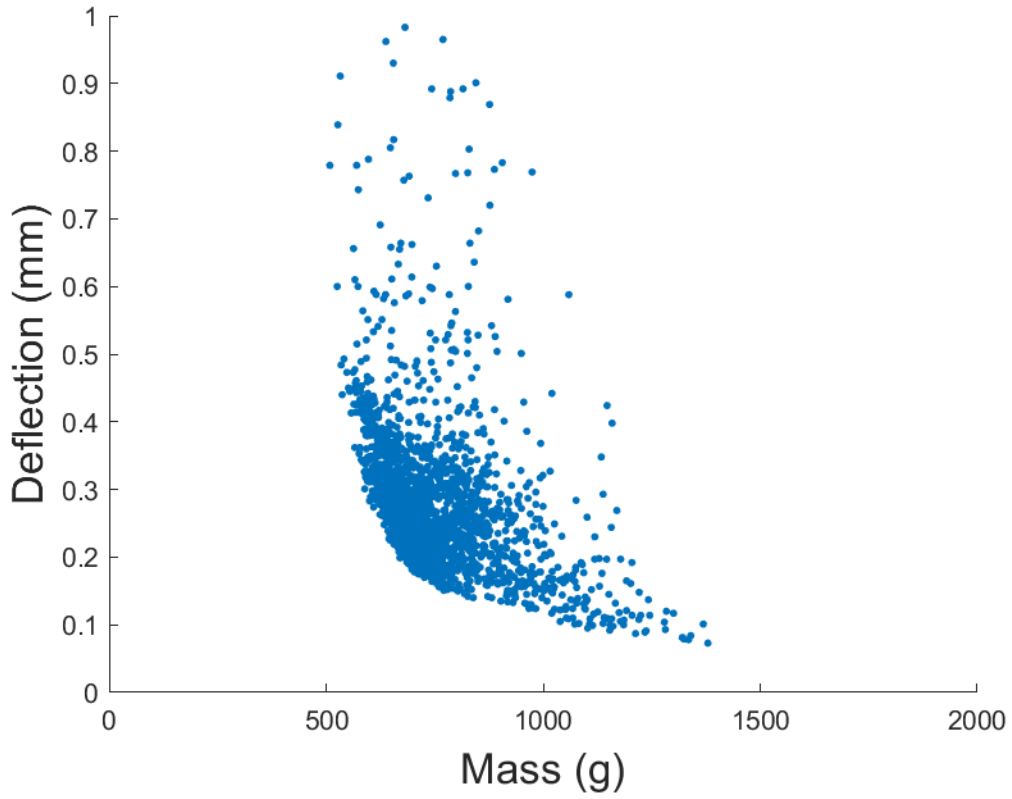

Figure 3.30: Design masses vs maximum axial deflections of hybrid spoked disk structure

Table 3.10: Optimal design variables for metallic spoked disk variations

Design Variable	Aluminum	Titanium	Hybrid
Root Radius	41.4 mm	40.0 mm	42.2 mm
Root Thickness	3.53 mm	2.10 mm	3.29 mm
Beam Height	26.7 mm	30.0 mm	24.0 mm
Beam Width	5.00 mm	5.40 mm	9.37 mm
Beam Thickness	1.50 mm	2.00 mm	1.50 mm
Number of Beams	10	10	10
Beam Cross Section Type	Box	Box	Box
Magnet Mounting Disk Inner Diameter	200 mm	200 mm	200 mm
Magnet Mounting Disk Thickness	2.54 mm	2.77 mm	3.30 mm
Retaining Ring Thickness	11.5 mm	4.38 mm	2.00 mm

3.7 Comparisons and Discussion

All of the optimization studies have been performed, and are now compared and contrasted with each other.

First, the four different optimal IM7/8552 structural configurations are compared. Table 3.11 gives the optimally found mass of the structures which satisfy the 0.3 mm constraint. Figure 3.31 compares the design space of these configurations on the same plot. It can be seen that by taking advantage of composite anisotropy, the Unidirectional Spoked Disk greatly outperforms the other configurations where each consist of a quasi-isotropic layup along the beam length. The Unidirectional Spoked Disk thus makes more efficient use of carbon fiber composites.

Table 3.11: Optimal mass of the composite structural configurations

Composite Structural Configuration	Optimal Mass (g)
Solid Disk	1000
Cutout Disk	941
Cutout Disk with Stiffeners	849
Unidirectional Spoked Disk	406

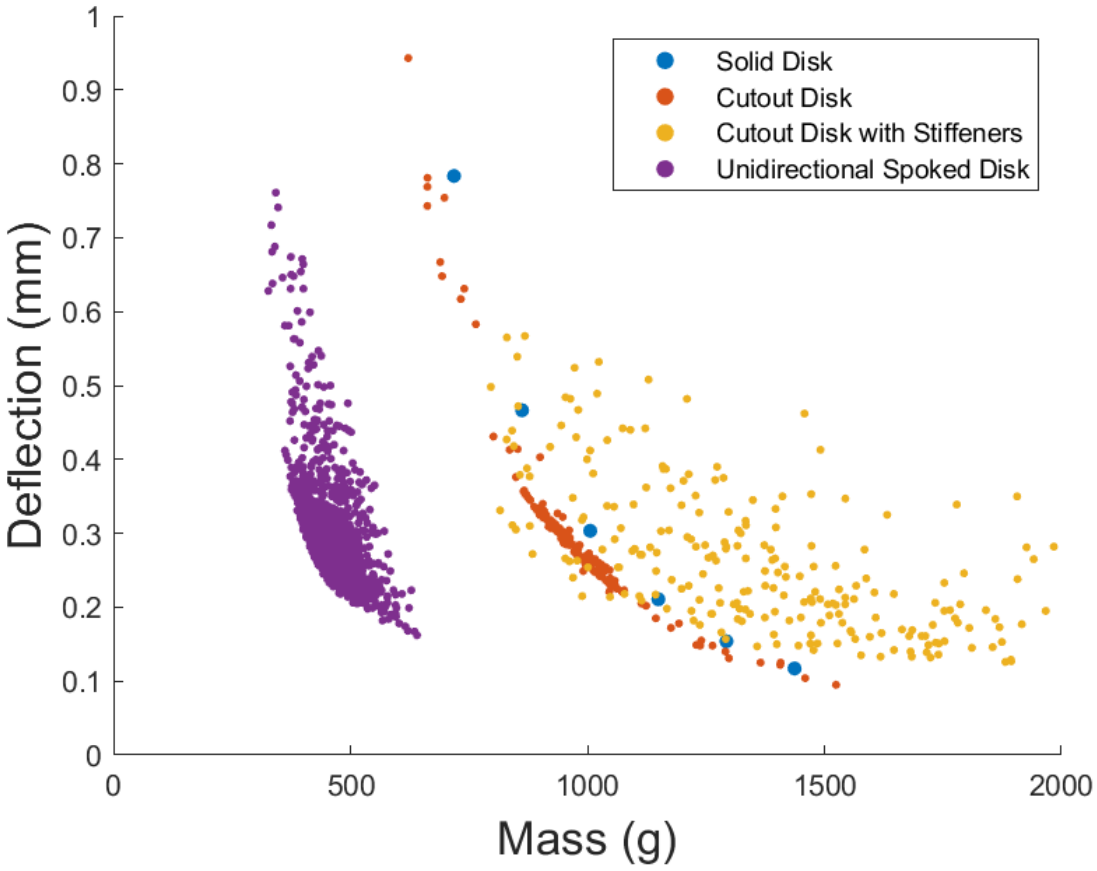

Figure 3.31: Design masses vs maximum axial deflections of IM7/8552 configurations

Since the Unidirectional Spoked Disk is the superior structural geometry, optimization studies using this configuration were conducted using metallic materials in Section 3.6. This generated a unique scatter plot for each material, and they are overlaid in Fig. 3.32. Table 3.12 picks out the optimal design from each class that satisfies the 0.3 mm deflection constraint.

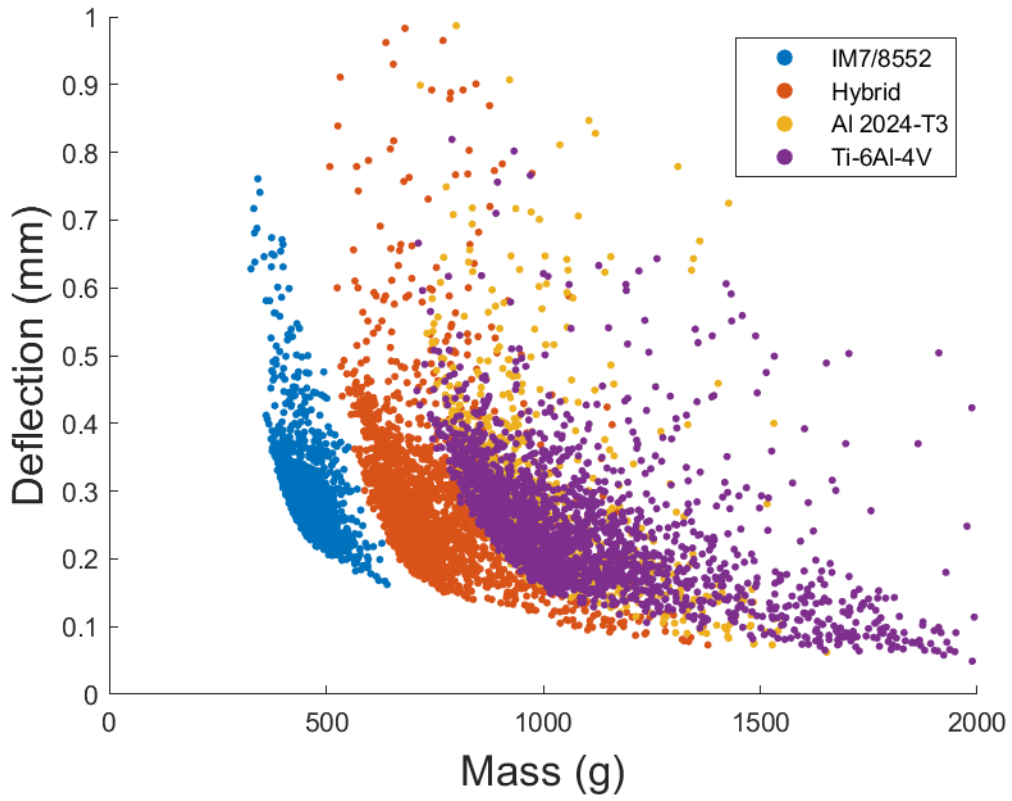

Figure 3.32: Design masses vs maximum axial deflections of unidirectional spoked disk models by material

Table 3.12: Optimal mass of the unidirectional spoked disk configurations by material

Material	Optimal Mass (g)
IM7/8552	406
Hybrid	600
Al 2024-T3	831
Ti-6Al-4V	819

Consider the results given in Table 3.11 against that in Table 3.12. Table 3.11 demonstrates that the optimal structural configuration is that of the Unidirectional Spoked Disk, especially since it allows the leverage of carbon fiber composite's strong anisotropic stiffness. However, notice that when the anisotropic stiffness is not taken advantage of, the quasi-isotropic layup configurations are actually worse in optimal mass than competing metallic designs! For example, Table 3.11 gives

the Solid Disk, Cutout Disk, and Cutout Disk with Stiffeners Configurations, with optimal masses ranging between 849 to 1000 g. However, the entirely Aluminum and Titanium structures given in Table 3.12 yield optimal masses of 831 and 819 g respectively. Hence, it is critical in a mass efficient composite design to utilize unidirectional layups efficiently.

4. TECHNOLOGY DEMONSTRATOR PROTOTYPE

In Section 3, many competing structural configurations were compared against one another using a single-objective genetic algorithm optimization process to find mass optimal structures meeting a 0.3 mm deflection constraint. As shown in Table 3.11, the Unidirectional Spoked Disk configuration outperformed the other configurations by a large margin. Hence, it is recommended that a real prototype of this structure be pursued as opposed to the other types of structures. Section 4.1 will introduce the methodology used in taking the type of optimized structure given in Fig. 3.18 through a redesign in order to make it feasible to manufacture. Section 4.2 will include testing methodology and results from simulating the axial attraction forces acting on the structure and the corresponding deflections measured.

4.1 Prototype Rotor

This section introduces the process behind the design and fabrication of the first rotor prototype. As will be seen in the following sub-section, considerable effort goes into designing the unidirectional spoked disk in such a way that it is manufacturing friendly. Then, the assembly of the rotor structure and mock magnets are presented in detail.

4.1.1 Manufacturing driven design

The design shown in Fig 4.1 had all parameters based on the optimized geometry given as the best unidirectional spoked configuration in Section 3. The only difference is that while the analytical model used box shaped stiffener cross sections, this one used hat shaped ones with an equivalent bending moment of inertia. This was done in an effort to assist in the fabrication of the spoke sections using a mold. The basic idea behind the fabrication of this design was to individually create each part using a vacuum-bagging method, then to assemble them together using some methods such as structural adhesives, bolted joints, or other potential engineering solutions. Regardless, an estimate received on the cost of producing this configuration of structure was over $90,000 per unit. This is due to the sheer number of toolings required, the labor involved

in producing each component, and the engineering work required to make each component feasibly assemble together. While this structure is true to the analytical model, it is likely to never be made due to it's impractical design.

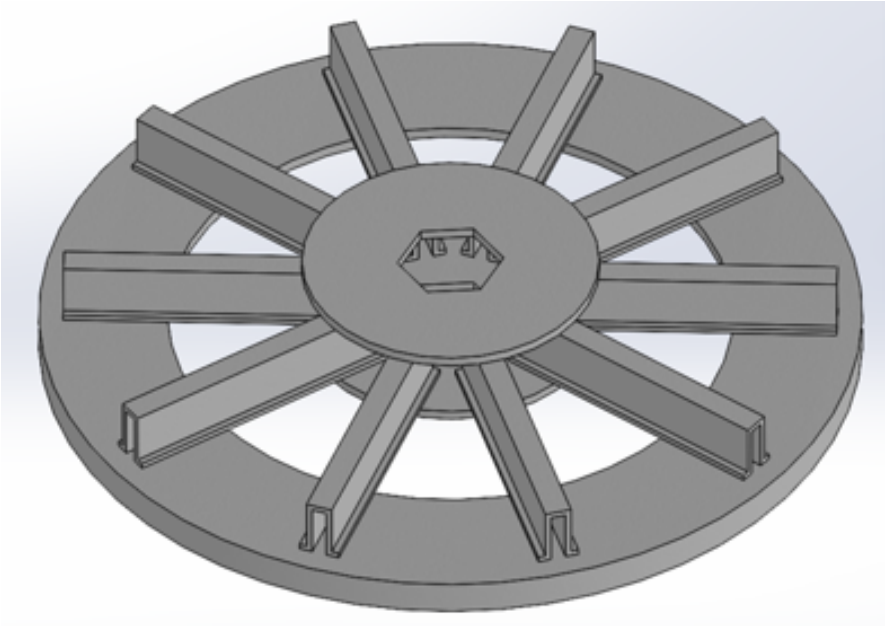

Figure 4.1: 10 spoked design based closely on analytical model

Koenigsegg [39] is a company that produces high-performance cars. Their cars use hollow core carbon fiber wheels, with an example shown in Fig. 4.2. Note that their design has structural elements that are similar to that in our rotor structure: the root hub, the spokes, and an outer ring which could be modified for holding the permanent magnets. One of the key advantages this design has over the previous design is that the entire structure is composed of only one monolithic structure such that the carbon fiber layups smoothly flow into each section. This is made possible with their Aircore patented technology which allows for a single-piece hollow core structure [40]. Using this design as inspiration, the rotor structure given in Fig. 4.1 can be re-engineered to be produced more economically while maintaining similar structural weight and performance.

Figure 4.2: Koenigsegg hollow core carbon fiber wheel [41]

With the Koenigsegg wheel design guiding the next design iteration, Fig. 4.3 highlights the next step of the carbon fiber rotor design. This model is composed of 2 main pieces: a standalone carbon fiber retaining ring, and a carbon fiber rotor structure with a foam core. While ideally a single-piece hollow carbon fiber rotor structure would be used, for practical manufacturing purposes, the foam core exists to provide the composite prepreg laminae a surface to be laid on. It should be noted that Koenigsegg was able to address this problem with their patented Aircore technology and produce single hollow core composite structures [40], hence, it is possible to create the rotor structure as a single piece with a hollow core. However, for the present application, a foam core is sufficient for the design. The addition of the foam core also gives the entire structure the type of stiffness benefits similar to that of sandwich panels.

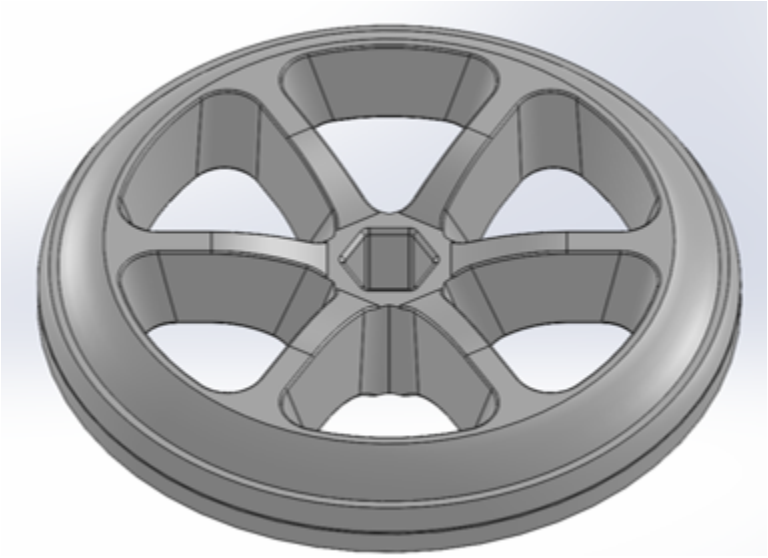

Figure 4.3: Foam compression rotor model

There are also several other factors that helped contribute to making the overall design more manufacturing friendly. One key point is to reduce the number of overall beams. Section 3.5.3 contained a study of the difference in optimal mass between 6, 8, and 10 spoked configurations of the rotor structure. It was found that optimal masses varied less than 6% between these configurations. Hence, moving from a 10-spoked structure to a 6-spoked structure should not result in a drastically different weight and should be an acceptable substitute. Figure 4.4 also highlights some key design features which help reduce overall cost of production. Fillets are necessary in the inside of the cutouts to promote the smooth transition of fiber direction. Additionally, rounded edges must exist everywhere on the model to reduce stress concentrations and avoid crimping the laminas. Finally, a 5 to 10 degree draft angle must be introduced on molded surfaces to allow for ease in removal from the tooling. Production of this design is estimated to cost only $14,000, which is a dramatic difference from the previous quote.

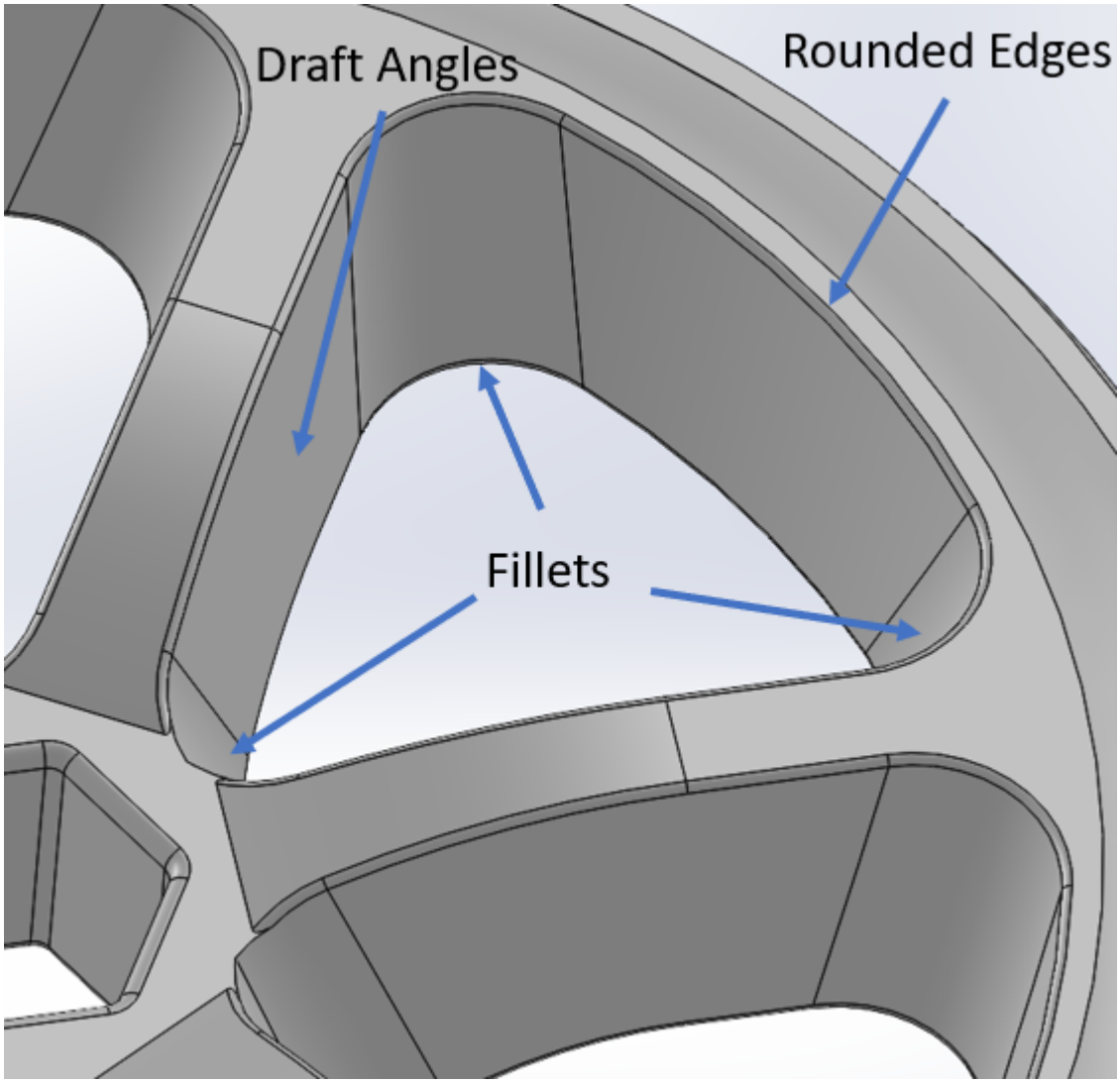

Figure 4.4: Features in a manufacturing friendly design

Finally, another effort was made to further reduce the overall cost of producing a rotor structure. Fig. 4.5 gives an isometric view of the hollow laminate rotor. This design differs from the former because it is a hollow core design, but made out of two main pieces as shown in the exploded view in Fig. 4.6. This design is based on having two pieces that can be made using a mold and a vacuum bagging process. These can be assembled together by simply using structural adhesive along several interfacing surfaces, with more details on this in the upcoming section. Since the number of overall tooling is again reduced, and there is no longer a foam piece to manufacture, the cost of production is reduced again to $8,000. A real-life version of this rotor was manufactured,

and is shown in Fig. 4.7 and in Fig. 4.8 with unbonded stainless steel mock magnets included.

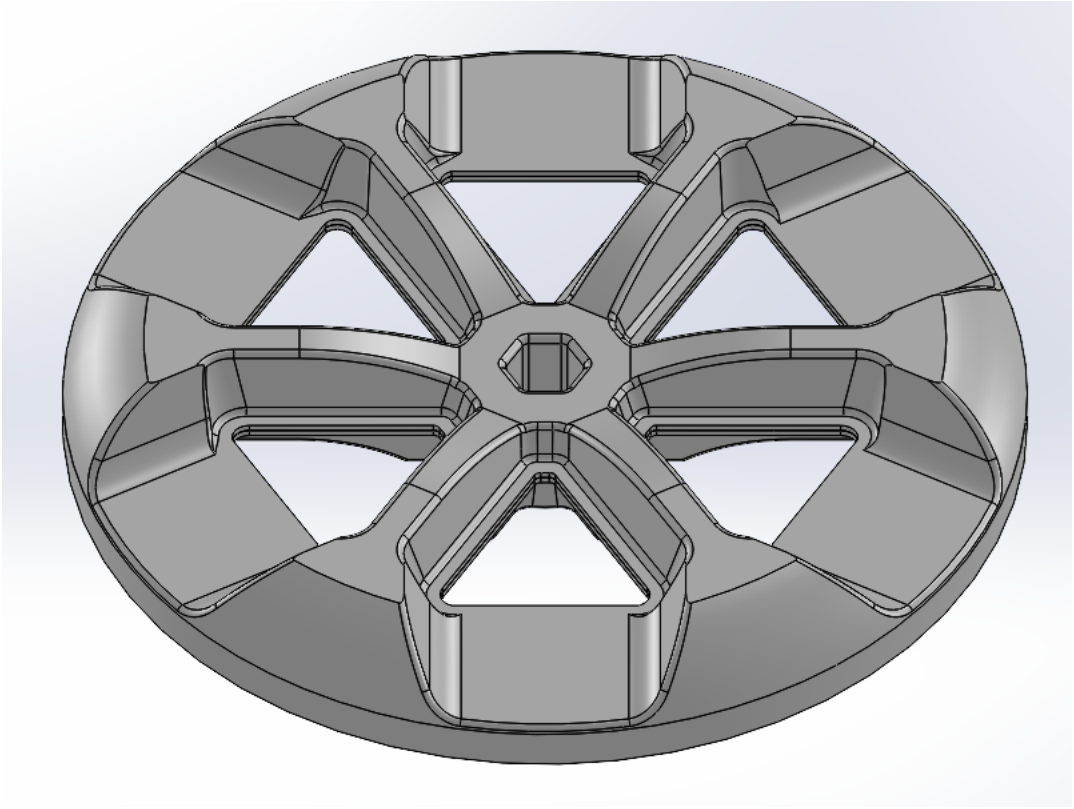

Figure 4.5: Hollow laminate rotor model

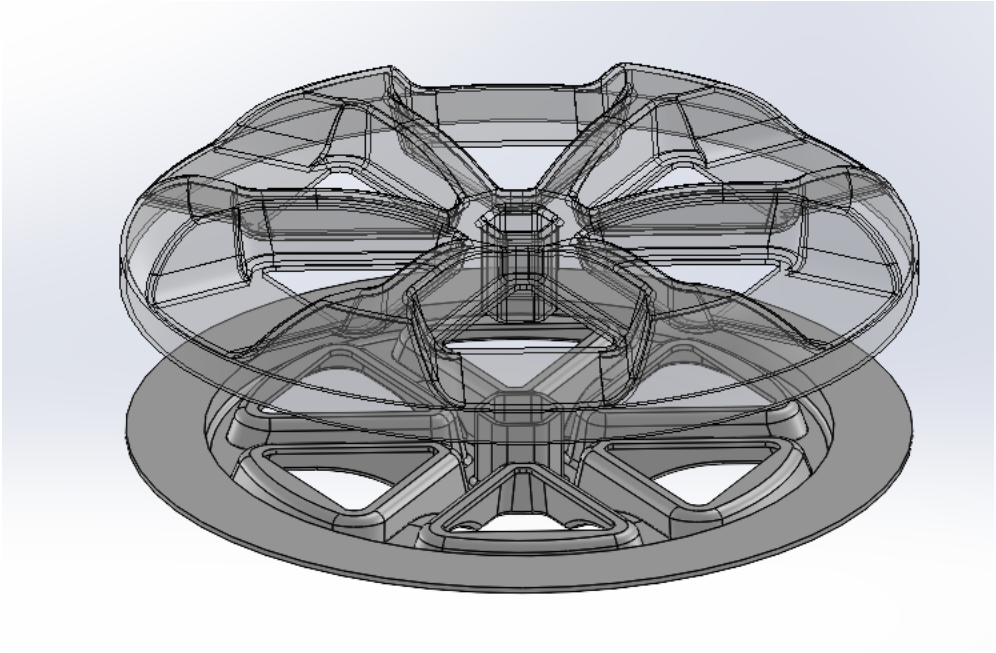

Figure 4.6: Hollow laminate rotor model exploded view

Figure 4.7: Prototype CFRP structure

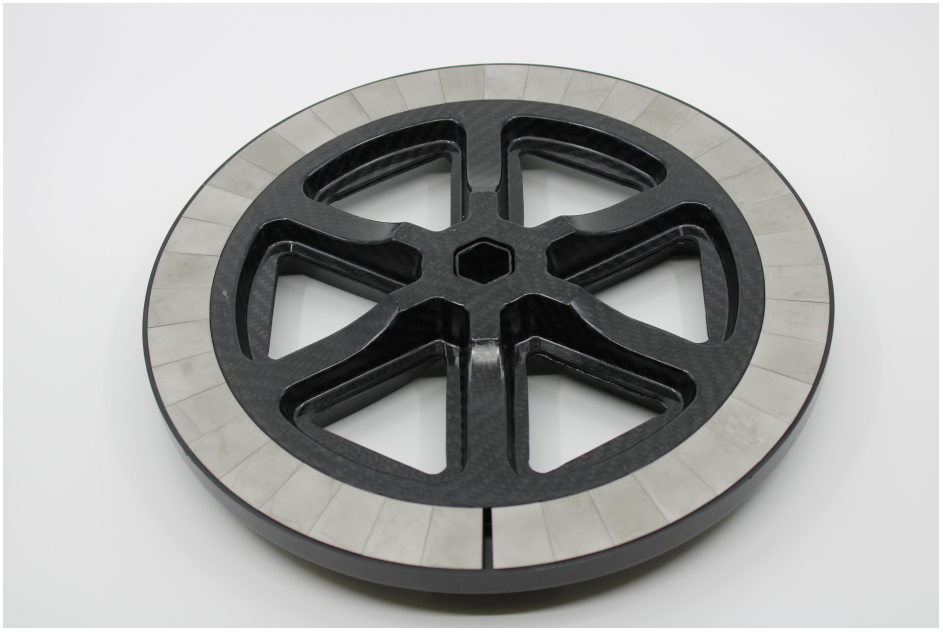

Figure 4.8: Prototype CFRP structure with mock magnets

4.1.2 Assembly Process

This sub-section highlights the procedure used to fully assemble the prototype rotor. To complete this process, the following materials are needed:

- Top half of composite rotor
- Bottom half of composite rotor
- 40 stainless steel "mock magnets" (simulates Neodymium magnets)
- 2 tubes of Loctite EA 11C epoxy
- Miapoxy Formula 65 Microspheres (or an equivalent at 0.1mm diameter)
- Face mask
- Paper plate
- Mixing stick
- 200 grit sandpaper
- 90% Isopropyl Alchohol
- Microfiber cloth
- Masking tape
- Knife (Xacto recommended)
- Surface liner

During Dry Assembly, there is a 3.5 – 4.0 mm gap existing in the tangential direction of the magnet assembly in the C-channel. Some of this should be absorbed by the epoxy interfaces (40 interfaces, minimum bond length is 0.1 mm, so the entire 4mm gap should be covered). Each mock magnet is 36.2 g in weight. The Neodymium estimate is 1443 g overall, split into 40 segments gives 36.1 g. This is only a 0.277% difference in weight.

The assembly procedure consists of 7 steps and is given below.

1. Assembly space setup: Use a liner on a flat tabletop surface. The liner should be clean and will serve as a clean surface to work on and protection for the underlying surface during bonding. A recommendation would be to use fresh wax paper. It is important to test both the Isopropyl alcohol and the epoxy mixture on an unimportant surface in both the composite and magnets. This is to ensure no adverse chemical reactions occur before fully committing to the assembly procedure.

2. Surface preparation: This step involves the use of sandpaper as a scratching tool and Isopropyl Alcohol as a cleaning agent along with the microfiber cloth. It is important that all bonded surfaces are scratched and clean prior to applying the epoxy – to ensure the strongest bond possible. Figure 4.9 shows the surfaces on the rotor which will be bonded, and Fig. 4.10 shows the surfaces on each magnet that will be bonded. To start, scratch the bond surface in circular motions until visible marks show on the surface. Attempt to move at a relaxed pace and perform about 10 rotations over the area before moving on. Be aware of residue that builds up on the sandpaper and discard for a fresh piece when needed. To clean the surface, simply soak the microfiber cloth in some of the Isopropyl alcohol and gently rub over the scratched surfaces. It is important to do this step after scratching the surface – as scratching leaves some contaminants on the surface. Be aware that the cloth will get progressively dirty as it cleans, so use a new area of the cloth as needed. Figure 4.11 shows a before and after picture of what the mock magnet surface looks like after properly prepped.

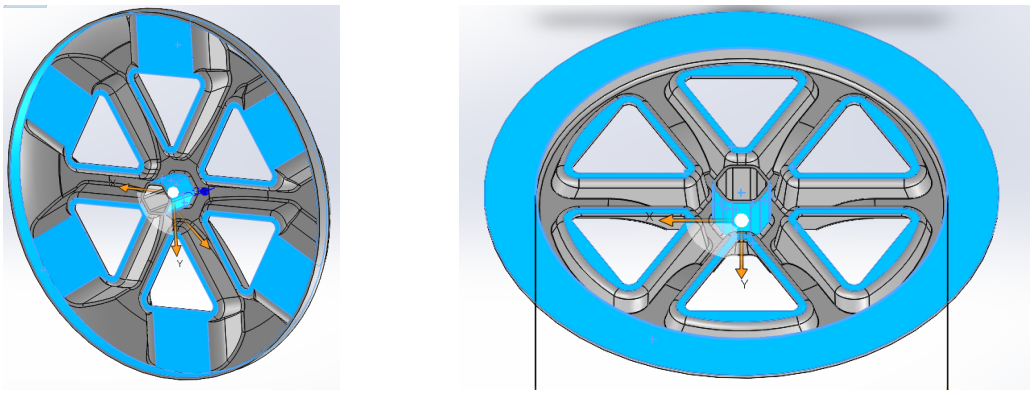

(a) Top rotor structure (b) Bottom rotor structure

Figure 4.9: Bond surfaces of rotor pieces highlighted in blue

(a) Isometric view 1 (b) Isometric view 2

Figure 4.10: Bond surfaces of mock magnet highlighted in blue

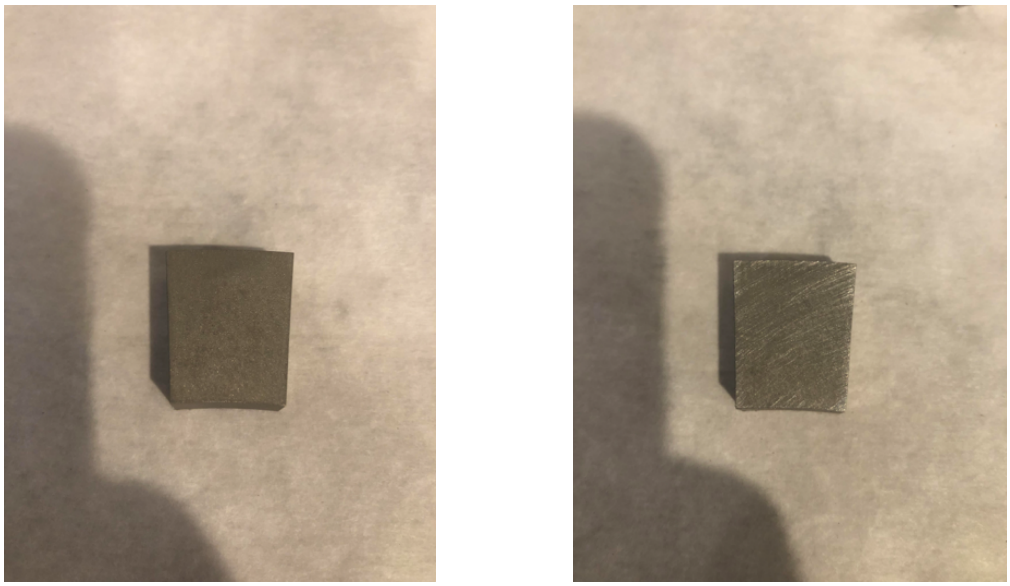

(a) Before surface prep (b) After surface prep

Figure 4.11: Mock magnet before and after surface preparation

3. Masking: To preserve the appearance of the rotor, it is important to use masking tape along all surfaces adjacent to bonding. First, place all mock magnets inside of the C-channel. Apply tape over all of the surfaces as seen in Fig. 4.12, including the shaft area. Next, take a knife and cut the outlines of the magnets. After these have been traced over, remove them individually from the C-channel as seen in Fig. 4.13. At this point, the magnets should be protected by the tape, and the structural segments adjacent to the C-channel should be protected as well.

Figure 4.12: Complete masking of rotor assembly

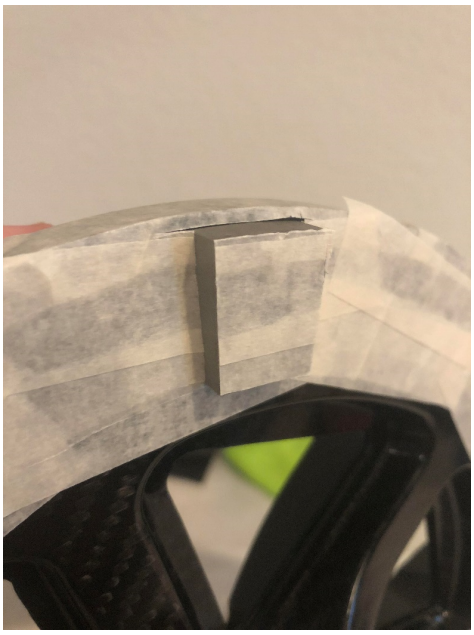

Figure 4.13: Removal of magnets from mask

4. Epoxy mixture preparation: After the surfaces have been prepped, the epoxy can also be prepared as long as everything is ready for immediate bonding. Depending on epoxy, a "work life" is specified as the period of time between mixing and application onto the surface. In the case of Loctite EA 11C, a 25 minute work life is recommended. To accommodate this,

the entire bonding phase is split into two sections: the Top and Bottom Rotor Structural Bonding, and the Mock Magnet Bonding. Hence, this step should only be performed when it is completely ready to assemble the other steps. To mix the adhesive, generally follow the directions given with the product. In the case of Loctite EA 11C, Fig. 4.14 shows the procedure given on the package. The product should be mixed on a clean, flat, dry, and discardable surface - a paper plate is recommended. Two tubes of paste are included – the resin and hardener – and should be squeezed out in even lengths alongside each other to obtain a proper mixture. Fig. 4.15 shows an example of this. Then, thoroughly mix the resin and hardener with a mixing stick – a wooden popsicle stick is sufficient. Finally, to ensure a proper minimum bond length thickness, some microspheres need to be blended into this mixture. Miapoxy formula 65 glass microspheres are used in this application. IMPORTANT: Wear a face mask when using this, as the spheres are very small and can easily act as dust in the air. Do not inhale! A small amount is only needed to mix with the epoxy, Fig. 4.16 shows an example of about how much should coat the mixing stick prior to application to the amount of resin given in 4.15. When thoroughly mixed, the microspheres should not alter the appearance of the epoxy.

Figure 4.14: Loctite EA 11C instructions

Figure 4.15: Epoxy mixture lengths

Figure 4.16: Amount of microspheres to add to mixture in Fig. 4.15

5. Top and bottom rotor structural bonding: Mix about one tube's worth of the adhesive and hardener together according to step 3. Once these are mixed, quickly yet carefully apply a liberal amount of epoxy to the structural bonding surfaces indicated in Fig. 4.9. Only one

side of each contact surface requires epoxy. Once all surfaces have been coated, slide the two pieces along each other and press to ensure contact exists between all bonded surfaces.

6. Mock magnet bonding: This step is time-consuming and best performed with a constant re-creation of the epoxy mixture. It will take about an hour to complete, and the work life of the mixture is 25 minutes. Ensure all magnet and composite surfaces are fully prepped before starting this process. To embed the magnets, first apply the epoxy mixture inside of the C-channel as opposed to each magnet surface. It is important that all 3 walls of the C-channel are coated, and to only coat about the area for 2-3 magnets at a time. Once the epoxy is applied, assemble the magnets individually and with enough force to push out the epoxy underneath. Subsequent magnets should also be forced in such that the bottom surface and the surface adjacent to the prior magnet has epoxy ooze out. Force is important to ensure consistent bond-line thickness between each surface. If bond-line thicknesses are inconsistent, then each mock magnet may not assemble towards the end of the process. Repeat until all magnets are assembled.

7. Curing: Once the entire assembly is bonded, it is recommended to remove all masking tape once completely finished with applying the epoxy. This is because the masking tape has accomplished it's job but will become difficult to remove after full cure is achieved. When curing, leave it in a safe place at room temperature. This mixture will reach 90% of full strength after 24 hours, and full strength after 72 hours.

The final result of this process is given in Fig. 4.17 Note that in the first prototype, removing the masking tape as instructed in step 7 was not performed until after a full cure is achieved. This is why pictures of the structure in Fig. 4.17 still have some masking tape in the cured epoxy regions. It is recommended to the reader that this tape is removed prior to full cure in order to avoid these cosmetic defects.

Figure 4.17: Prototype rotor after cure

4.2 Testing

Since the prototype structure made is similar to the original model given in Fig. 4.1, it should also perform similarly. However, significant changes have also occurred to make the design feasible to produce, and it is a major assumption to say that what was made will act like what was simulated. This section covers the experimental testing of the prototype rotor, and will determine if the structure as is will diminish the 1.25 mm air gap which exists between the motor rotor and stator segments.

4.2.1 Methodology

Since real Neodymium magnets were not able to be used, a stainless steel mock magnet was employed instead. These magnets also have a tapped hole in the center, which will connect to M5 screws. When these screws are in tension, the electromagnetic axial force is mechanically simulated. Fig. 4.18 shows the test fixture assembly to be used. All parts are made of stainless steel. The rotor is supported at the shaft area and by a small plate underneath. This is meant to simulate the same boundary conditions expected in the real motor application. Tensile load is applied from the bottom fixture, through a large plate, and through each 5 mm screw engaged to each respective

mock magnet in the fixture. Both the top and bottom fixtures then mounts onto a tensile testing machine which both applies a force, tracks overall displacements of the crossbeam, and records data throughout the experiment. Figure 4.19 shows the real-life setup of this experimental rig. The load path then simulates the no RPM forces the rotor experiences.

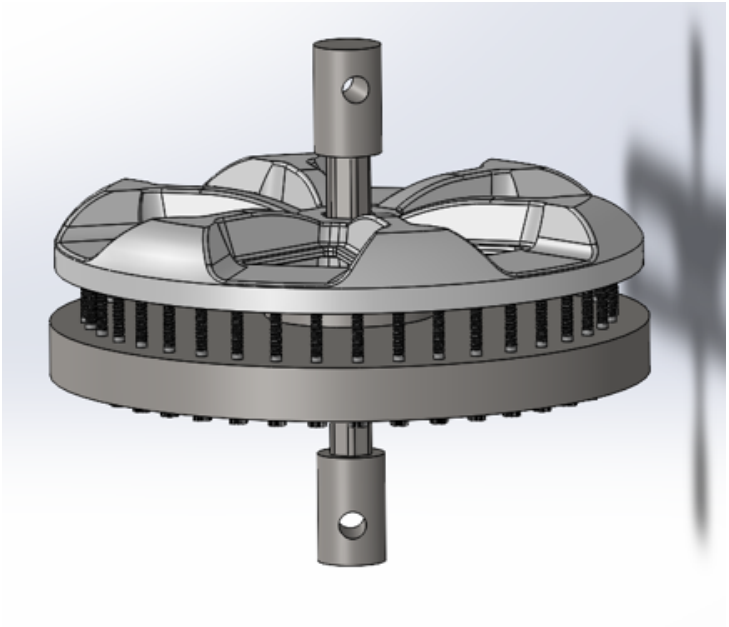

Figure 4.18: CAD of the test fixture

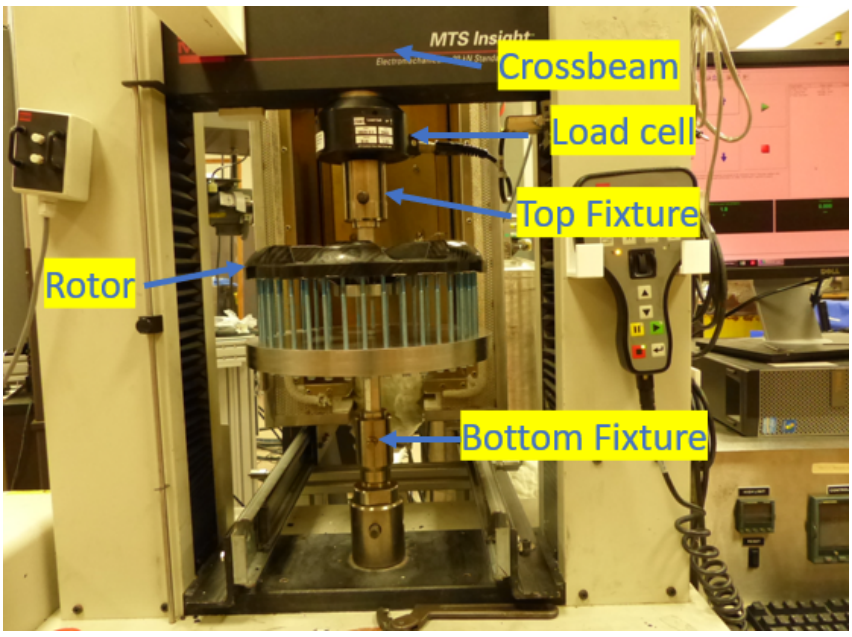

Figure 4.19: Experimental rig

4.2.2 Results

To simulate the forces expected, the tensile force was slowly applied at a rate of 1000 N per minute up to 700 N. While much lower than the full 5750 N, the goal here is to measure the bending stiffness of the structure and determine if the 1.25 mm airgap will be conserved. After the highest load was acheived, the structure was slowly relaxed. This process was repeated for a total of 3 times, with results given in Fig. 4.20.

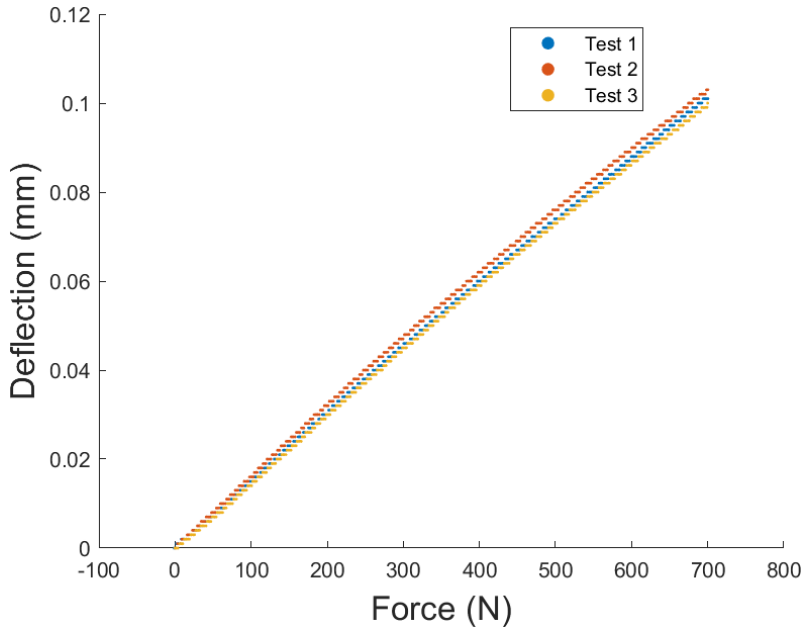

Figure 4.20: Experimental data comparing force applied to overall axial deflections

4.2.3 Discussion

Given a load of 700 N, a maximum deflection of 0.10 mm was recorded. This gives an overall compliance of 0.143 mm/kN. If extrapolating force to 5750 N, then the maximum axial deflection expected is 0.82 mm. Given that the air gap is 1.25 mm, this experiment suggests that the rotor is more than stiff enough to support this air gap size at the maximal load.

It is also important to note that the deflections measured in the assembly are not deflections solely from the rotor structure. Two significant sources of error exist: the overall deflections occurring from each member along the load path in the test assembly, and the deflections which occur from the epoxy magnet-structure interface not previously accounted for. This means that

once these are properly accounted for, the rotor structure deflection will likely be less than what is reported from the experimental data.

5. SUMMARY AND CONCLUSIONS

The introduction of this thesis gave the reader an understanding of the core subject matter behind the studies of this thesis. These include electric motor topologies, the specific Dual Rotor Axial Flux Motor Configuration our rotor structure is based around, common materials used in electric motors and the aerospace industry, and the challenges associated with designing with composite materials.

Chapter 2 introduced the geometric and performance parameters going into the rotor structural design, the expected load cases, the overall design space, preliminary guidelines for creating lightweight designs with composites, and the four different structural configurations.

This led to Chapter 3, which discusses the development of a Genetic Algorithm optimizer and FEA models in Abaqus software for each of the four structural configurations. Then, the optimizer is combined with the Abaqus FEA models to generate scatter plots comparing masses with axial deflections for each structural configuration, ultimately providing a mass-optimal design for each. Finally, the same optimization technique is applied to rotor structures with metallic materials and compared with that of a carbon fiber structure.

Chapter 4 took the optimal structure obtained in Chapter 3, and bridged the gap between design and reality with the creation of a real composite structure prototype. Simplifying the design to make it manufacturable brought the price down from $90,000 to $8,000. After the structure was fabricated, it was then tested in order to determine if the final product will be stiff enough to preserve a 1.25 mm air gap in the motor. Testing predicted that at worst the structure will deflect 0.82 mm at the maximum 5750 N load. Hence, the current structural design as is will satisfy this design requirement.

Key findings include:

1. In the Dual Rotor Axial Flux Motor topology, significant axial forces act on the rotor permanent magnets, which cause deflection of the rotor structures towards the stator. This

is unique for this configuration and is most prominent when the rotor is stationary (not spinning) since the centrifugal forces from rotation serve to "stiffen" the rotor. Therefore, the bending stiffness of this design is of utmost importance and should be the basis of structural mass optimizations.

2. Out of all composite mechanical properties, the longitudinal stiffness (E_1) has the greatest effect on overall bending stiffness and should be prioritized over the other properties.

3. When comparing structural configurations with quasi-isotropic layups running along the mid-section of the disk against those with a unidirectional layup, the unidirectional layup greatly outperforms every other configuration. Hence, leveraging the anisotropic properties of carbon fiber composites to enhance the stiffness of the structure is critical.

4. The best metallic structures are twice as heavy for the same bending stiffness as a unidirectional spoked disk carbon fiber structure.

5. A "hybrid" structure can be created by using a metallic main structure and a carbon fiber retaining ring around the magnets. The result is an optimal design that is just 50% heavier than an entire carbon fiber composite structure.

6. The first analytical model representing the performance of the rotor structure is unfeasible to produce. However, by designing the structure like more of a high-performance car wheel, a feasible design emerges.

7. The first prototype conservatively suggests a maximum deflection of 0.82 mm at a load of 5750 N. This confirms that this structure can be expected to maintain a 1.25 mm air gap in operation.

5.1 Future Work

This thesis thoroughly explored the design space of the rotor structure in a dual-rotor axial flux motor. The purpose was to give the reader a feel for how weight-optimal these structures may be

made with carbon fiber composites, and to compare that performance against competing metallic structural designs. Additionally, insights provided from the optimal structure inform the general geometry to a feasible to produce real-life composite rotor structure. However, this prototype is still significantly different from that used in sweeping the design space in Section 3. A new FEA model should be made that will better capture the geometry used in the real structure. Additionally, experimental results were gathered in predicting the overall deflection of the structure at a expected load. Due to the nature of the test assembly, data collected over predict deflections of the rotor structure and will need to be accounted for in order to find the true axial deflection of the rotor. Additionally, strength tests should be performed to validate the structural integrity of the prototype at both the no RPM load condition at the 5000 RPM load condition. It is advised that if testing at 5000 RPM, safety is of the utmost importance as a catastrophic rotor burst will result in a dangerous situation. Rotational testing up to 5000 RPM can be done to check both retaining ring integrity and for critical speeds. Finally, thermal effects should fully be explored as during motor operation the magnets are expected to reach 100 degrees Celsius. Effects on localized deflection, strength of both the structure and adhesive bonding, and creep should be quantified through experiments.

REFERENCES

[1] "Ford f-150 lightning." [Online]. Available: https://www.ford.com/trucks/f150/f150-lightning-electric-truck/

[2] "Yasa motor." [Online]. Available: https://www.yasa.com/products/yasa-750/

[3] "What is axial flux motor?" [Online]. Available: https://mechanicaljungle.com/what-is-axial-flux-motor/

[4] D. Talebi, M. C. Gardner, S. V. Sankarraman, A. Daniar, and H. Toliyat, "Electromagnetic Design Characterization of a Dual Rotor Axial Flux Motor for Electric Aircraft," 2021.

[5] M. C. Gardner and et al, ""Loss Breakdown of a Dual Conical Rotor Permanent Magnet Motor using Grain Oriented Electrical Steel and Soft Magnetic Composites," 2019.

[6] J. D. Widmer, C. M. Spargo, G. J. Atkinson, and B. C. Mecrow, ""Solar Plane Propulsion Motors With Precompressed Aluminum Stator Windings," *IEEE Trans. Energy Convers.*, vol. 29, no. 3, pp. 681–688, 2014.

[7] K. Grace, S. Galioto, K. Bodla, and A. M. El-Refaie, ""Design and Testing of a Carbon-Fiber-Wrapped Synchronous Reluctance Traction Motor," *IEEE Trans. Ind. Appl.*, vol. 54, no. 5, pp. 4207–4217, 2018.

[8] J. Oyama, T. Higuchi, T. Abe, and K. Tanaka, ""The fundamental characteristics of novel switched reluctance motor with segment core embedded in aluminum rotor block," *Proc. Int. Conf. Elect. Mach. Syst.*, pp. 515–519, 2005.

[9] R. Beloit, "Marathon motors catalog," 2018.

[10] Y. Wei, J. Bai, B. Yu, Z. Yin, and P. Zheng, ""Mover Optimization and Mechanical Strength Analysis of a Tubular Permanent-Magnet Linear Motor," *Proc. Int. Conf. Elect. Mach. Syst.*, pp. 1–4, 2019.

[11] T. F. Tallerico, Z. A. Cameron, and J. J. Scheidler, “"Design of a Magnetic Gear for NASA’s Vertical Lift Quadrotor Concept Vehicle,” *Proc. AIAA/IEEE Elect. Aircraft Technol. Symp.*, pp. 1–21, 2019.

[12] Y. Yu and et al., “"Rotordynamic Assessment for an Inside Out, High Speed Permanent Magnet Synchronous Motor,” *Proc. Int. Conf. Elect. Mach.*, pp. 529–535, 2020.

[13] “Material property charts.” [Online]. Available: https://www.grantadesign.com/education/students/charts/

[14] H. Shercliff and M. Ashby, *Reference Module in Materials Science and Materials Engineering*. Elsevier, 2016.

[15] G. Marsh, “"Airframers exploit composites in battle for supremacy,” *Reinforced Plastics*, vol. 49, no. 3, pp. 26–32, 2005.

[16] *MMPDS-11: Metallic Materials Properties Development and Standardization (MMPDS)*. Federal Aviation Administration, 2016.

[17] E. J. Barbaro, *Introduction to Composite Materials Design, 3e*. Taylor Fancis Group, 2017.

[18] C. Wiley, D. Talebi, S. Sankarraman, M. C. Gardner, and M. Benedict, “Design of a Carbon Fiber Rotor in a Dual Rotor Axial Flux Motor for Electric Aircraft,” in *ECCE*, Detroit, MI, 2022.

[19] “Cbi presents: Shear capacity of reinforced concrete slabs with openings.” [Online]. Available: https://cbi.rwth-campus.com/en/news/cbi-presents-shear-capacity-of-reinforced-concrete-slabs-with-openings/

[20] “Industry 4.0 testlab for composite carbon manufacturing.” [Online]. Available: https://blog.drupa.com/de/industry-4-0-testlab-for-composite-carbon-manufacturing/

[21] “Frp composite material.” [Online]. Available: https://dicausa.com/fiber-reinforced-polymer-frp-composites/

[22] "Understanding honeycomb panels." [Online]. Available: https://www.plascore.com/honeycomb/honeycomb-panels/

[23] I. J. B. S. Leigh Phoenix, *Comprehensive Composite Materials*, 2000.

[24] S. M. K. P. M. W. Lemanski SL, J Wang, ""Modelling failure of composite specimens with defects under compression loading," 2013.

[25] R. Unnthorsson and T. Runarsson, "Ndt methods for evaluating carbon fiber composites," 10 2022.

[26] L. Gorbatikh and S. Lomov, *Modeling Damage, Fatigue and Failure of Composite Materials*, ser. Woodhead Publishing Series in Composites Science and Engineering, R. Talreja and J. Varna, Eds. Woodhead Publishing, 2016. [Online]. Available: https://www.sciencedirect.com/science/article/pii/B9781782422860000030

[27] T. V. Y. Bai and T. Keller, "Delamination of pultruded glass fiber-reinforced polymer composites subjected to axial compression," pp. 66–73, 2009.

[28] "Yield and failure criteria for composite materials under static and dynamic loading." [Online]. Available: https://www.osti.gov/pages/biblio/1431008

[29] "Glass transition temperature." [Online]. Available: https://www.corrosionpedia.com/definition/593/glass-transition-temperature-tg

[30] J. K. N. R. G. Budynas, *Shigley's Mechanical Engineering Design, 11th edition*, 2019.

[31] "303 stainless steel mechanical properties." [Online]. Available: https://www.ezlok.com/303-stainless-steel-properties

[32] "Beam moment of inertia." [Online]. Available: https://www.metalroofsnowguards.com/Technical-Data_c_56.html

[33] "Abaqus fea software from dassault systemes." [Online]. Available: https://www.3ds.com/products-services/simulia/products/abaqus/

[34] D. J. Murray-Smith, *Modelling and Simulation of Integrated Systems in Engineering*. Woodhead Publishing, 2012.

[35] "Beale function." [Online]. Available: https://www.sfu.ca/~ssurjano/beale.html

[36] "Goldstein-price function." [Online]. Available: https://www.sfu.ca/~ssurjano/goldpr.html

[37] "Eggholder function." [Online]. Available: https://www.sfu.ca/~ssurjano/egg.html

[38] "L27 orthogonal array." [Online]. Available: https://www.york.ac.uk/depts/maths/tables/l27.htm

[39] "Koenigsegg." [Online]. Available: https://www.koenigsegg.com/index.php/

[40] "Koenigseggaircore." [Online]. Available: https://www.koenigsegg.com/aircore

[41] "Koenigsegg wheel." [Online]. Available: https://www.cnet.com/roadshow/news/lightweighting-taking-carbon-fiber-wheels-mainstream/